2007

Modeling, analysis and non-linear control of a novel pneumatic semi-active vibration isolator: a concept validation study

Hemanth Porumamilla
Iowa State University

Modeling, analysis and non-linear control of a novel pneumatic semi-active vibration isolator: A concept validation study

by

Hemanth Porumamilla

A dissertation submitted to the graduate faculty

in partial fulfillment of the requirements for the degree of

DOCTOR OF PHILOSOPHY

Major: Mechanical Engineering

Program of Study Committee:
Atul. G Kelkar, Major Professor
Jerald. M Vogel
Adin. J Mann
Fritz Keinert
Qingze Zou

Iowa State University

Ames, Iowa

2007

DEDICATION

I would like to dedicate the thesis to the divine mother without whose blessing I would have not been able to accomplish the task. I would also like to sincerely thank my family and well wishers for their motivation and loving support all through my graduate studies.

TABLE OF CONTENTS

LIST OF TABLES

LIST OF FIGURES

CHAPTER 1. Introduction

In the last 2 decades some of the prominent contributions to modern vehicle technology have been the developments of anti-lock brake and anti slip control systems, four wheel steering systems and advanced suspensions. The success of these developments is mainly due to the integration of advanced control algorithms which continuously monitor the performance and take necessary corrective action. This thesis study comprises of the modeling, analysis and control of a proposed novel pneumatic vibration isolation technology. This chapter presents a broad overview of the topic of vibration isolation as applied to suspension technologies. The subsequent chapters utilize this available background information and present the new vibration isolation concept as an alternative to the existing ones by demonstrating its advantages and capabilities.

1.1 Vibration isolation systems: A background

Advanced suspension systems play a crucial role in the performance of vehicles. Let's consider the well known and widely studied conventional linearized model of a passive suspension with spring of constant k and damper of constant c as shown in Fig. 1.1. It represents a lumped parameter approximation of a single degree of freedom (SDOF) vibration isolator. The essential problem in designing the suspension for this system may be stated thus:

1. The relative motion between the mass and the ground $(x - d)$ must be controlled due to space and other limitations.

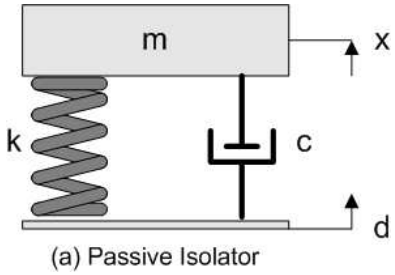

Figure 1.1 SDOF vibration isolator model

This could be achieved by making the suspension very stiff.

2. The suspension should isolate the motion of the mass from the ground motion, i.e., the transmissibility $(x/d) = (\ddot{x}/\ddot{d})$ should be less than unity for all but very low frequencies.

   This can be achieved by making the suspension very soft.

Clearly with fixed valves of k and c , even though an optimum performance could be achieved, it may still be unacceptable. Hence, advanced suspensions are basically required to improve the compromise between these conflicting ride and handling measures of vehicle performance. Specifically speaking, they must:

- support the vehicle body
- provide adequate passenger comfort
- maintain vehicle stability during various handling conditions
- control body and wheel attitude, and
- minimize the vertical force transmissibility

Although the idea of advanced suspension systems is not very new, research and development efforts in advanced suspension have been particularly extensive in the past few decades (1)-(6).

1.1.1 Modern passive suspensions

The word "advanced" must not be restricted to active suspensions, since, there has been significant advances in the design of passive suspension components, especially, shock absorbers. Being simple, reliable and inexpensive, these modern passive suspensions are still very competitive with their actively controlled counterparts. The absence of a power supply is usually the factor that distinguishes passive suspensions from other types. In modern passive suspension systems, almost all research focusses on the design of various types of shock absorbers. These dampers which are generally unsystematic in jounce and rebound, do not follow a simple linear damping law. Several studies (7)-(17) dealing with shock absorbers characteristics such as asymmetric and sequential damping, stick slip phenomenon amongst others have documented the usefulness of these non-linear phenomena when effectively utilized in the damper design.

Airspring is another typical suspension component used in place of mechanical coil springs on almost all types of suspensions. Airsprings when used as passive suspension elements offer some features which cannot be easily achieved by mechanical springs. Although, as compared to the shock absorbers, limited literature can be found on the analysis, synthesis and optimization of pneumatic springs, (18) is one prominent article published in the Shock and Vibration handbook, which is noteworthy. Modeling of the airspring is crucial to the understanding of the novel pneumatic isolator concept proposed in this study. Concepts from (18) have also been used in the present study to model the pneumatic spring and has been presented in chapter 6.

1.1.2 Active suspensions

The word "active" has been used loosely in research literature. It gets coined to any suspension that utilizes power supply and signal processing. Since, different suspensions may have different power and signal processing requirements, and there does not exist a

clear protocol to differentiate based on the amount of power supplied or the frequency band of active elements used, correct usage of the word "active" is not present in research literature.

The notion of active suspension system started several decades ago ((19), (20) and (21)) with the basic idea to replace the traditional suspension elements (springs and dampers) by a controlled system which would have virtually unlimited performance characteristics. Although, excellent performance could be achieved in theory by employing these controllable systems ((22), (23)), researchers and manufacturers quickly discovered many difficulties in putting such a system into production ((24), (25)).

These limiting factors led to the creation of two versions of active suspension systems: The "fully active" or "high frequency active suspension" and the slow active or "low frequency (band limited) active suspensions". In (26), it is suggested that low frequency active suspensions employ actuators with less than 8 Hz bandwidth and those of greater than 8 Hz bandwidth are characterized as high frequency (fully) active suspension. The one common feature in both these active suspensions is that the desired performance is still achieved by actuation, which results in addition of energy into the system. An example of a more recent "fully" active suspension technology is the Bose system shown in Fig. 1.2.

The Bose system uses a linear electromagnetic motor (LEM) at each wheel in lieu of a conventional shock-and-spring setup. Amplifiers provide electricity to the motors in such a way that their power is regenerated with each compression of the system. The main benefit of the motors is that they are not limited by the inertia inherent in conventional fluid-based dampers. As a result, an LEM can extend and compress at a much greater speed, virtually eliminating all vibrations in the passenger cabin. The motors mounted on each wheel, receive input from sensors throughout the vehicle and react to bumps and potholes instantaneously, using downward force to extend the wheel into potholes, while keeping the car level and the driver virtually unaware. As the wheel

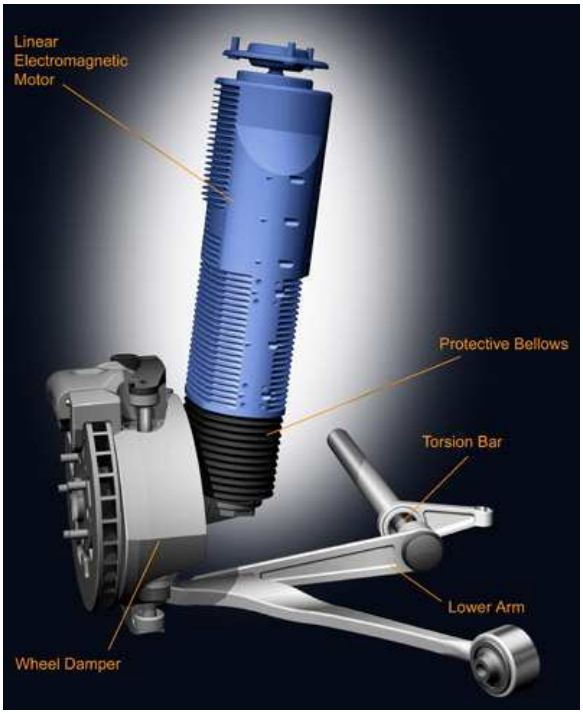

Figure 1.2 The Bose fully-active suspension system

pops back up onto the road, the suspension recaptures nearly all the energy expended.

The LEM can also counteract the body motion of the car while accelerating, braking and cornering. This way the system also improves handling, virtually eliminating body roll in tight turns and minimizing pitching motion during braking and acceleration. Hence, the performance trade-offs present in even the most advanced passive vibration isolators are almost completely eliminated by the use of such active systems. With all these advantages making this system a very attractive "buy", it's incorporation is still limited to high-end luxury vehicles owing to its exorbitant cost.

One other type of active suspension, which has received considerable research interest is the preview based active suspension. This preview based concept is broadly classified into two types. The first concept utilizes the road profile data ahead of the vehicle and uses this information to prepare the suspension ahead of timer to react appropriately. The second concept utilizes the dynamic variables from preceding axles as preview for

the axels that follow. Theoretical predictions show significant improvement,in the suspension performance under preview action. However, in the real world, preview based suspensions are mainly seen on multi-purpose army vehicles such as HMMWV (High Mobility Multipurpose Wheeled Vehicle), which travel on highly uneven terrain. Just like for the case of many other active systems, the cost of implementation and maintenance are the limiting factors precluding their use on more common automobiles.

1.1.3 Semi-active suspensions

Semi-active suspensions have been very popular with industries as well as the academic community owing to their advantages over both fully-active and passive suspensions ((31)-(37)). The main distinguishing factor between semi-active and all types of active suspension is that semi-active suspensions utilize components that are close to passive components in terms of dynamic behavior, cost and complexity. They produce the control action by varying their characteristics as compared to fully active suspensions, which utilize positive force actuators.

The most widely researched and implemented semi-active component is the MR damper. This semi-active damper is an externally controlled force generator whose force-velocity relationship could be modulated over a wide band of frequencies. A variety of control signals can be used to control the semi-active damper. **The biggest advantage of semi-actively controlled suspension over its fully active counterpart is that the inherent stability problems of fully active suspensions are not found in semi-active systems.**

Various control schemes for semi-active dampers have been studied in literature. They can be broadly classified into two categories.

1. The continuously controlled semi-active damper in which, the damping force depends on either the absolute velocity of the spring mass (Original skyhook control)

Figure 1.3 The VRS2000 semi-active suspension seat (Sears Seating Company)

or the relative velocity across the damper(Modified skyhook Control).

2. On-Off semi-active damper in which the damping force only depends on relative velocity across the damper and valve designs.

Extensive literature could be found on both these types of semi-active control designs. Fig. 1.3 is an example of a MR-damped semi-active suspension employing the continuous control scheme. The controller receives information about the suspension stroke from the rotary type position sensor as shown in the figure. The microprocessor uses this feedback information to compute the desired control signal to be provided to the MR-damper.

Although MR dampers have revolutionized the suspension industry, they still have shortcomings in their ability to achieve vibration isolation. In chapter 3, the performance limitations of MR-damper based suspensions is explained using fundamental concepts, which is then used as motivation for the development of the proposed purely pneumatic

vibration isolation technology. The ensuing section provides a detail description of airsprings, its history and other relevant information as part of background for the work presented in the thesis. This background information is also useful in understanding the mathematical modeling and analysis of the airspring behavior introduced in the later chapters.

1.2 Pneumatic springs

A pneumatic spring is a spring, which employs gas as its resilient element. Since, the gas is usually air, such a spring is called an airspring. The ability of the airspring to support a given mass is governed by the effective area and the confined gas pressure. The gas in the spring can be compressed to the pressure required to carry the load and, therefore, airsprings do not require large static deflection. The compressibility of the gas provides the desired elasticity for the spring. Hence, in applications where the load and static deflection are large, airsprings are most suitable.

History: Air suspensions have been around for more than a century and a half. Charles Goodyear, the founder of Goodyear tire and rubber company was issued a patent for rubber vulcanization in the year 1844. Only three years later in 1847, inventor John Lewis was granted an US patent for "Pneumatic Springs for rail road cars, Locomotives, Burden-Cars and Bumpers". This spring lacked the resilience required of a suspension component and hence did not receive much prominence for close to a century. It was not until post world war II with the invention of polymers including nylon tire cord and synthetic rubber elastomers that airsprings achieved success over its mechanical coil-spring counter part. In the present day, almost all vehicles including locomotives, off-road equipment, trucks, etc, use airsprings in one form or the other. The advantages that have made the modern day airspring so widely accepted are listed below.

Advantages of airsprings:

1. Airsprings have the capability of achieving a low natural frequency to provide a soft ride. The efficient potential energy storage of air is the reason behind this characteristic of airsprings.

2. Airsprings provide a constant natural frequency system over a wide range of sprung mass loading. Airsprings are able to achieve this characteristic by adjusting their static height so that their cross- sectional area and volume remain constant as the load varies.

3. Since, airsprings maintain a constant height for all load conditions, usable suspension stroke remains constant both in compression and expansion.

4. Airsprings are much lighter and compact as compared to the bulky mechanical coil-springs with comparable specifications.

5. Due to the compressibility of air, airsprings achieve significantly higher vibration isolation characteristics at higher excitation frequencies as compared to mechanical springs.

Disadvantages:

1. The low natural frequency characteristic of airsprings while desirable for vibration isolation, causes difficulty in controlling vehicle roll and handling. Although roll stabilizes help eliminate the problem to an extent, they stiffen the suspension, thereby, reducing the soft feel.

2. Airsprings require more maintenance than mechanical coil-springs and are also subject to damage by sharp and hot objects.

3. The operating temperature range for airsprings is also restricted compared to those of mechanical springs.

In spite of these limitations, airsprings have become an indispensable suspension component for a wide variety of applications both mobile and stationary.

1.2.1 Types of airsprings

Since its invention in the 1800s, many different types of pneumatic springs have been developed and several of these are in use even today. They include:

Figure 1.4 Types of airsprings

Convoluted type airspring It has a very low minimum height and a stroke that is larger than its minimum height. It is available in one , two or three convolutes. This type of airspring is mainly used in secondary suspensions to isolate the sprung mass from high-frequency shock-type inputs.

Rolling lobe type airspring As shown in the Fig. 1.4, the rolling lobe type airspring is usually a heavy duty air spring used for chassis suspension of vehicles and is capable of producing large axial displacements without max-ing out on the stroke. Hence, they are suitable to be used as primary suspension units.

Sleeve type airspring Sleeve type airspring is very similar to the rolling lobe type. The differences is in the fabric of the rubber. Rolling lobe airsprings have a much

thicker and stiffer fabric with many layers interlaced, which make the airspring rugged. This is necessary since they are subjected to more extreme working conditions and are also required to haul larger loads. Sleeve type airsprings are usually used for seat/cab suspensions and have a thin rubber fabric thereby reducing the overall stiffness of the spring. On the downside, they are not as resilient as the rolling lobe type.

Rolling diaphragm type airspring This type of airspring is very similar to the rolling lobe airspring, but, has a small stroke and is employed to isolate low-amplitude vibration. As compared to the first three types , this airspring has high lateral stiffness. This characteristic makes these airsprings highly suitable for secondary suspensions in trains permitting bolster-less bogies, thereby, simplifying the bogie design.

1.2.2 Manufacture

Pneumatic springs are built in a manner similar to tire manufacture. The basic steps are:

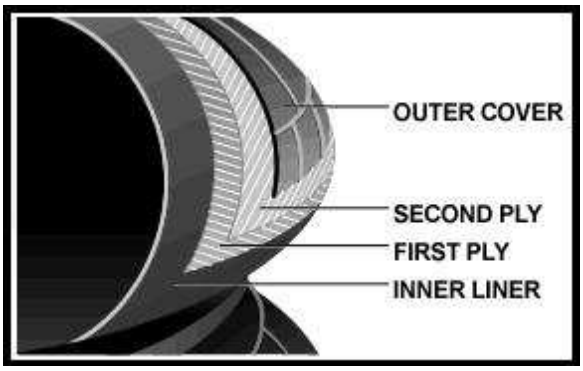

Figure 1.5 Airspring construction

1. A compound rubber liner having good flexing life and air retention properties is applied to the building drum.

2. One, two or four piles of rubber-coated fabric are applied to the liner at desired cord angles as shown in Fig. 1.5. The rubber treatment provides adhesion of the piles and good flex life.

3. A rubber cover compounded to provide good resistance to flex fatigue, weathering and adhesion is added.

4. When required, beads are applied and anchored in place by a wrap over of the fabric.

5. The un-vulcanized part is removed from the building drum and placed in a curing mold.

6. Heat and pressure are applied to effect vulcanization of the spring.

7. The cured flexible member is removed from the mold and inspected.

8. The metal components and the flexible members are assembled and tested for air-tightness at the rated pressures.

1.2.3 Airspring fundamental governing laws

The spring effect of airsprings is due to the compressible nature of air enclosed in it. When airspring volume reduces during suspension jounce, the air particles get squeezed closer together, thereby, increasing both pressure and temperature. The gas pressure in the airspring is dependent on the speed and magnitude of deflection. Hence, for any particular deflection, the pressure will be different based on whether the governing process is isothermal, adiabatic or polytropic.

Since the spring rate is a function of the absolute pressure inside the airspring, the governing process should be identified to ascertain the spring stiffness.

Isothermal process: An isothermal process is a process in which the temperature of the system under consideration remains constant and is governed by the relation

$$p_1 v_1 = p_2 v_2 \tag{1.1}$$

where p_1, p_2 = Initial and final absolute pressures.
v_1, v_2 = initial and final volumes (absolute).

It is a well known fact that all gases heat up when compressed and cool down when expanded. However, if the airspring is stroked very slowly so that all the heat generated during compression or that absorbed during expansion is dissipated, an isothermal process results. Since, the airsprings get excited in a moderate to high frequency band and since, the rubber fabric enclosing the air insulates it from the surroundings, Isothermal process approximation is not realistic and is generally not employed for modeling.

Adiabatic Process: An adiabatic process is a process during which there is no heat transfer between the system and its surroundings and such a process is governed by the equation

$$p_1 v_1^{\gamma} = p_2 v_2^{\gamma} = constant \tag{1.2}$$

where γ is the ratio of specific heats c_p/c_v of the gas and is 1.4 for air.

During suspension jounce, very little heat escapes due to the speed of compression and the rubber insulating layer that encloses the air. Similarly, during rebound, negligible heat enters the airspring due to the same reasons. Thus, during compression, the air temperature inside the airspring increases and when the airspring goes into rebound, the sudden decrease in pressure causes the air temperature in the airspring to instantaneously drop. If airsprings are excited quickly enough and with zero mean random vibration, all the heat of the operation is conserved and an adiabatic process results.

However, airsprings neither follow an isothermal or adiabatic process and obey a polytropic law. But, since the process is much closer to adiabatic than Isothermal, an adiabatic process approximation is widely employed including the present study.

CHAPTER 2. Field test project: A motivation

The material contained in this chapter includes the description and corresponding results of a series of road tests performed on seven utility truck configurations located throughout the Iowa region. The road tests were designed to provide databases from which quantifying methods that address operator/occupant response to whole-body vibration in relation to human health and comfort could be investigated. The intension of the project was to acquire a real-world feel in the area of vibration isolation and to also get an idea of the severity of the need (if required) for superior vibration isolators.

2.1 Introduction

Whole-body vibration (WBV) is classified as one of the many physical occupational hazards in the workplaces. A vast group of workers typically subjected to this type vibration are operators or drivers of numerous kinds of vehicles used in agriculture, transport, materials handling, mining, and forestry. Another human population segment impacted by WBV is the mobility impaired group that must rely on a wheelchair mode of transportation. WBV does not target a specific organ within the human body, thus creating non-specific health outcomes not easily discerned. Even though WBV has been previously researched ((27) ,(28) and (29)), it is difficult to quantify, costly to control and hence often ignored until faced with complaints on health problems. The aim of the present study was to quantify WBV so that a qualitative assessment on human comfort and health when exposed to vibration could be made.

2.1.1 ISO 2631-1

The overall test program was designed using guidelines from the International Organization of Standards (ISO), the worldwide federation of national standards bodies. This international standard defined by ISO 2631-1 provides methods for the measurement of periodic, random and transient whole-body vibration. It indicates principle factors that combine to determine the degree to which a vibration exposure will be acceptable. ISO 2631 is applicable to motions transmitted to the human body as a whole through supporting surfaces; the feet, buttocks, back, etc. Since, the vibration environment in utility trucks closely corresponds to that quantified by the ISO 2631 guidelines, it was chosen as the standard for testing and analysis.

Specifically, the ISO 2631-1:1997(E) was used to determine the details dealing with the instrumentation component specifications, the number and distribution of components within the truck cab, data sampling techniques for data acquisition, and data reduction techniques. The results and conclusions were generated also using the guidelines contained in this ISO standard. This document, entitled Mechanical Vibration and shock - Evaluation of Human Exposure to Whole-Body Vibration - Part 1: provides the basis for a quantitative assessment on the effects of vibration on health and comfort.

A detailed description of the truck cab instrumentation type and layout, data sampling procedures, road test segments and driving technique, and vibration evaluation methods are contained in the sections that follow directly below. A comprehensive discussion of test results are contained in the latter sections.

A set of 7 utility truck configurations were identified for inclusion in the test program. These trucks mainly included class 7 and 8 utility trucks typically used in construction industry.

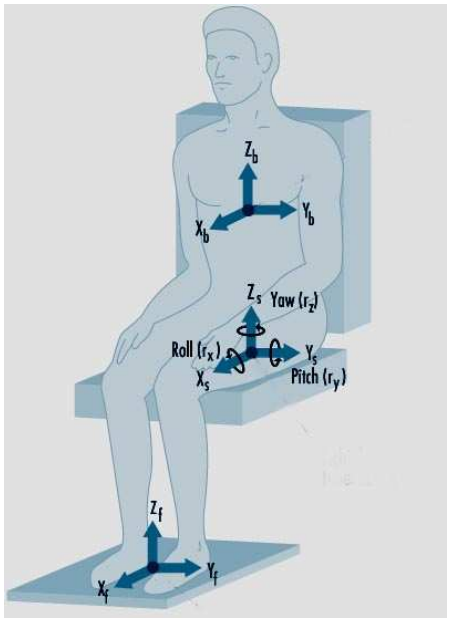

Figure 2.1 Human body schematic

2.2 The instrumentation package: components and layout

Constraints used in developing the instrumentation package (components and layout) are clearly defined in ISO 2631-1:1997(E), Part 1: General Requirements, clauses 1 - 5.3. Below is an explanation of the same.

2.2.1 Instrument/data acquisition system specifications

The primary signal to be measured in the truck testing program is interior cab acceleration in the 0.5 - 80 Hz frequency band at each of several specified locations as defined in subsequent section. Highly sensitive accelerometers in the (+/-) 5 - 10 g range with operational frequencies in the cited range were chosen for data acquisition. Accelerometer output was directed through a signal conditioner unit to a PC based analog-to-digital data acquisition board.

2.2.1.1 Instrumentation, component enumeration and layout details

The primary subject of interest in this investigation was the vibration environment for passenger side occupant of the truck cab. Driver side occupant was equipped with an air suspension seat which was assumed to provide better vibration isolation environment than passenger side. Hence, driver side was considered to be of less importance in the study. However, minimal instrumentation was applied to driver side to provide a measure of the voracity for this assumption. In both cases, occupant is considered to be in a seated position with body contact in the feet, buttocks, and back portions of the human body. Per ISO 2631, Part 1, clause 5.2, accelerometers were placed in each of the 3 locations as follows:

1. x-, y-, z-axes, feet
2. x-axis , y-axis, and z-axis seat surfaces
3. x-axis, seat back

In all cases, the rotational motions of roll, pitch, and yaw were considered negligible with respect to whole-body vibrations. Figure 2.2 depicts the locations for 10 accelerometers used in the data acquisition package. Accelerometer outputs arranged in specific combinations yielded appropriate information regarding passenger and driver occupant vibration environment as follows:

- Passenger Side
    1. Accelerometers 1, 2, 3 for feet region
    2. Accelerometers 8, 9, 10 for buttocks region
    3. Accelerometer 7 for seat back region
- Driver side

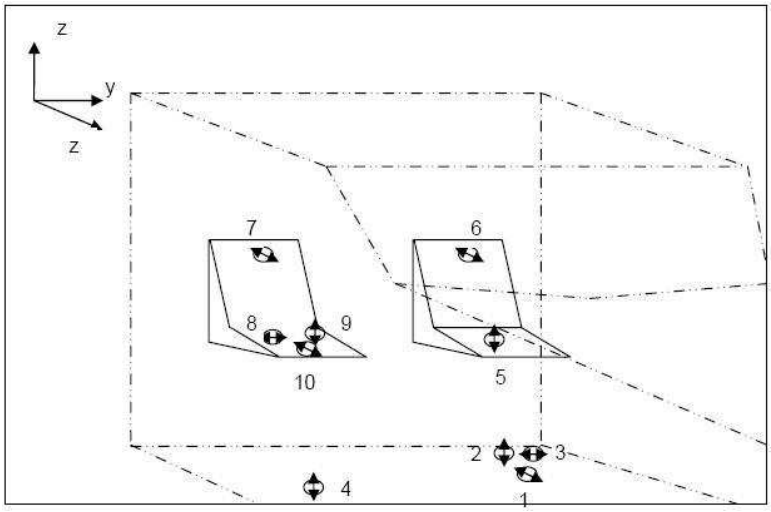

Figure 2.2 Locations of accelerometers incorporated in the instrument package

1. Accelerometers 1, 2, 3 for feet region
2. Accelerometers 5, 8, 10 for buttocks region
3. Accelerometer 6 for seat back region

It is noted here that accelerometers 8 and 10 are used to provide information for both passenger and driver sides enforcing the assumption that the lateral (side-to-side) and longitudinal (fore/aft) accelerations in the seat surface regions are similar. This assumption is reasonable in that neither the passenger nor driver seat is equipped with vibration alleviation along those axes. A similar assumption is required for feet region vibrations with accelerometers 1, 2, and 3 providing the required vibration information. Accelerometer 4 is used to provide corroborative information regarding floor vertical acceleration, and, when used in conjunction with accelerometer 2, provides quantitative information on truck pitch and roll accelerations.

(a) (b)

Figure 2.3 Instrumented seat cushion used to house seat accelerometers

2.2.2 Accelerometer cluster design/installation

The ten accelerometers used to sense interior truck cab accelerations were packaged and installed using guidelines per ISO 2632, Part 1, clause 5.3. According to these guidelines, accelerometers used to measure occupant exposure in the buttocks and back regions had to be placed between the occupant and the corresponding seat surfaces, and the interaction between occupant and seat could not interfere with accelerometer orientation during the testing process. Thus, accelerometer mounts containing accelerometers were embedded in a thin seat cushion (Fig. 2.3a) with appropriate cutouts for securely housing the instruments. Instrumented cushions for both driver and passenger seats were securely attached (Fig. 2.3b) in each truck tested.

Mounts for securing each accelerometer set within the seat cushion consisted of a metal/rubber wafer structure constructed by bonding a firm rubber core material between two thin metal plates. Cutouts for encapsulating accelerometer bodies were placed

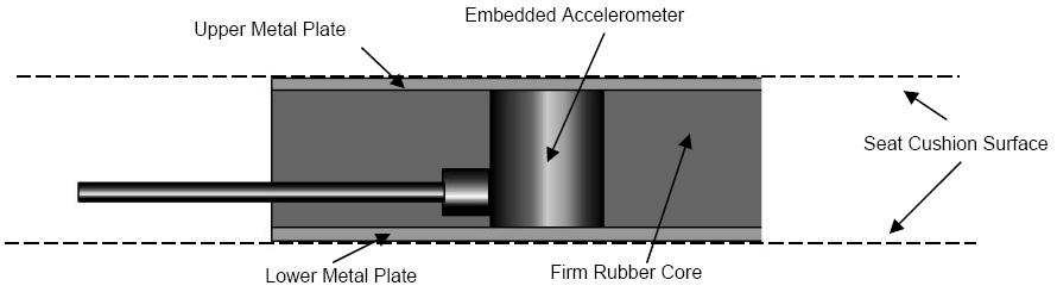

Figure 2.4 Accelerometer containment modules

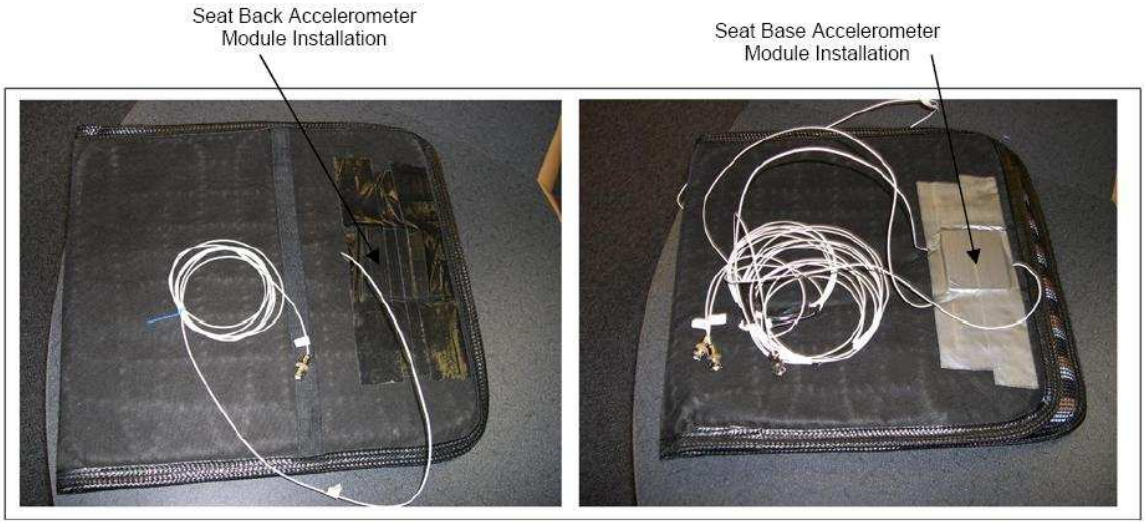

Figure 2.5 Seat-back and seat-base accelerometer module installations

in the rubber core (Fig. 2.4). This type construction secured each accelerometer and helped it maintain a proper position during all tests. Figure 2.5 depicts the seat cushion with embedded accelerometers.

Accelerometers for measuring cab floor vibrations were embedded in a small wooden block that was securely attached to the floor. Figure 2.6 depicts the 3-axis floor module.

2.3 Data acquisition procedures

The overall data sampling procedure used to test each truck configuration was carefully designed to ensure that test results accurately reflect typical daily cab vibration

Figure 2.6 Floor region accelerometer module showing a 3-axis set

environments. Roads within the operational region of the truck/crew combination were traversed at typical speeds.

In all cases, the road types included city streets, county surfaced roads, and gravel roads. Drivers were asked to distribute the test time on each road type to accurately reflect typical daily activities. Within these guidelines, several 3-minute data acquisition bursts were acquired for each road type. The target for total sampling time for each truck configuration test was set at 1-hour. Acceleration levels were sampled at a rate of 500 Hz for each of the 10 accelerometers.

2.4 Vibration evaluation method

The vibration evaluation guidelines of ISO 2631-1 are applied to provide quantitative insight of vibration on comfort and health. The basic evaluation method of vibration evaluation using weighted root-mean-square acceleration per ISO 2631-1, clause 6.1, was applied to the test databases. Frequency weighting curves recommended by the guidelines contained in ISO 2631-1, were used for the various acceleration directions. The specific guidelines used for application of the basic evaluation method for health

and comfort are given in ISO 2631-1, clauses 7 and 8, respectively, for health and comfort considerations. Guides to the effects of vibration on health and comfort per ISO 2631-1, were used in assessing basic evaluation method results and are explained in the following subsections.

2.4.1 Basic evaluation method

As per ISO 2631-1, vibration evaluation based on the basic evaluation method always includes measurements of the weighted root-mean-square (r.m.s) acceleration defined by,

$$a_w = \left[\frac{1}{T}\int_0^T a_w^2(t)dt\right]^{\frac{1}{2}} \tag{2.1}$$

where, a_w= the weighted acceleration (translational and rotational) as a function of time. T = the duration of measurement.

In the case where vibration enters the system in more than one direction, the vibration total value of weighted r.m.s acceleration, determined from vibration in orthogonal coordinates is calculated as,

$$a_w = (k_x^2 a_{wx}^2 + k_y^2 a_{wy}^2 + k_z^2 a_{wz}^2)^{\frac{1}{2}} \tag{2.2}$$

where, $a_{wx},\ a_{wy},\ a_{wz}$ are the weighted r.m.s accelerations with respect to the orthogonal axes x,y,z respectively. k_x, k_y, k_z are the multiplying factors. The exact value of the multiplying factors depends on the frequency weighting selected to either predict the effects of vibration on comfort or health and also on the point where vibration enters the human body (feet, buttocks, back).

The applicability of the basic evaluation method results were tested using crest factors defined and evaluated per ISO 2631-1, clause 6.2. According to these guidelines, crest factors in excess of 9 cast doubt on basic evaluation method results and in such cases the additional evaluation method which uses the running r.m.s method per ISO 2631-1, clause 6.3 was used.

2.4.2 Additional evaluation method

The crest factor method of ISO 2631-1, was used to investigate the suitability of the basic evaluation method in describing the severity of vibration. Crest factors were used to test data samples acquired in the test program for excessive acceleration spikes which the basic evaluation method might not consider. ISO 2631-1 defines Crest factor as the modulus of the ratio of the maximum instantaneous peak value of the frequency weighted acceleration signal to its r.m.s value. Specifically, for crest factors less than or equal to 9, the basic evaluation method is normally sufficient. For higher values of crest factors additional methods of evaluation had to be employed.

2.4.2.1 The running r.m.s method

The running r.m.s evaluation method takes into account occasional shocks and transient vibration by use of a short integration time constant. The vibration magnitude is defined as the maximum transient vibration value (MTVV), given as the maximum in time of $a_w(t_0)$ defined by:

$$a_w(t_0) = \left\{ \frac{1}{\tau} \int_{t_0-\tau}^{t_0} [a_w(t)]^2 \, dt \right\}^{\frac{1}{2}} \tag{2.3}$$

where, $a_w(t)$ is the instantaneous frequency weighted acceleration. τ is the integration time for running averaging. t is the integration variable. t_0 is the time of observation.

The maximum transient vibration value, MTVV, is then defined as

$$\text{MTVV} = max[a_x(t_0)] \tag{2.4}$$

i.e. the highest magnitude of $a_w(t_0)$ read during the measurement period.

2.5 Test results

2.5.1 Basic evaluation method

Figure 2.8 enumerates results for the 7 truck configurations tested. The red portion of the table deals with occupant comfort per basic evaluation method. The data contained in the second row of the table represents values of vibration magnitude corresponding to comfort for driver and passenger individually. Qualitative assessment on degree of comfort was made using criteria of ISO 2631-1, annex c.2.3 and is contained in rows-3 and -4. It was noticed that all trucks generally fell within the “fairly uncomfortable” to “uncomfortable” range of comfort.

Row-5 (green color) corresponds to the vibration magnitude levels corresponding to health for both driver and passenger using the basic evaluation method per ISO 2631-1, clause 7. Assessment regarding occupant health is made per ISO 2631-1, annex B. Interpretation of the cited vibration levels requires that the duration of testing be between 4 - 8 hours. Composite sample times for data acquisition during tests were in the 1-hour range. Since the tests were conducted using typical road types and travel times as experienced on a daily basis of operation, the weighted r.m.s. value of acceleration obtained for this reduced duration of testing was assumed to be representative for that of a 4 - 8 hour duration.

Figure 2.7 contains the test vibration magnitude levels showing the time extension from test sample time to the 4-8 hour reference time. Test results from all trucks show that the vibration magnitude levels generally fell within the ”health guidance caution zone”. Per ISO 2631-1, annex B.3.1, ”in the zone, caution with respect to potential health risks is indicated and above the zone health risks are likely”. Hence, these results showed that even from a health perspective, the seat suspensions were inadequate in ensuring requisite vibration isolation.

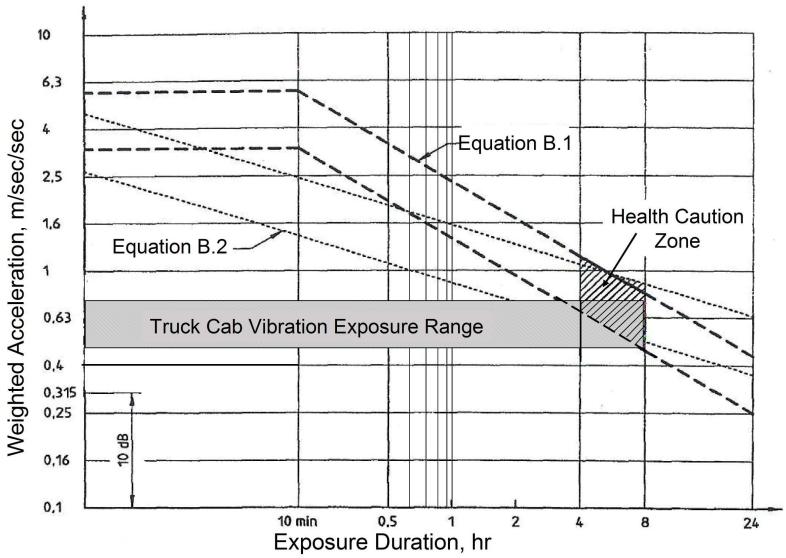

Figure 2.7 Health guidance caution zones for driver and passenger

2.5.2 Additional evaluation method

Crest factors generated from the composite data samples for all trucks tested are contained in rows 6-12 of Table 2.8. Generally, the trucks exhibited crest factors clustered around the value of 9. However, some truck configurations showed crest factors in the near 30 range. Hence the running r.m.s. method of ISO 2631-1, clause 6.3.1 was used for the additional evaluation method.

Representative plots for one truck configuration and corresponding to the ratio of the 1-second running r.m.s. value to the sample r.m.s. value of the basic evaluation method are shown in Figs. 2.9 and 2.10. Ratios in excess of a 1.5 value indicate excessive vibration spike activity. The ratios have been sorted in an ascending value order to depict the portion of each test sample which is beyond the critical ratio of 1.5 per ISO 2631-1, clause 6.3.3. The figure indicates that the cab interior vibration environment contain significant portions of ratio values in excess of the critical 1.5 value.

Name of truck	FL70 Des Moines	M2106 Urbandale	FL70 Waterloo	FL70 Avoca	FL70 Ottumwa	FL70 w/trailer Ottumwa	FL80 Rock Island
Duration of measurement (in mins)	42.3	57.9	37.7	51.2	45.7	46.7	63.6
R.M.S vibration total value a_v in m/s^2 (Passenger/Driver) (Basic evaluation method for comfort)	0.71 1.01	0.68 0.84	0.58 0.63	0.59 0.94	0.58 0.74	0.59 0.74	0.66 0.96
Comfort index (Passenger) (Basic evaluation method)	Fairly Uncomfortable	Fairly Uncomfortable	Fairly Uncomfortable	Fairly Uncomfortable	Fairly Uncomfortable	Fairly Uncomfortable	Fairly Uncomfortable
Comfort index (Driver) (Basic evaluation method)	Uncomfortable	Uncomfortable	Fairly Uncomfortable	Uncomfortable	Fairly Uncomfortable	Fairly Uncomfortable	Uncomfortable
R.M.S vibration total value a_v in m/s^2 (Passenger/Driver) (Basic evaluation method, health)	0.64 0.75	0.60 0.59	0.39 0.50	0.60 0.56	0.59 0.70	0.60 0.65	0.63 0.75
Crest factor (Passenger/Driver) Floor vertical	15.8 61.5	7.0 10.9	7.5 7.4	12.0 7.7	10.3 13.4	9.7 12.7	6.5 10.3
Crest factor (Passenger/ Driver) Floor Fore-aft	10.0 10.0	11.7 11.7	7.8 7.8	12.9 12.9	10.5 10.5	9.9 9.9	9.9 9.9
Crest factor (Passenger/Driver) Floor lateral	9.4 9.4	9. 2 9. 2	10.7 10.7	12.3 12.3	8.9 8.9	10.3 10.3	9.1 9.1
Crest factor (Passenger/Driver) Seat vertical	24.0 28.4	8.1 10.8	6.7 10.8	27.9 7.4	8. 8 13.1	11.7 13.3	7.0 9.4
Crest factor (Passenger/Driver) Seat Fore-aft	15.7 15.7	12.3 12.3	9.6 9.6	9.0 9.0	10.5 10.5	10.2 10.2	9.9 9.9
Crest factor (Passenger/Driver) Seat lateral	18.2 18.2	11.5 11.5	8.8 8.8	12.3 12.3	29.1 29.1	10.0 10.0	9.0 9.0
Crest factor (Passenger/Driver) Seat-back Fore-aft	12.4 13.5	9.5 11.4	8.3 9.0	12.9 10.2	8.9 10.3	8.2 7.1	7.8 7.1

Figure 2.8 Results of basic evaluation of vibration effects using weighted r.m.s. acceleration values for comfort/health and crest factors for judging basic evaluation method applicability

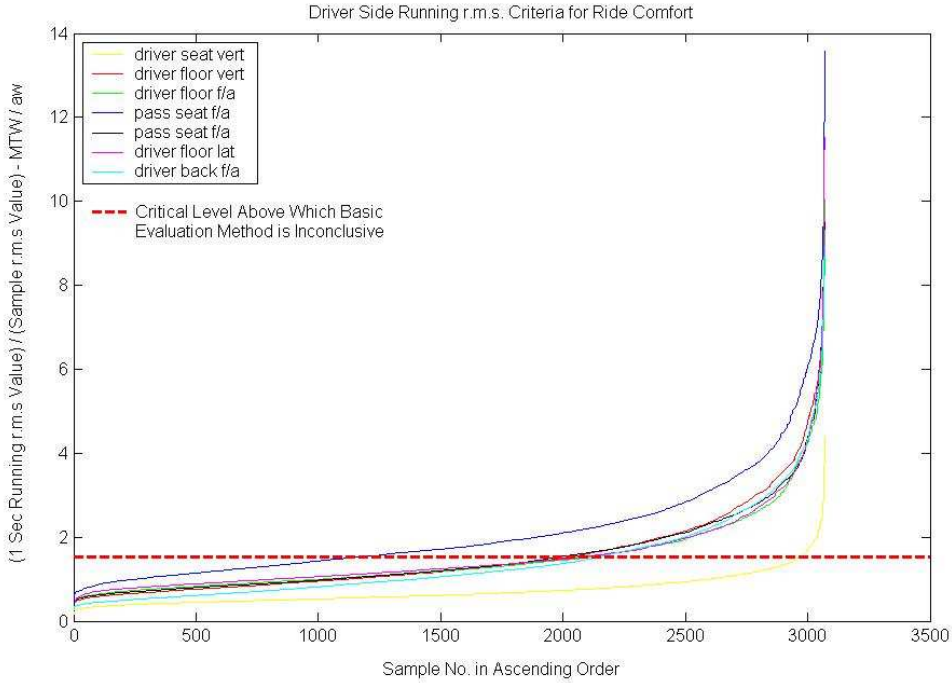

Figure 2.9 Acceleration ratio: driver side

2.6 Summary of results

1. The basic evaluation method per ISO 2631-1 standards indicated that all trucks provided ride comfort in the "fairly uncomfortable" to "uncomfortable" range of comfort quality.

2. All trucks exhibited cab vibration magnitudes that approached the "health guidance caution zone" in the 4 - 8 hour exposure time.

3. Further analysis using an additional evaluation method cast doubt on the sufficiency of the basic method procedures to predict additional comfort and health problems due to acceleration spikes.

In summary, the field test project brought to light the inarguable fact that the vibration environment in the trucks tested (which are typical of trucks used by many industries) needed to be enhanced, both from a comfort as well as a health standpoint.

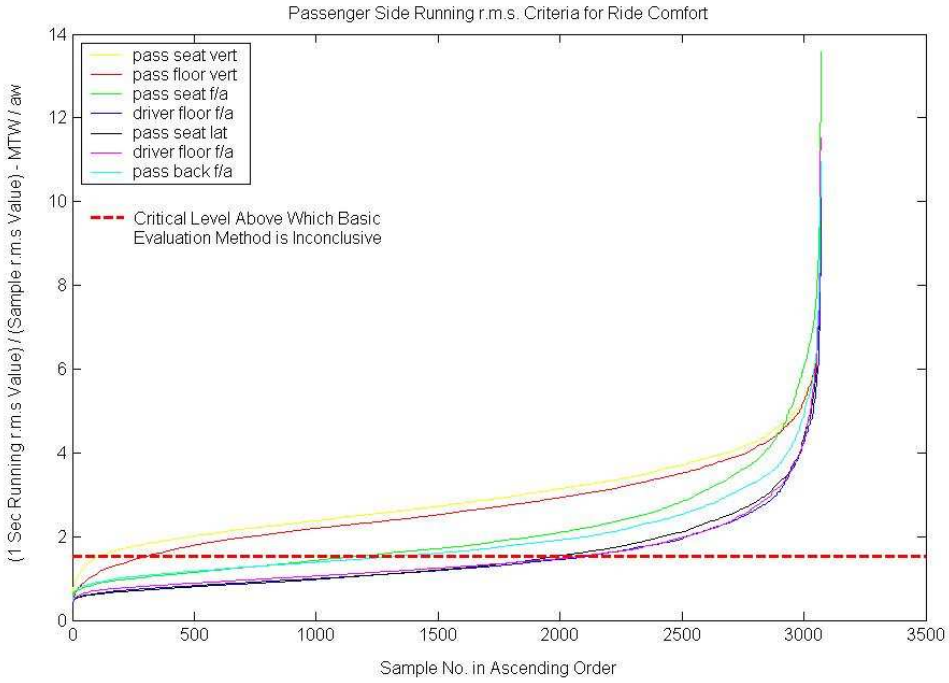

Figure 2.10 Acceleration ratio: passenger side

Even a conservative estimate using only the basic evaluation technique clearly showed the inadequacy of the contemporary low-cost vibration isolators that are in use and thus provided a motivation for further investigation into the design of better vibration isolators.

CHAPTER 3. Proposed novel pneumatic suspension

From the field test project and literature survey of the contemporary suspension systems, it is evident that additional research is necessary in the development of an isolation technology capable of economic operation while delivering superior performance over a broad spectrum of vibration environments. With this as motivation, a preliminary pneumatic suspension technology was proposed in (66). As a part of this study, the concept and the analysis validating a continuously variable natural frequency and damping (CVNFD) isolation technology using the components specified in (66) is included. This chapter presents the components that make-up this novel pneumatic isolation technology.

Using this CVNFD concept, a low cost, mechanically controlled pneumatic isolation device termed "LCPID" (Low cost pneumatic isolation device) was invented in (67), but, has not been included as a part of this thesis due to patent considerations. Instead, this thesis focusses on a more sophisticated electronically controlled closed-loop configuration of the CVNFD based pneumatic vibration isolation system. In the later chapters it will be shown that this intelligently controlled system utilizing displacement and velocity feedbacks demonstrates excellent vibration isolation qualities. The main advantages of this system compared to the fully active suspension systems are that it is not bulky and it is considerably more economical, since, it requires only a minute fraction of the power to operate (maximum 20 watt). Also, its advantage over the economical magneto rheological damper (MR-damper) based semi-active suspension is its capability to alter its natural frequency along with its ability to provide variable damping. *For the reader's*

reference, the magneto-rheological (MR) fluid technology is based on the fact that when a small DC electric current passes through fluid containing tiny particles of carbonyl iron, the floating particles instantly line up in rows that make the fluid rigid thereby providing resistance to motion (damping). When the current stops, it becomes fluid again.

The following section explains the limitations of the present state-of-the-art in vibration isolation systems from a mathematical standpoint to provide credibility to the argument made above regarding the limitations of the contemporary systems.

3.1 State-of-the-art isolation systems and their limitations

Figure 3.1 depicts the transmissibility of a typical single degree of freedom vibratory system as a function of the ratio of excitation frequencies and natural frequencies. Two regions can be identified along the frequency axis.

- ***Region A*** *is the operational region for typical traditional isolation systems.*
- ***Region B*** *represents a region of enhanced isolator operation whereby isolator performance would be significantly improved by using appropriately designed isolator components.*

The curves demonstrate the requirement that isolator natural frequency must be tuned to values significantly lower than the major excitation frequency to which the system is subjected in order to switch to region B of operation.

Traditional isolator systems that utilize constant natural frequency and damping values are forced to operate in region A along a constant damping value curve. The more recent semi-active vibration isolation systems incorporate components that operate at a single natural frequency level, but, possess a variable damping capacity. One such isolator is the semi-active pneumatic suspension utilizing a MR damper. The MR damper is easy to incorporate into the suspension thereby alleviating many of the drawbacks of

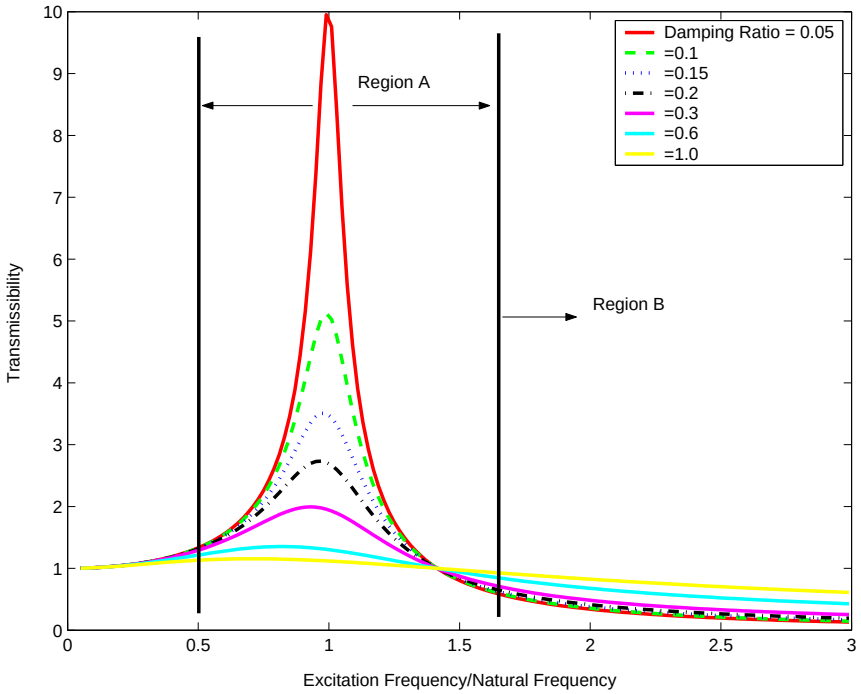

Figure 3.1 Transmissibility curves for a suspended mass with base excitation

the fixed-point traditional suspension design (31), (32), and (33). This allows isolation activity over a broad range of region A, culminating in improved performance.

Even though more flexibility is achieved in region A due to the variable damping capability, the semi-active suspensions with the MR damper however cannot, on demand, extend the region of operation to include region B due to their inability to alter the natural frequency of the system. Many other state-of-the-art suspensions in the market suffer from similar drawbacks. The single exception to the preceding argument is the modern hydraulic isolator that provides a broad range of natural frequencies and damping values, but, at a prohibitive cost in terms of money,maintenance and power requirements. The fully active Bose system mentioned in chapter 1 is also aimed only at high-end vehicles, which shows its similarities to the hydraulics based units in terms of drawbacks.

The CVNFD isolator offsets the drawbacks of both the MR-damper based semi-active system and the fully active type of units due to its ability to

continuously vary the damping and natural frequency of the system without needing exorbitant power for functioning. The following section explains the CVNFD concept and the components used to achieve continuously variable natural frequency and damping.

3.2 CVNFD technology

The idea behind the CVNFD system design is to utilize standard components where ever possible so as to reduce the cost of the system, but, at the same time, improve its functionality by adding additional components intelligently to enhance their characteristics. Fundamental analysis of this novel pneumatic CVNFD isolator concept based on mathematical principles is presented in the next chapter.

3.2.1 System components

The fundamental concept behind the pneumatic CVNFD system is to provide a 2-parameter (natural frequency and damping) isolation system so that a wide range of performance can be achieved. The basic components for the open loop isolator system are listed with a brief explanation of their functioning .

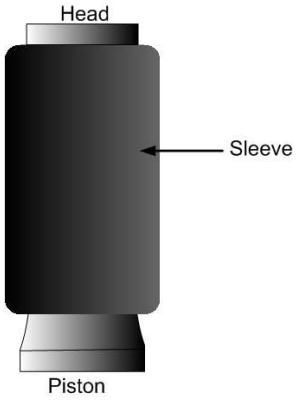

Figure 3.2 Typical sleeve type airspring used in pneumatic isolator systems

Airspring: As noted in chapter 1, the airspring is a central component in pneumatic isolators including the CVNFD system. Figure 3.2 shows a schematic of a sleeve type airspring. The spring contains 3 fundamental components - head, piston, and sleeve. The base of the rubber sleeve is fastened to the top of the piston and rolls along the lateral surface of the piston allowing vertical motion of the head. As mentioned earlier, sleeve type airsprings are usually used for seat/cab suspensions and have a thin rubber fabric to help reduce the overall stiffness of the spring. The airspring behaves much the same as a mechanical spring, a fact which is verified by linearizing the equations that govern air spring transient motions. It will be shown in Chapter 5 that the airspring in the proposed CVNFD system, also functions as a pneumatic damper.

The variable orifice system: Damping is achieved by placing a sharp-edged orifice with a variable orifice area in the pneumatic flow tube connecting the airspring and the accumulator (Fig. 3.3). Continuously varying damping capability is generated by controlling the degree of airspring-accumulator air exchange. Unlike oil-dampers, where damping is produced due to the conversion of kinetic energy into heat energy, pneumatic damping produced in the CVNFD system depends on the instantaneous pressure differential that exists across the orifice, which in turn depends on the orifice geometry. The mathematical equations governing the damping behavior for one such orifice, the sharp edged orifice, is derived from first principles of thermodynamics and is shown in the next chapter and experimentally corroborated (as will be shown in chapter 5).

Accumulator and volume modulator: The accumulator volume (Fig. 3.4) in a CVNFD system is used to set the natural frequency of the isolator (see Eq. 4.5). It is a fixed-wall container connected to the airspring by means of a flow tube, allowing unrestricted air flow to and from the airspring. In order to achieve the continuous change

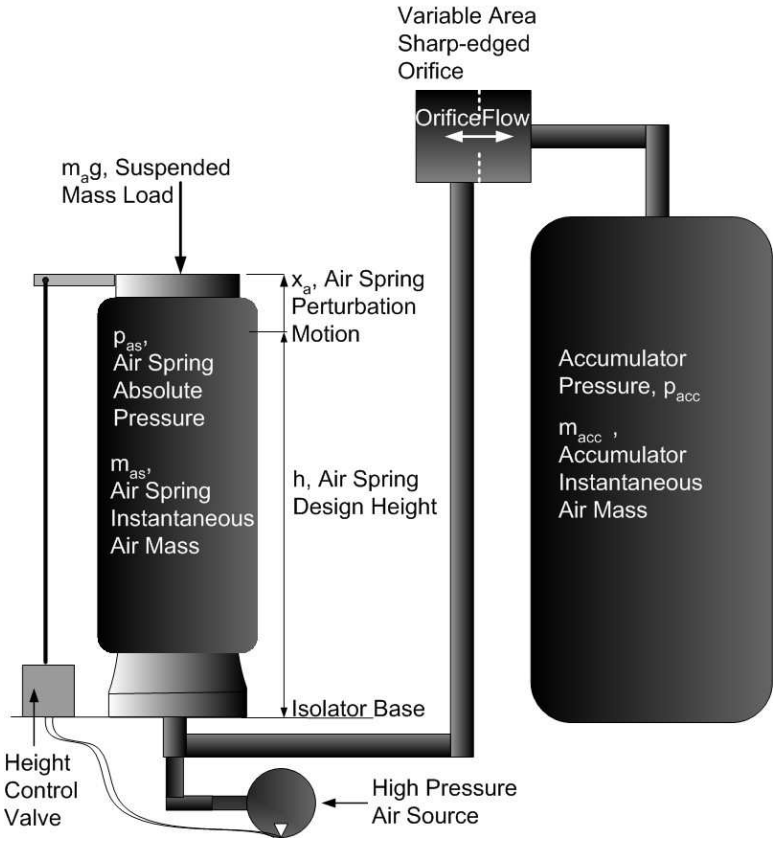

Figure 3.3 CVNFD isolator depicting airspring, variable orifice, and accumulator

in natural frequency, a volume modulator (Fig. 3.4) is used. The volume modulator is a piston-like mechanism capable of isolating selected regions of the accumulator on demand, thus providing a variable accumulator volume. The modulator piston has electronically controlled valves that allow unrestricted airflow between the useful and isolated volumes of the accumulator only when the piston moves. When the piston has moved to its new desired position, the valves close thereby resulting in a new accumulator volume. A mathematical relationship between the accumulator volume and the natural frequency of the system is derived in the next chapter and is experimentally validated (chapter 5).

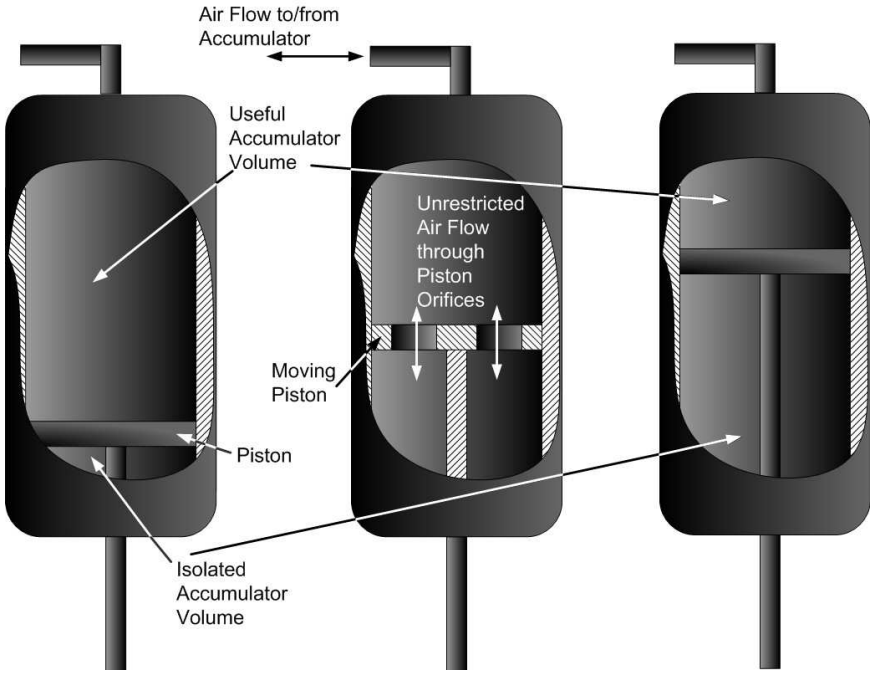

Figure 3.4 Accumulator volume modulator

Height control valve: A height control valve (Fig. 3.3) is placed between the suspended mass and the base of the airspring to guarantee that the mass remains, on average, at a prescribed height above the airspring base. As explained in section 1.2, the main advantages of airspring are its ability to maintain a constant static height under varying load conditions and the height control valve is the component that makes this possible. The height control valve is designed with sufficient time delay so as to have a dynamic response that does not affect the transient motion of the suspended mass.

3.3 Experimental test-setup

A test apparatus for validating the computational simulation results defining the CVNFD isolator system performance was designed. The prototype experimental test rig built is as shown in Fig. 3.5. The main components making up the test rig were the shaker table, I-beam hard back, precision machined linear motion path with pillow

blocks and bearings, pneumatic suspension with airspring, accumulator, variable orifice and height control valve and sprung (suspended) mass. The instrumentation side of the setup comprised of a computer equipped with a data acquisition board, dynamic signal analyzer, displacement sensors, linear velocity sensors and accelerometers.

3.3.1 Mechanical/electro-mechanical components

Shaker: A electro-dynamic shaker table (Unholtz-Dickie T-206) served as a vibration motion base. For the present study, the shaker was used to replicate sine waves from a spectrum analyzer to perform sine sweeps for system identification and also to replicate an arbitrary ride profile typical of real-world base excitation inputs.

Linear motion path/hard-back: A linear motion path (the two vertical steel shafts seen behind the suspended mass in Fig. 3.5) was constructed using a linear ball bearing type motion path. As compared to typical industry suspension designs, which employ a scissors type mechanism, the linear guides provide smoother, stiction free sliding of the suspended mass. The steel shafts were precision aligned and machined to an accuracy of 0.001 inch to reduce any friction forces. The high accuracy machining is necessary to eliminate any obstruction to motion of the suspended mass. A heavy I-beam hard back was also constructed to support the linear motion path for the suspension assembly. The main function of the hard back was to prevent any transverse loading on the linear motion path by allowing motion to occur only in the vertical direction.

Sprung (suspended) mass: The suspended mass was built in the fashion of a carriage to which a series of steel plates weighing 200 lb were secured as dead-weight. The chassis was fastened onto a vertical plate with pillow blocks attached to it on the rear side. The carriage slid vertically along the linear motion path with the help of a set of linear ball bearings housed in these pillow blocks.

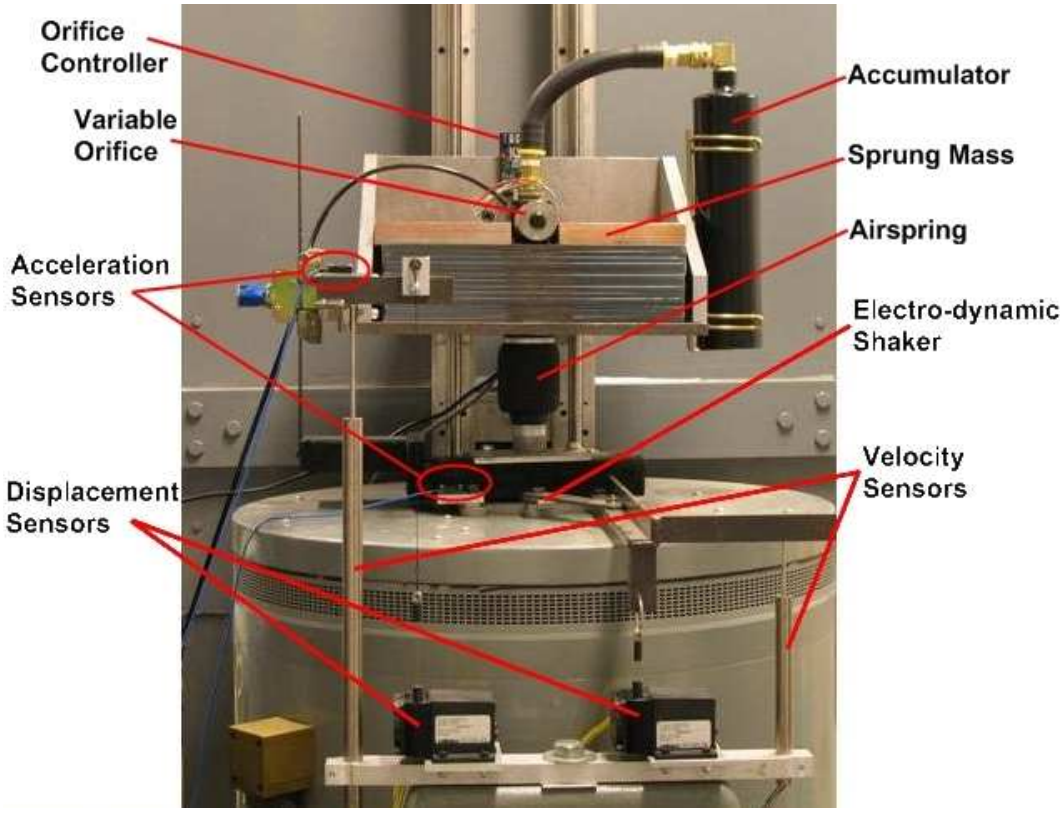

Figure 3.5 Experimental test-rig

Airspring/ Accumulator: The isolator system incorporated a Goodyear $IS3-011$ sleeve type airspring capable of supporting up to 400 lbs. As mentioned in chapter 1, the sleeve type airsprings are suited for light-medium duty applications such as seat/cab suspensions. The main advantage of the sleeve type airspring is that it has a relatively long stroke of actuation and the rubber fabric is not very stiff, thereby keeping the natural frequency of the suspension low.

The accumulator component consisted of a fire extinguisher canister with its threaded end connected for air exchange capability with the airspring. The diameter of threaded end was chosen to be large ($3/4inch$) for aiding unrestricted flow. Accumulator volume was set at a maximum value of 4 times the airspring volume with the capability of varying its volume with the help of a volume modulator.

Variable orifice valve: Choosing the right orifice mechanism was the single most important criteria for achieving the continuously variable damping phenomenon. This is due to the fact that the density of air is much less as compared to that of oil, for any particular orifice size, air will escape with lesser resistance than oil. Hence, the pneumatic damping effect changes drastically with incremental orifice opening. A proportional solenoid manufactured by Teknocraft Inc (Figure 3.6) with a maximum diameter of 3/8 inch and a resolution of $1/1000^{th}$ of an inch was found to be suitable for the application at hand.

Figure 3.6 Teknocraft proportional solenoid valve

Displacement sensors: Compact cable-extension transducers (Celesco PT1A) was chosen for absolute displacement measurements of both the base and the sprung mass. Using a high cycle plastic-hybrid potentiometer, the PT1A provides a precision

voltage divider position feedback signal for full-scale measurement ranges from 2 to 50 inches. Thus, the sensor's high degree of accuracy, linearity and repeatability made it a suitable displacement measurement and feedback device for the pneumatic suspension application.

Velocity sensors: Linear Velocity Transducers (Transtek inc, Series 100) were chosen for velocity measurements. These transducers provide a simple yet accurate means of measuring linear velocity. They consist of high coercive force permanent magnet cores which induce sizable DC voltage while moving concentrically within shielded coils. The basic design permits operation without external excitation, while the generated output voltage varies linearly with core (magnet) velocity. The main features of this transducer are, Self-Generating DC Voltage Output, High Sensitivity, Magnetically Shielded and High Frequency Response making them ideal for any application where an instantaneous velocity measurement is required.

Acceleration senors: High sensitivity DC accelerometers (PCB piezotronics) were used for acceleration measurements of both the base and the suspended mass. These accelerometers utilize a MEMS (Micro-Electro-Mechanical Systems) silicon sensor connected as a bridge element in the circuit. The electrical characteristics of one portion of the bridge increases while the other decreases, when exposed to acceleration. These particular accelerometers provide a dc or steady state acceleration measurement capability as opposed to a predetermined low frequency cut off associated with charge or ICP type accelerometers. Hence, they were chosen to be most suitable for suspension testing where frequencies as low as 1 Hz are included in the operational range.

Data acquisition: Hardware/computer interaction was provided by means of an R&D controller board (dSpace DS1104). The board comprising of 8 D/A and 4 A/D channels was capable of sampling at 10,000 Hz. The DS1104 basically upgraded the

desktop computer to a powerful development system for rapid control prototyping. The Real-Time Interface utilized by the software provides Simulink blocks for graphical configuration of A/D, D/A, digital I/O lines, incremental encoder interface, etc, making control design and testing user friendly. Another important equipment that was used for data acquisition was a Two-Channel Dynamic Signal Analyzer (Stanford Research Systems SRS785). This analyzer was mainly used for performing sine sweeps to ascertain the natural frequency and damping behavior of the CVNFD system (Chapter 5).

CHAPTER 4. Nonlinear mathematical modeling

The proposed pneumatic vibration isolation system is modeled as a single degree-of-freedom spring-mass-damper system subjected to base excitation. The development of the equations of motion for this system is accomplished in two parts. The first part deals with the dynamics of the suspended mass in response to the terrain surface and is given by the inertial motion equation for the suspended mass. The second part refers to the equations that govern the thermodynamics of the airspring- accumulator-orifice mechanism. The next two sections provide a detailed modeling of these governing equations.

4.1 Modeling of suspended mass motion

The pneumatic processes that govern the performance of the isolator are inherently nonlinear and irreversible. The fidelity of the pneumatic system model depends on the extent of the computational complexity in the algorithm which captures the nonlinear mechanical and thermodynamic behavior. The following assumptions are made in establishing the inertial equation of motion:

Assumptions: (1.) Mechanical friction associated with the motion of the sleeve in the airspring is assumed to act as a damper in parallel with the airspring; (2.) The gas process that defines the relationship between pressure and specific volume in both the airspring and accumulator volumes is given by the adiabatic, isentropic relationship ($pv^{\gamma} = c$).

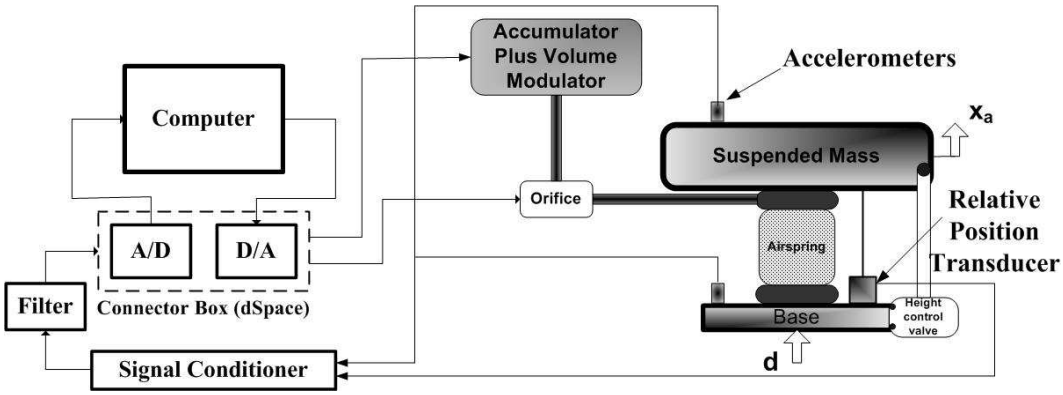

Figure 4.1 Schematic of pneumatic suspension

The following notation is used to delineate the various parameters used in describing the behavior of the airspring: p_{amb} - ambient pressure acting on the exterior piston head surface; p_{as} - absolute pressure of the air mass contained within the air spring sleeve; x_{as_o} - design height of the airspring that suspends mass, m_a; a_{as} - diameter of the airspring; and x_a - perturbation extension of the airspring during transient motion. An instantaneous airspring internal pressure magnitude is governed by the classic isentropic process equation given by $(p_{as}(\upsilon_{as})^{\gamma} = c)$ where, υ_{as} is the specific volume of the air mass contained within the airspring; γ is the specific heat ratio (=1.4); c is the isentropic Flow Constant; and m_{as} - mass of air contained in the airspring.

The equation of motion for the airspring/suspended mass combination can then be derived from Newton's second law as shown in Eq.(4.1):

$$\ddot{x}_a = \left(\frac{p_{as}a_{as}}{m_a}\right) + \frac{C_a}{m_a}(\dot{d} - \dot{x}_a) - g \tag{4.1}$$

$$\text{where,} \quad x_{as} = (x_{as_o} + x_a - d) \tag{4.2}$$

$$p_{as} = c\left(\frac{a_{as}x_{as}}{m_{as}}\right)^{-\gamma} \tag{4.3}$$

Neglecting the damping term and linearizing Eq.(4.1) about the equilibrium height of the airspring (x_{as_o}) yields an equation that closely predicts airspring/suspended mass transient motions and is as obtained in Eq.(4.4):

$$\ddot{x}_a + \left[\frac{c}{m_a} \frac{\gamma}{x_{as_o}} \left(\frac{a_{as} x_{as_o}}{m_{as}} \right)^{-\gamma} a_{as} \right] x_a = 0 \tag{4.4}$$

From the second order equation as obtained above, the characteristic transient motion of the air spring/suspended mass is noted to be sinusoidal with a natural frequency of

$$\omega_n = \sqrt{\frac{c}{m_a} \frac{\gamma}{x_{as_o}} \left(\frac{a_{as} x_{as_o}}{m_{as}} \right)^{-\gamma} a_{as}} = \sqrt{\frac{c\gamma}{m_a} a_{as} \left(\frac{m_{as}}{V_{as}} \right)^{\gamma}} \tag{4.5}$$

The term V_{as} represents the equilibrium volume of the air spring. The natural frequency of an airspring/ suspended mass system with a fixed design diameter, a_{as}, is strongly dependent on airspring volume which makes a_{as} a primary design parameter. By changing the volume of the airspring, the natural frequency can be changed even under fixed suspended mass magnitude.

This change in volume can be achieved in real life by connecting the airspring to a variable volume accumulator. Natural frequency decreases with increasing airspring volume and vice versa. In the above analysis, the damping due to wall forces of the airspring were neglected since the determination of natural frequency through linearization is not affected by the uncoupled constant damping term which appears independently.

4.2 Modeling of orifice mechanism

Another critical component of the CVNFD suspension unit is the variable orifice mechanism. A variable area sharp edged orifice, a standard in fluid flow control, is used to control the mass flow rate of air between the airspring and the accumulator to provide damping to the system. It is a well known fact that when a fluid encounters a constriction such as an orifice, a pressure differential is created across the constriction. This pressure differential causes the flow of air through the constriction (orifice) causing a phenomenon that appears as damping. The flow through this orifice is highly nonlinear and irreversible due to the compressible nature of air.

Description	Symbol	Symbol
Cross section avg velocity	υ_1	υ_2
Pressure	p_1	p_2
Fluid cross section area	A_1	A_2
Fluid density	ρ_1	ρ_2
Total energy/mass	E_1	E_2
Elevation above datum	z_1	z_2

Table 4.1 Parameters for flow analysis through a D/P meter

To help understand the damping phenomenon for such a compressible medium, the flow across the orifice is modeled using first principles of Thermodynamics as well as empirical co-relations (64). The ensuing mathematical derivation has been reproduced from (64) for the reader's reference as well as to help co-relate the generic variables of the derivation with those for the pneumatic system investigated.

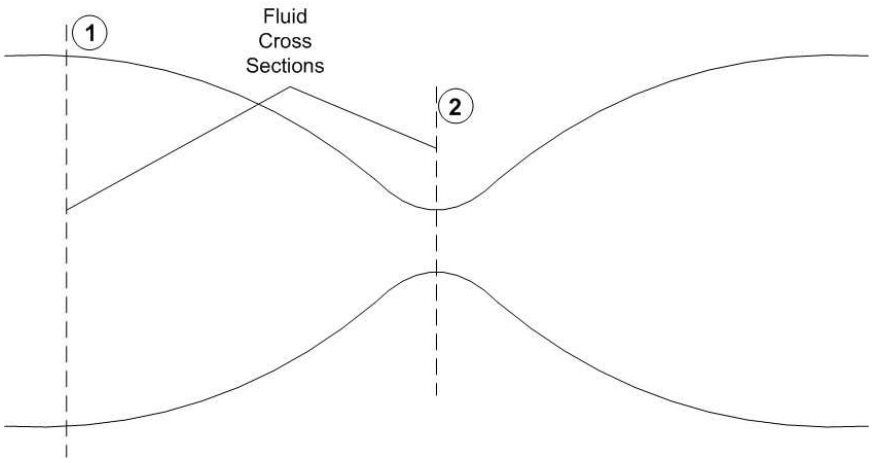

Figure 4.2 Schematic of D/P meter

Consider a flow through a differential pressure flow (D/P) meter as shown in Fig. 4.2. The constriction causes a reduction in the cross sectional area of the fluid. Relevant quantities are given in table 4.1.

The following assumptions enable a theoretical calculation of pressure difference to

be made.

- Frictionless flow- i.e no energy losses due to friction, either in the fluid itself or between the fluid and the pipe walls.
- No heat losses or gains due to heat transfer between the fluid and its surroundings.
- Conservation of total energy and total volume flow rate are valid.
- Pressure-volume changes between cross-sections 1 and 2 of the D/P meter are assumed to be adiabatic.

Using conservation of total energy (pressure + kinetic + potential) one can obtain Eq. 4.6.

$$E_1 = \frac{p_1}{\rho_1} + \frac{1}{2}\upsilon_1^2 + gz_1 = E_2 = \frac{p_2}{\rho_2} + \frac{1}{2}\upsilon_2^2 + gz_2 \tag{4.6}$$

Since, the pressure-volume changes between cross-sections 1 and 2 are assumed to be isentropic, the relation as shown in Eq. 4.7 can be obtained.

$$\frac{p_1}{\rho_1^{\gamma}} = \frac{p_2}{\rho_2^{\gamma}} \tag{4.7}$$

where, γ = specific heat ratio C_p/C_v.

Also, since the pipe is horizontal, we have $z_1 = z_2$. Hence Eq. 4.6 becomes

$$\frac{\gamma}{\gamma - 1}\frac{p_1}{\rho_1} + \frac{1}{2}\upsilon_1^2 = \frac{\gamma}{\gamma - 1}\frac{p_2}{\rho_2} + \frac{1}{2}\upsilon_2^2 \tag{4.8}$$

When $p_1 > p_2$, $\rho_1 > \rho_2$ i.e. the fluid expands, $Q_2 > Q_1$ and volume flow rate is not conserved. However, there is conservation of mass flowrate $\dot{m}$.

$$\dot{m}_1 = \upsilon_1 A_1 \rho_1 = \dot{m}_2 = \upsilon_2 A_2 \rho_2 \tag{4.9}$$

From Eqs. 4.7, 4.8 and 4.9, the theoretical mass flow through a D-P mater can be established as shown in Eq. 4.10.

$$\dot{m}_{th} = \varepsilon \frac{A_2}{\sqrt{1 - \left(\frac{A_2}{A_1}\right)^2}} \sqrt{2\rho_1(p_1 - p_2)} \tag{4.10}$$

where, ϵ = compressibility factor and is given by,

$$\varepsilon = \sqrt{\left(\frac{\gamma}{\gamma-1}\right) p_1 \left(\frac{p_2}{p_1}\right)^{\frac{2}{\gamma}} \left(\frac{1-\left(\frac{A_2}{A_1}\right)^2}{1-\left(\frac{A_2}{A_1}\right)^2 \left(\frac{p_2}{p_1}\right)^{\frac{2}{\gamma}}}\right)} \tag{4.11}$$

The above equation for theoretical mass flow does not account for many losses that occur in real world such as while using an orifice plate. Also, the orifice plate is a sudden constriction, which causes the fluid area to be about 0.6 times the area at the vena contracta. For these reasons, a general and practical equation for differential pressure flow meter, metering any clean liquid or gas can be obtained by multiplying the theoretical mass flow equation with a discharge co-efficient (C) which is normally obtained from empirical co-relations and is given by Eq. 4.12.

$$\dot{m}_{act} = C\varepsilon \frac{A_2}{\sqrt{1-\left(\frac{A_2}{A_1}\right)^2}} \sqrt{2\rho_1(p_1-p_2)} \tag{4.12}$$

For the case at hand, region 1 of the D/P meter corresponds to the airspring side and region 2 corresponds to the accumulator side of the system. Hence, the following notation is used for the orifice equation.

$$p_1 = p_{as}, \quad p_2 = p_{acc}, \quad \dot{m}_{act} = \dot{m}_{as}$$

$$\rho_1 = \rho_{as}, \quad A_1 = a_{as}, \quad A_2 = a_o \tag{4.13}$$

where, the parameters p_{as}, m_{as}, p_{acc}, m_{acc} represent the absolute pressure and air mass in the airspring and accumulator, respectively. The term m_{total} is the total air mass contained in the airspring/ accumulator combination and V_{acc} is the accumulator volume. x_{as} is the actual length of the airspring and d is the base excitation amplitude (positive up). The parameters c_d , a_o , and x_{acc} represent the orifice coefficient, orifice instantaneous area, and instantaneous accumulator piston position, respectively.

Note: Equation 4.12 describes flow rate in only one direction, i.e. when $p_1 > p_2$. For the other case, this equation is undefined. Since, any side of the D/P meter can be

assumed to be p_1 or p_2, a slight modification of the above equation will make it capable of capturing bi-directional flow through the orifice. The simplest way to achieve this is by the use of the absolute function as shown by the term L_4 in Eq. 4.14.

Combining and simplifying Eqs. (4.11,4.12) and substituting the appropriate variables from Eq. 4.13, the actual mass flow rate equation can be obtained as shown in Eq.(4.14):

$$\dot{m}_{as} = \frac{L_1 L_2 L_4}{L_3} \tag{4.14}$$

where,

$$L_1 = c_d a_0 \left(\left[\tfrac{2\gamma}{\gamma - 1} \right] \left[\tfrac{p_{as} m_{as}}{a_{as} x_{as}} \right] \right)^{0.5} \qquad L_3 = \left(1 - \left(\tfrac{a_o}{a_{as}} \right)^2 \left(\tfrac{p_{acc}}{p_{as}} \right)^{2/\gamma} \right)^{0.5}$$

$$L_2 = abs \left(\left[\tfrac{p_{acc}}{p_{as}} \right]^{2/\gamma} - \left[\tfrac{p_{acc}}{p_{as}} \right]^{(\gamma+1)/\gamma} \right)^{0.5} \qquad L_4 = \tfrac{(p_{acc} - p_{as})}{abs(p_{acc} - p_{as})}$$

$$p_{acc} = c \left(\tfrac{V_{acc}}{m_{acc}} \right)^{-\gamma} \qquad m_{acc} = (m_{total} - m_{as})$$

$$x_{as} = (x_{as_o} + x_a - d) \quad , V_{acc} = x_{acc} a_{acc}$$

The nonlinear equations of motion for a suspended mass/accumulated-airspring combination with a variable area orifice are given by Eqs. (4.1) and (4.14). These equations govern the behavior of the suspended mass for the applied excitation input. The instantaneous orifice size, a_o, and instantaneous accumulator piston position, x_{acc} (i.e. length of accumulator volume), are external control inputs to achieve a continuously variable change in natural frequency and damping.

The computational study conducted on the mathematical model of the pneumatic system and experimental validation of the system dynamics are explained in detail in the next chapter. The intention was to first understand the behavior of the system computationally by making use of well established analysis relations for low-order systems, and then to use this information to experimentally validate the concept, and to also tune the analytical model for control system design purposes.

CHAPTER 5. Analysis of the nonlinear model

5.1 Relevant background

Transient-response of second order systems: In many practical cases, the desired performance characteristics of control systems are specified in terms of time-domain quantities. Another very important aspect of time-domain analysis is that they can be used for system identification. Although, closed-form expressions in the time-domain do not exist for higher order systems, a second order system can be uniquely identified from step response analysis.

The requirement that a system be of second order is quite restrictive. However, many higher order systems have a predominantly second order behavior over a range of operation and the concepts of dominant pole approximation could be utilized to reduce these higher order system to a second order for analysis. It will be shown in the following sections that the CVNFD system behaves like a second order over a significant domain of operation and that step response analysis yields sufficiently accurate information of its behavior. Some relevant time-response characteristics of second order systems that have been used for damping and natural frequency calculations of the CVNFD system are mentioned here first for the reader's reference.

Settling time characteristic: We know from several undergraduate texts that for an undamped second order system, the transient response is obtained from Eq.5.1.

$$y(t) = 1 - \frac{e^{-\zeta\omega_n t}}{\sqrt{1-\zeta^2}} \sin\left(\omega_d t + \tan^{-1}\frac{\sqrt{1-\zeta^2}}{\zeta}\right) \forall t \geq 0 \tag{5.1}$$

where, ζ = damping ratio; ω_n = natural frequency and ω_d = damped natural frequency.

The curves $y(t) = 1 \pm (e^{-\zeta\omega_n t}/\sqrt{1-\zeta^2})$ are the envelope curves of the transient response to a unit-step input. The response curve y(t) always remain within a pair of envelope curves, as shown in Fig. 5.1. The time constant of theses envelope curves is $1/\zeta\omega_n$.

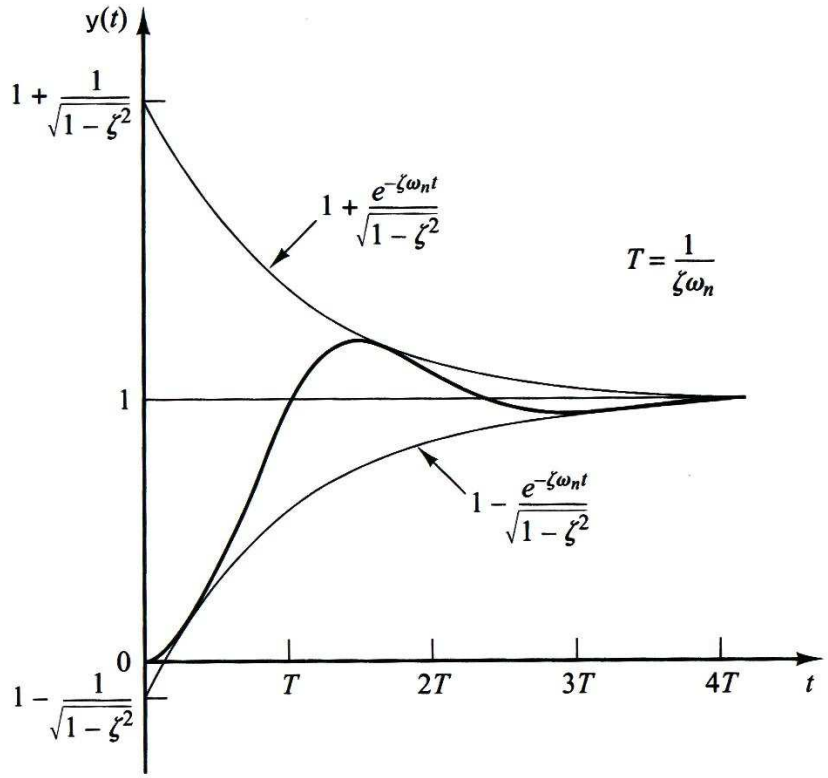

Figure 5.1 Time constant: Second order system

The speed of decay of the transient response depends on the value of the time constant $1/\zeta\omega_n$. For a given ω_n, the settling time t_s is a function of the damping ratio ζ. We have that for the same ω_n and for a range of ζ between 0 and 1, the settling time t_s for a very lightly damped system is larger than that for a properly damped system.

The settling time corresponding to a $\pm 2\%$ *or* $\pm 5\%$ tolerance band may be measured in terms of the time constant $T = 1/\zeta\omega_n$ for different values of ζ. For underdamped

systems, if the 2% criterion is used, t_s is approximately four times the time constant of the system. If the 5% criterion is used, then t_s is approximately three times the time constant. Hence, the mathematical relation between the settling time and the time constant is,

$$t_s = 4T = \frac{4}{\sigma} = \frac{4}{\zeta\omega_n} \qquad (2\% \quad \text{criterion}) \tag{5.2}$$

$$t_s = 3T = \frac{3}{\sigma} = \frac{3}{\zeta\omega_n} \qquad (5\% \quad \text{criterion}) \tag{5.3}$$

Maximum overshoot characteristic: The maximum overshoot M_p occurs at the peak time or at t=$t_p = \pi/\omega_d$. Assuming that the final value of the output is unity, M_p can be written as,

$$M_p = y(t_p) - 1$$

$$M_p = \frac{e^{-\zeta\omega_n(\pi/\omega_d)}}{\sqrt{1-\zeta^2}}\left(\cos\pi + \frac{\zeta}{\sqrt{1-\zeta^2}}\sin\pi\right)$$

$$M_p = e^{\left(-\zeta/\sqrt{1-\zeta^2}\right)\pi} \tag{5.4}$$

5.2 Computational study of mathematical model

Computational simulations were performed using matlab/Simulink (Fig. B.3) to validate the analytical model. Equations (4.1) and (4.14) were solved numerically for a unit step input of base deflection, d. A typical airspring was used in the CVNFD model. The airspring had a design height x_{as_o} of 6 inches and a diameter of 3 inches respectively. The suspended mass used in the simulation weighed 200 lb. The accumulator volume was set at 4 times the airspring volume which provided a low natural frequency boundary for the isolator. The maximum orifice was set at $\frac{3}{8}$ inches, which, was observed to be the smallest orifice size that would allow "unrestricted" flow between the airspring and accumulator when fully open. Table 5.1 gives a description and numerical values of all

Description	Symbol	Value	units
Acceleration due to gravity	g	32.17	ft/s^2
Universal process constant	R	53.3	ft/Ra
Atmosphere pressure	P_{atm}	2116	lb/ft^2
Density of air	ρ	0.004265	$slugs/ft^3$
Temperature of air	T	520	Ra
Fictitious damping (Bag forces)	ζ	5%	-
Ratio of specific heats	γ	1.4	-
Isentropic process constant	C	7910673	-

Table 5.1 Values of the system parameters

the other important parameters used in the simulation study. In order to ascertain both the change in natural frequency and damping of the suspension, two different sets of tests were simulated and are explained next.

5.2.1 Fixed accumulator volume case

A series of computational simulations, each with a different orifice size from zero to maximum were performed for the isolator/suspended mass combination in response to a step input of base deflection. For these tests, the accumulator volume was fixed at a constant value of 4 times the airspring volume. Suspended mass transient motion, recorded for each simulation, appeared to consist of combinations of linear motion modes.

Figure 5.2 shows the variation of the CVNFD system time constant (using a 2% settling time criteria) with respect to orifice opening and for different accumulator sizes. From the figure it can be observed that the CVNFD suspension behaves like a second order spring-mass-damper system between 8% and 100% of orifice opening ($\zeta = 0.15$ onwards) and for the above mentioned airspring-accumulator configuration. Hence, the damping ratio ζ was calculated as a function of orifice size using the maximum overshoot criteria for second order systems (Eq. 5.4).

Again using second order system approximation and a 2% settling time criteria,

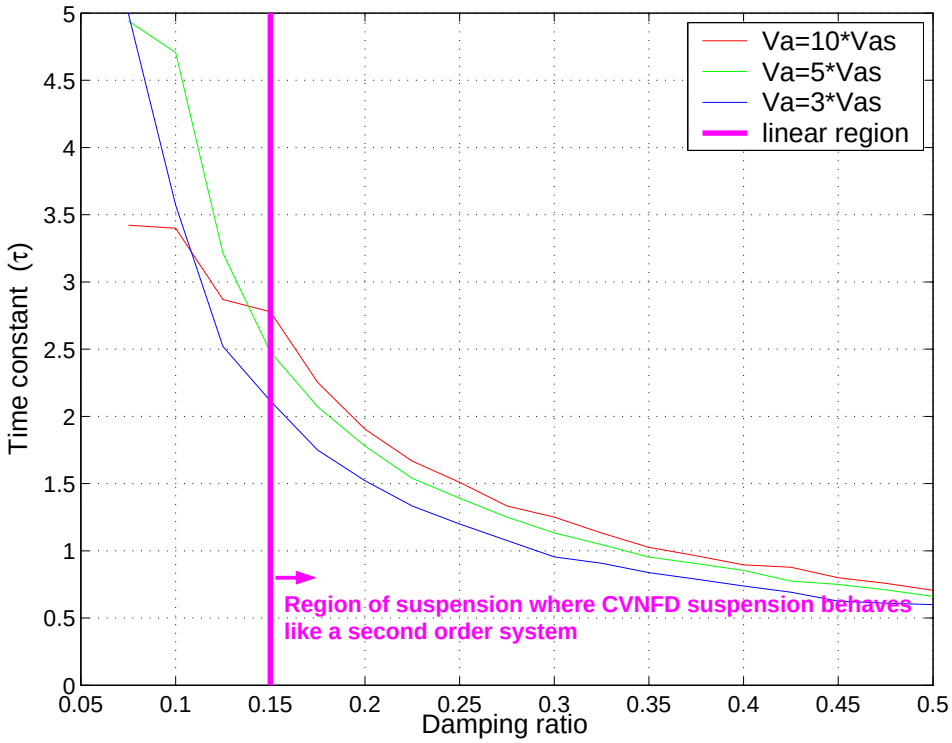

Figure 5.2 Time constant for the CVNFD suspension

the simulation data for each case was processed to extract estimates of isolator natural frequency, ω_n, as a function of orifice size using the Eq. 5.2.

Figure 5.3 depicts the parameter distributions for the computational solutions cited and shows that by increasing the orifice area from zero to about 8%, the damping changes drastically. Even though the damping changes continuously in this region, it is noticed that the natural frequency abruptly changes from its high value to its low value. Hence, the dynamics is predominantly nonlinear and difficult to model. However, for orifice openings 8% and above, the natural frequency of the CVNFD system remains constant at its low value while the damping changes from a high value of 0.7 at 8% orifice open, to less than 0.1 when fully open. This region is, therefore, characterized by a continuously varying damping with a relatively constant natural frequency and is easier to model. The preliminary design studies restrict the CVNFD suspension operation to this region.

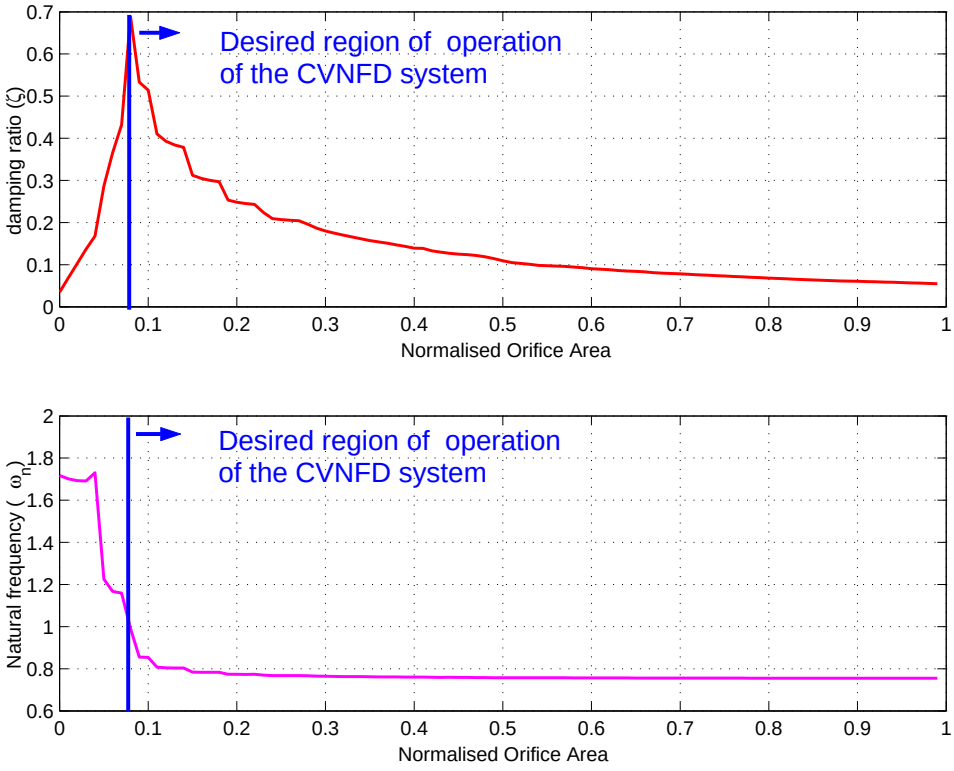

Figure 5.3 Change in ω_n and ζ for fixed accumulator volume and varying orifice area

5.2.2 Fixed orifice case

Similar to the variable orifice study, numerical solutions to Eqs. (4.1) and (4.14) were obtained for a fixed orifice of $\frac{3}{8}$ inch diameter, but the accumulator volume was varied to determine the natural frequency variation characteristics for the CVNFD isolator. A series of computational simulations, each with a different accumulator volume, was obtained for the isolator/ suspended mass combination in response to a step input of the base displacement.

Accumulator volumes ranged from 0 to 10 times the airspring volume. The estimates of isolator natural frequency, ω_n, and damping ratio, ζ, were derived as functions of accumulator volume using the maximum overshoot and 2% settling time criteria for second order systems. Figure 5.4 depicts natural frequency and damping ratio distribu-

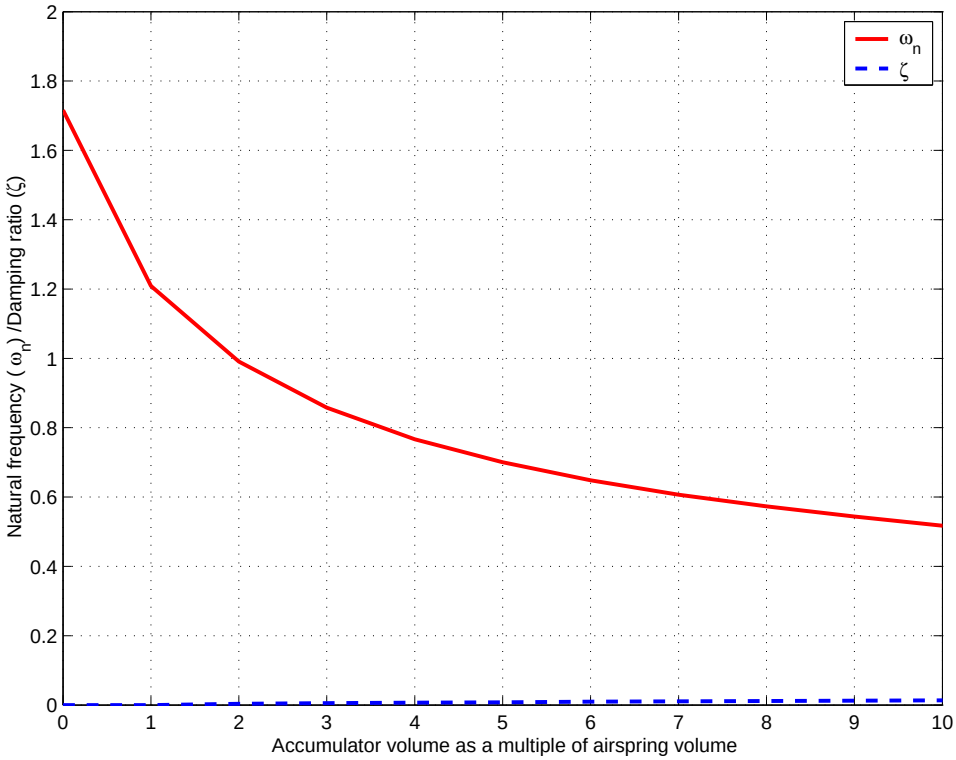

Figure 5.4 Change in ω_n and ζ for fixed orifice area and varying accumulator volume

tions from the computational study. The plots show a wide range of natural frequencies available for isolator performance. On the other hand, damping ratio remains constant for the applicable range of accumulator volumes. Hence, it can be concluded that by changing the accumulator volume while keeping a fixed orifice diameter, the natural frequency can be independently altered.

5.3 Experimental corroboration of mathematical model

In addition to computational study, an experimental validation of the mathematical model was also performed as a part of preliminary study. The experimental setup built for preliminary validation is explained in detail in Section 3.3. As the first step, experimental data was used to assess the fidelity of the nonlinear analytical/simulation model.

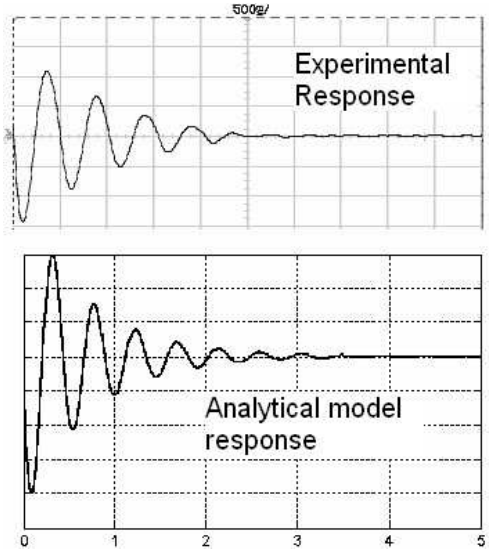

Figure 5.5 Full orifice opening

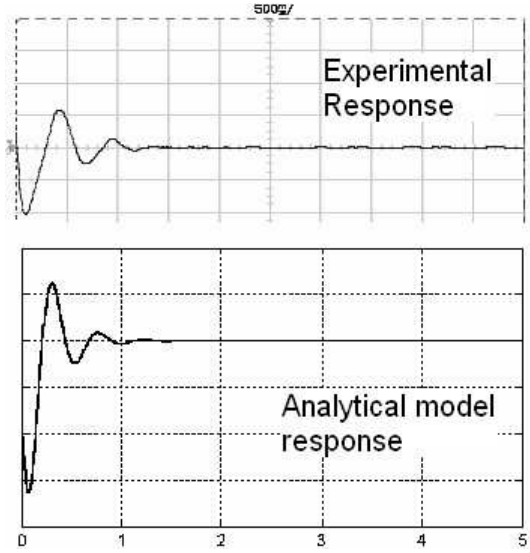

Figure 5.6 15% orifice opening

In the computational study, it was observed that the CVNFD suspension behaved similar to a second order system. Impulse response analysis was performed for both the nonlinear analytical model and on the hardware and the acceleration response of the suspended mass was recorded. For comparison, two orifice settings were used: one maximum orifice opening which corresponds to the minimum damping and the other about 15% orifice opening which corresponds to near maximum damping. The acceleration measurements on the hardware were recorded using accelerometers.

Figures 5.5 and 5.6 show the results for the fully open orifice case and the 15% orifice open case, respectively. It can be observed that the experimental response closely resembles that of the simulations thereby providing a measure of the fidelity of the nonlinear analytical model. To understand the frequency domain behavior properly, the frequency response of the system needs to be examined. This entails using the best available linearized models of the system.

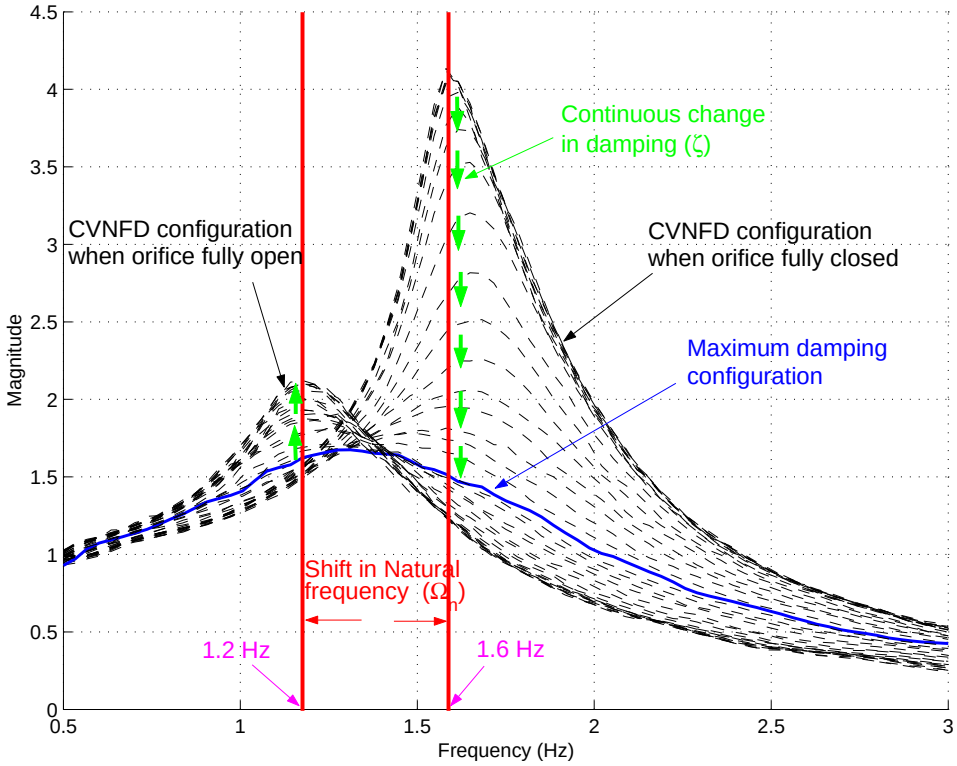

Figure 5.7 Experimental corroboration of CVNFD dynamics

5.3.1 Fixed accumulator volume case

The frequency response of the system was obtained using sine sweep inputs provided by the SRS 785 spectrum analyzer. The transfer function between the suspension base and the suspended mass displacements were recorded for small increments in orifice opening from fully closed to fully open. The result obtained is as shown in Fig. 5.7. Comparing this with Fig. 5.3 shows a good agreement in behavior of the system. When the orifice is completely closed, the natural frequency is at its high value and damping is minimal. On gradually increasing the orifice area up to about 10% open, the natural frequency initially stays constant before changing slightly to an intermediate value where the damping is maximum. This trend was also observed in the computational study. Also, as observed for the analytical case, the damping changes from its minimum to maximum value continuously. On further increasing the orifice opening, the damping

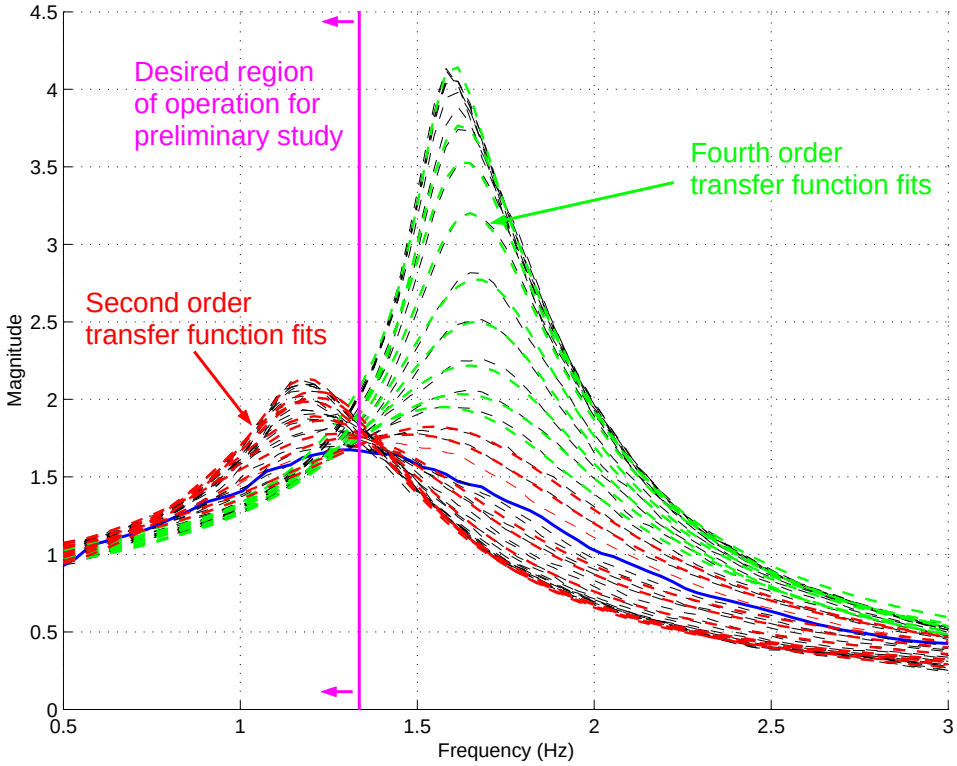

Figure 5.8 Transfer function fits

continuously reduces reaching its minimum value while the natural frequency quickly shifts to its minimum value and stays constant at that value.

In the computational analysis, it was observed that between 15% and 100% orifice openings, the CVNFD isolator behaved like a second order system. This entailed the analysis of the natural frequency and damping calculations from second order approximations. To validate this claim, the frequency response data from Fig. 5.7 was used to fit transfer functions with the help of SOCIT, a software tool designed by NASA for this purpose. Effort was made to fit transfer functions of the smallest order. The resulting fits are as shown in Fig. 5.8. It was observed that for orifice openings less than $6-8\%$, reasonable fits could be obtained only with a fourth order transfer function. However, for orifice openings beyond this value, second order transfer functions were sufficient to capture the important dynamics. This shows that, the CVNFD isolator can indeed be

approximated by a second order system in this region.

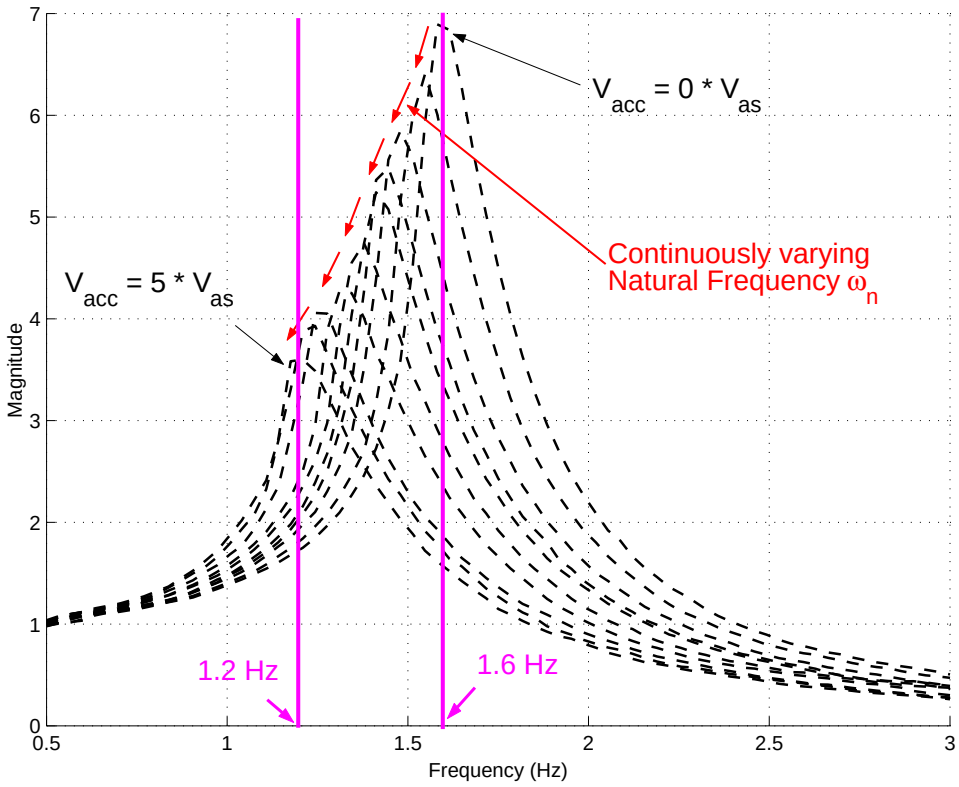

Figure 5.9 Change in ω_n and ζ for fixed orifice area and varying accumulator volume

5.3.2 Fixed orifice case

For a fixed orifice case, a constant orifice diameter of $\frac{3}{8}$ inch was used. With the help of the volume modulator, the accumulator volume was varied in increments from 5 times the airspring volume to zero accumulation to determine the natural frequency variation characteristics for the CVNFD isolator.

Figure 5.9 shows the trend recorded. The natural frequency was around 1.2 Hz for maximum accumulation and reached a value of about 1.6 Hz when the accumulator was shutoff. As in the case of the computational analysis, the change in natural frequency was continuous while the damping did not alter by much and remained at a negligible value

of about $7 - 10\%$. Hence, for the case of a fixed orifice diameter, it can be noticed that by changing the accumulator volume, the natural frequency (second control parameter) could be independently altered.

5.4 Assessment of the analysis

In the previous chapter, a novel concept of CVNFD technology was proposed. The various components making up the system and their functionality were explained in detail. In this chapter, a rigorous mathematical modeling procedure using inertial equations of motion as well as fundamental Thermodynamic concepts was undertaken to capture the essential dynamics of the system. Comprehensive computational simulations were carried out to ascertain the behavior of the new suspension.

A Test rig comprising of all the necessary components was built to perform the required experiments. Experiments were performed primarily with the help of data acquisition boards and the spectrum analyzer. The results obtained closely matched the claims made from the computational study thereby validating the concept of CVNFD technology.

Both from the computational study and experimental analysis it was observed and confirmed that by using the airspring-orifice-accumulator combination, damping could be injected into the suspension per demand without using a dashpot or an MR damper. It was also noted that the same combination could also be used to vary the natural frequency of the isolator independent of the damping when desired.

Although the nonlinear model analyzed in this chapter is able to portray the system dynamics to a considerably good extent, the nonlinear couplings in the model limit its use in control design studies. Since, the effectiveness of the CVNFD technology depends greatly on the real-time control of the system parameters (ζ and ω_n), finding a suitable system model is imperative to the success of the proposed technology. However, the

model so derived must have sufficient fidelity to replicate the dynamics observed in the nonlinear model. To accomplish this objective, the system parameters that can yield a linear model is obtained both through analytical derivation and experimental system identification and is explained in the next chapter. Being of canonical form, the model obtained from these parametric values is suitable for control design purposes and hence, used for designing a model-matching sliding mode control (chapter 8).

CHAPTER 6. Analytical/experimental system identification

6.1 Analytical modeling of pneumatic stiffness

For the purpose of comparison, the widely researched contemporary suspension comprising of an airspring and an electronically controlled MR-damper is used as a benchmark. For the case of the pneumatic suspension, the airspring is modeled analytically and the orifice induced damping variation is obtained through experimental techniques. Due to the unavailability of MR-damper based suspension apparatus, the damper characteristics have been modeled analytically based on manufacturer's specifications. The modeling of the airspring stiffness for the MR based unit is however similar to that of the pneumatic suspension. The following sections cover in detail the modeling of both the airspring as well as the dampers (pneumatic and MR) using fundamental governing laws, empirical co-relations, and experimental techniques.

6.1.1 Airspring modeling

Figure 6.1 shows a schematic of a sleeve type airspring fixed at the base and various forces involved. As mentioned in chapter 3, the air spring behaves much the same as a mechanical spring, as will be shown next.

Force on the head of the Airspring is given by

$$F_{as} = P_{as} a_{as} \tag{6.1}$$

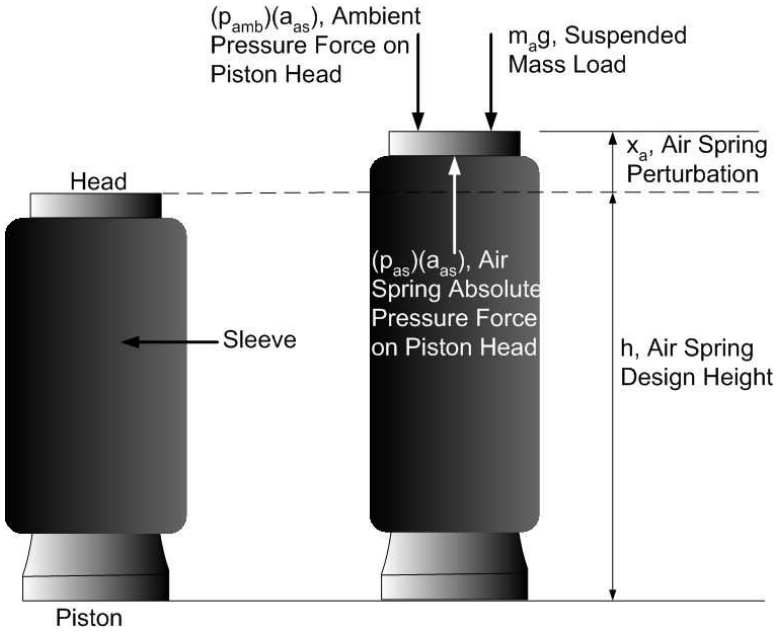

Figure 6.1 Typical airspring used in pneumatic isolator systems

Absolute air pressure inside the airbag can be calculated as

$$P_{as} = P_g + P_{amb} \tag{6.2}$$

$$P_g \rightarrow \text{Gauge Pressure} \qquad a_{as} \rightarrow \text{Airspring area}$$

Spring stiffness, which is defined as the force per unit displacement can be defined for the airspring as,

$$\begin{aligned} K_{as} &= \frac{dF_{as}}{dx_a} = \frac{d(P_{as}a_{as})}{dx_a} \\ &= P_{as}\frac{da_{as}}{dx_a} + \frac{dP_{as}}{dx_a}a_{as} \end{aligned} \tag{6.3}$$

Hence, the stiffness of the airspring is derived from the gas laws governing the pressure and volume relationship.Assuming adiabatic compression, the equation defining the pressure-volume relationship is

$$PV^{\gamma} = P_i V_i^{\gamma} = \text{constant} \tag{6.4}$$

where,

P_i = absolute gas pressure at reference displacement.

V_i = corresponding volume of contained gas.

γ = ratio of specific heats of gas, 1.4 for air.

Differentiating the above process equation wrt x_a, we get

$$\frac{d(P_{as}V_{as}^{\gamma})}{dx_a} = P\gamma V_{as}^{\gamma-1}\frac{dV_{as}}{dx_a} + \frac{dP_{as}}{dx_a}V_{as}^{\gamma} = 0 \tag{6.5}$$

For an airspring, $\frac{dV_{as}}{dx_a} = -a_{as}$ (By sign convention, positive pressure changes are given by positive displacements and, since, positive pressures result from compression we get the negative sign). Re-arranging Eq. 6.5 we obtain,

$$\frac{dP_{as}}{dx_a} = \frac{-P_{as}\gamma V_{as}^{\gamma-1}\left(dV_{as}/dx_a\right)}{V_{as}^{\gamma}} = \frac{-P_{as}\gamma\left(dV_{as}/dx_a\right)}{V_{as}} \tag{6.6}$$

The expression for spring rate was obtained in Eq. 6.3 as,

$$K_{as} = P_{as}\frac{da_{as}}{dx_a} + \frac{dP_{as}}{dx_a}a_{as} \tag{6.7}$$

For a sleeve type airbag, the change in cross-sectional area as the spring actuates is negligible due to the rolling of the sleeve over the piston. Hence, $P_{as}\frac{da_{as}}{dx_a} = 0$. Substituting Eq. 6.6 into the above expression, the spring rate becomes,

$$K_{as} = \frac{dP_{as}}{dx_a}a_{as} = \frac{P_{as}\gamma a_{as}^2}{V_{as}} \tag{6.8}$$

Again, using the definition of isentropic equation we get

$$\frac{P}{\rho^{\gamma}} = C \Rightarrow P = C\rho^{\gamma} \tag{6.9}$$

where, C = Isentropic process constant. ρ = density of air.

From Eq. 6.8 and Eq. 6.9 we the final expression for the stiffness of the spring as,

$$K_{as} = \frac{dP_{as}}{dx_a}a_{as} = \frac{C\rho_a^{\gamma}\gamma a_{as}^2}{V_{as}} \tag{6.10}$$

For a suspended mass of 200 lbs and using the Goodyear(1S3-011) airspring, the spring constant with the accumulator closed was calculated to be K_{as}= 18622 N/m and with the accumulator open was K_{as}= 6207 N/m.

6.2 Experimental identification of pneumatic damping

System identification is the process of extracting a mathematical model of a system using input/output data obtained experimentally. For a linear system, this mathematical model can be written in the form of a transfer function or as an equivalent state-space representation. Due to the modal characteristics of vibratory systems, frequency domain techniques tend to yield better fits to the model than time domain methods and hence, frequency domain system identification techniques are used.

The exercise focused on system identification of the CVNFD system to obtain a linear second order model from which the damping variation could be obtained as a function of the orifice opening for control design. Even though the analytical methods produced excellent estimates of the system natural frequency, with the orifice behavior being highly non-linear, it is more convenient and accurate to obtain an estimate using a system identification process rather than a mathematical derivation. Since, these parametric values will be eventually used for control design, obtaining an accurate system model is key to the robustness and performance that any controller designed can achieve.

Matlab has a built-in command for frequency domain system identification called *invfreqs* which uses least squares error minimization to fit the data. The *invfreqs* function operates under the transfer function framework, so it's output is the numerator and denominator coefficients of the modeled system's transfer function. This method is not well-suited for vibratory systems, since, it has been observed that converting back to modal canonical form degrades the accuracy of the model. This is because, *invfreqs* outputs a model that is very ill-conditioned, even for the case of low order systems. In addition, *invfreqs* is computationally slow.

6.2.1 Obtaining low order models

In view of the drawbacks of the *invfreqs* function, and the necessity to accurately fit a low order transfer function to the CVNFD system dynamics, a more advanced transfer function fitting program called SOCIT was employed.

The results of the system identification process applied to the CVNFD isolation system is as shown in Fig. 6.2. The 4 state continuous-time system obtained from the SOCIT frequency domain identification algorithm has extremely small error when compared with the experimental frequency response data. Dominant pole approximation was then performed to further reduce the system to a second order canonical form using which, the damping was obtained. Figure 6.3, shows the experimentally obtained variation of orifice damping as a function of the voltage applied to the solenoid of the orifice mechanism. The empirical curve fit for this data is given by Eq. 6.11 and its graph is superposed on the experimental data in Fig.6.3.

$$V_{sol} = \left(6.9 - 0.105\left[\frac{(3.5\times10^{-11})e^{29x} - e^{-29x}}{3e^{29x} + 0.05e^{-29x}}\right]\right) \tag{6.11}$$

In the above expression, V_{sol} - voltage to be supplied to the solenoid, $x = \zeta - 0.415$ is a dummy variable, and ζ is the damping ratio demanded by the controller.

6.3 Analytical modeling of magneto rheological damper

Magneto rheological fluids Magneto rheological fluids are materials that exhibit a change in rheological properties (elasticity, plasticity, or viscosity) with the application of a magnetic field. Another class of fluids that exhibit a rheological change is electro rheological (ER) fluids. As the name suggests, ER fluids exhibit rheological changes when an electric field is applied to the fluid. There are, however, many drawbacks to ER fluids, including relatively small rheological changes and extreme property changes with temperature. In comparison, MR fluids only require small voltages and currents,

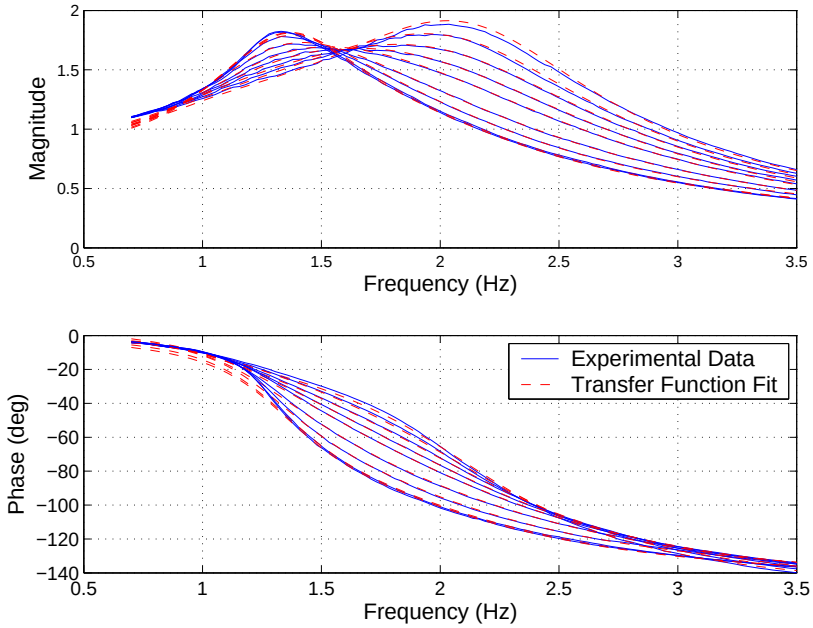

Figure 6.2 System identification of CVNFD isolator

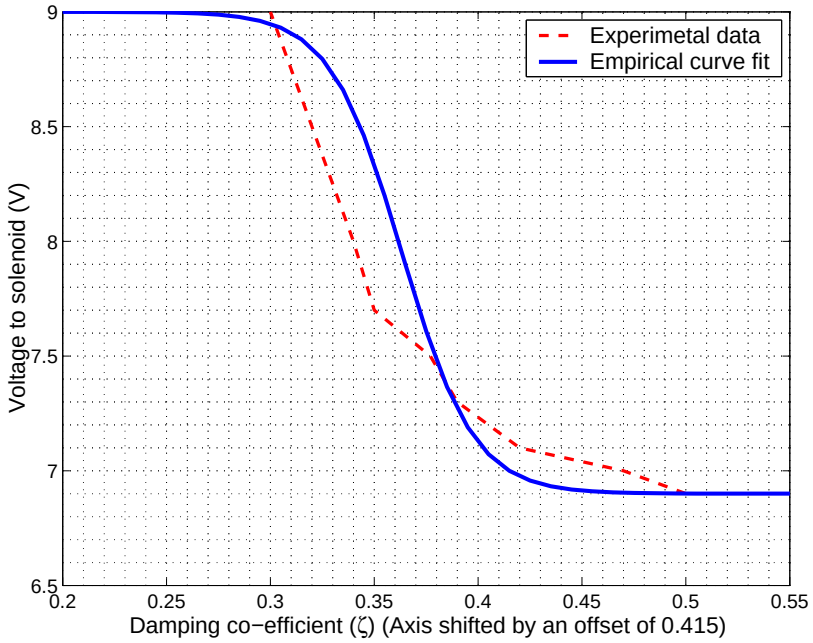

Figure 6.3 Relationship between orifice damping and solenoid voltage

while ER fluids require very large voltages and very small currents. For these reasons, MR fluids have recently become a widely studied 'smart' fluid. Especially, in the area of vibration control, the MR effect is most interesting since it is possible to apply the effect to a hydraulic damper. The MR fluid essentially allows the control of the damping force by replacing mechanical valves commonly used in adjustable dampers. This offers the potential for a superior damper with little concern about reliability, since, if the MR damper ceases to be controllable, it simply reverts to a passive damper.

The semi-active damper employed in seat suspensions of many off and on-highway vehicles is the Lord corporation's RD-1005 − 3 MR-damper. For a head-to-head comparison with the CVNFD suspension, a contemporary suspension with an airspring and MR damper will be used. While, the analytical modeling of the airspring done in section 6.1 holds for this suspension, the MR damper itself needs to be modeled. The following section describes the modeling of the MR damper based on manufacturer's specifications.

6.3.1 MR damper modeling

In the product bulletin (48), the damping characteristic of the MR-damper is plotted as a graph of Typical Force Vs Velocity Profile. This graph has been reproduced here in Fig. 6.4. It can be seen that the damping exhibits an asymmetrical bi-linear force profile with magnitude being a function of the velocity across the damper.

In (45) a continuous skyhook equation was proposed to represent the damping coefficient of the semiactive suspension, which could be adjusted in real time. This has been reproduced here in Eq. 6.12 for reference.

$$C_{sa} = I_s + \frac{e^f - e^{-f}}{I_{on}e^f + I_{off}e^{-f}} \tag{6.12}$$

where, $I_{on} \ll I_{off}, I_s \ll I_{off}, f = KV_1V_{12}$

In the same study, it was shown that using this continuous skyhook function, eliminated dynamic jerks in the damper force. In the present study, the above function is

suitable for implementation, since it is necessary to ascertain the variation of damper force as a function of velocity for use in the simulation model. Hence, the profile shown in Fig. 6.4 has been approximated by a continuously differentiable function obtained by superposing a modified hyperbolic tangent function with a ramp as shown in Eq. 6.14 and Fig. 6.5.

$$F_{dmin} = 100\left[\frac{0.15e^{2f} - e^{-2f}}{e^{2f} + 0.3e^{-2f}}\right] + 5f \tag{6.13}$$

$$F_{dmax} = 1400\left[\frac{1.1e^{2f} - e^{-2f}}{1.4e^{2f} + e^{-2f}}\right] + 18f \tag{6.14}$$

where,

f $= 100(\dot{x_a} - \dot{d})$.

$\dot{x_a}$ = velocity of the seat platform.

$\dot{d}$ = velocity of the base.

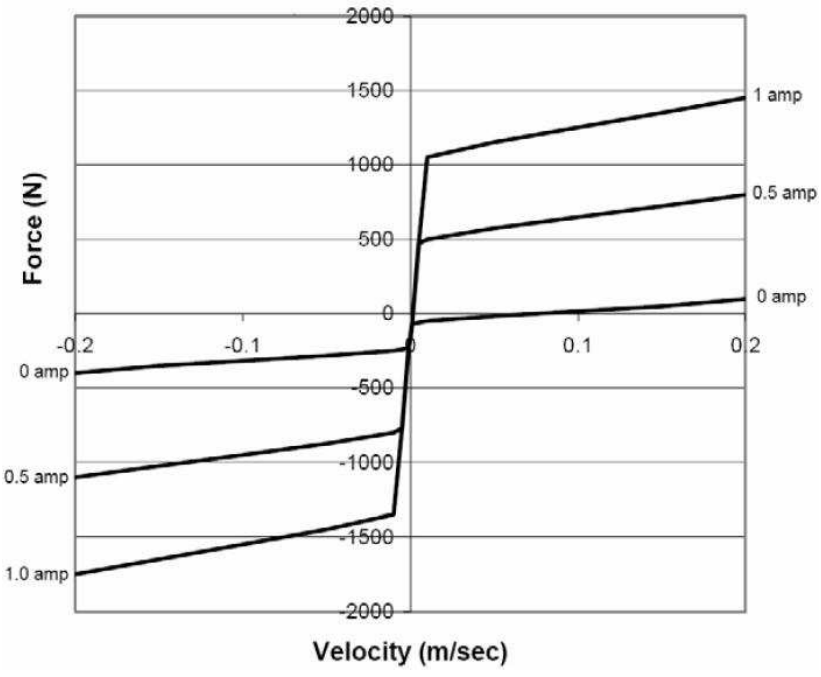

Figure 6.4 Typical Force Vs velocity profile (manufacturer specs.)

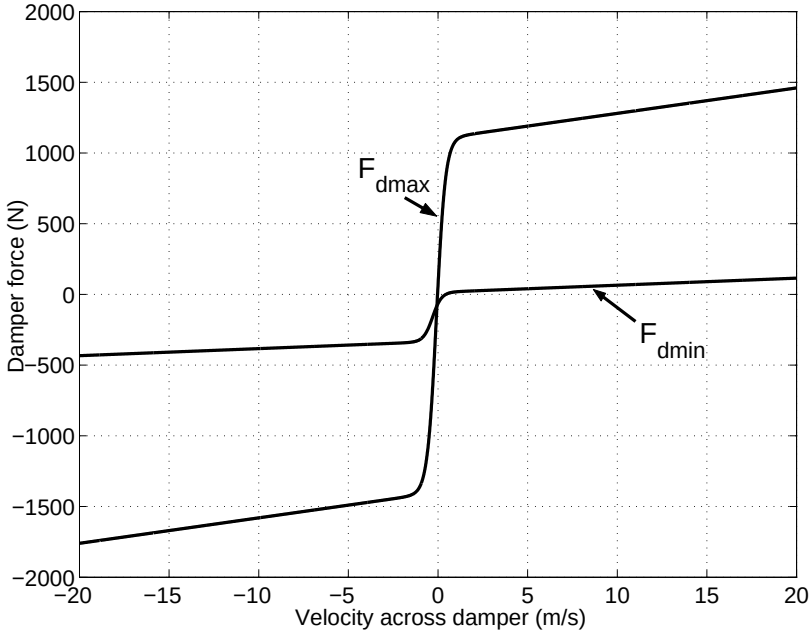

Figure 6.5 Continuous approximation of damper force

In (49), a study on the response time characteristics of the MR damper was conducted. Based on the damper force response to a step input in current, it was shown that the damper behaved like a first order system with a time lag of 1 millisecond. This response characteristic of the damper has also been incorporated into the analytical model.

CHAPTER 7. Skyhook control and its variants

As in the case to fully active suspensions, the true potential of semi-active systems is harnessed by actively commanding the suspension components to produce the desired behavior with the help of an intelligent control system. However, there are significant differences between the control systems designed for fully active and semi-active suspensions. The reasons being,

1. The active component in a fully active system is an actuator that can cause relative motion as opposed to a semi-active component which relies on externally caused relative motion to produce the active effect. Example: A hydraulic actuator can produce motion through actuation, however, an MR damper can cause damping only when there exists a relative motion between the suspended mass and the base.

2. Active control systems rely on adding energy into the system to cancel the effect of disturbance. Semi-active system on the other hand achieve the same objective by dissipating the vibration as quickly and effectively as possible.

3. The actuator power and bandwidth available for active systems far exceeds that of semi-active systems.

In view of the above inherent differences, it can be intuitively inferred that linear control techniques which rely on positive force actuation are not very well suited for control of semi-active suspensions. However, some non-linear

control techniques, shown excellent promise for control of such systems and have been employed here for the controller design.

This chapter focusses on the model-independent Skyhook-control based algorithm, while the next chapter considers the design of a more sophisticated model specific non-linear robust control scheme called the sliding mode control for controller synthesis.

The desired region of the CVNFD system shown in Fig. 5.3 is the region utilized for control. In this region, the CVNFD system behaves as a "constant low natural frequency/ continuously variable damping system." Therefore, in this region, the system can be approximated as a conventional spring-mass-damper unit with the spring stiffness remaining constant and given by Eq. 6.10 and the damping changing continuously as shown in fig. 5.7. The skyhook-controller synthesis for this system is explained in the ensuing sections.

7.1 Ideal skyhook control: background

The material in this section is reproduced from (59) to serve as background for the reader. It will also aid in better understanding of the modifications suggested to the original skyhook control algorithms that are introduced later in the chapter.

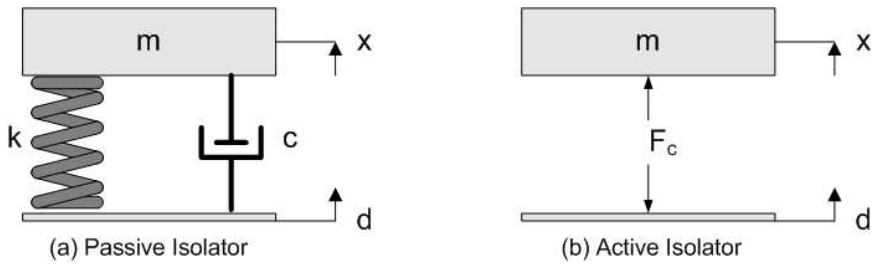

Figure 7.1 Isolation of a mass from ground

In fig. 7.1(a), the familiar passive suspension schematic is shown. The design trade-off between ride comfort and handling was explained in chapter 1. Now, let's consider the schematic shown in Fig. 7.1(b), which is the same isolation problem posed in a more

general context. The control force F_c is studied without regard initially as to whether it can be supplied by a combination of passive elements or whether it must be supplied by some active system such as an hydraulic piston. It is conceptually easy to specify F_c as a function of time for a given $d(t)$ when the criterion for optimizing the suspension has been setout.

But, such an open-loop system is practically much less useful than a closed-loop solution in which F_c is found as a function of the system variables such as $x(t), \dot{x}(t)$ and $d(t), \dot{d}(t)$. In this context, the passive system may be conceived of as a special closed-loop feedback system which generates a force as a weighted sum of forces proportional to relative velocity. That is,

$$F_c = +c(\dot{x} - \dot{d}) + k(x - d) \tag{7.1}$$

for the passive linear system.

Such a force could be supplied by a servo, but, passive elements provide a simpler means of generating the force. On the other hand, however, the active system is not restricted to generating forces of the form of Eq. 7.1.

The question of how F_c should be determined depends on just how the performance criteria for the system are stated. For most practical criteria of performance, it not not known how F_c should be determined, but, valuable clues may be found from linear optimal control theory. When quadratic criteria are used, then the optimal control policy involves feedback of all state variables using a linear weighting co-efficient scheme. In vehicle context, for example, if we assume a roadway generates $d(t)$ histories, which are sample functions of a white noise process, and we minimize $c_1 E(\dot{x}^2) + c_2 E(x-d)^2$ where c_1 and c_2 are given constants and $E(\ )$ stands for "expected value," then

$$F_c = +c(\dot{x}) + k(x - d) \tag{7.2}$$

where, c and k depend on c_1 and c_2, (60) and (61). A similar result is obtained for

a transient response case in which the time integral of the weighted sum of $(\dot{x}^2)$ and $(x-d)^2$ is minimized.

The feedback law in Eq.7.2 can, in fact, be realized by passive elements, as shown in Fig. 7.2.

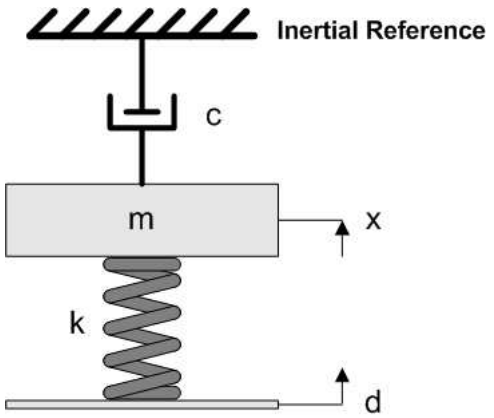

Figure 7.2 Isolation of a mass from ground (skyhook configuration)

In many practical cases, however, it is not possible to connect a damper from the isolated mass to an inertial reference so that the damper force is proportional to the absolute mass velocity. This is obviously the case for vehicle suspensions, and in this case, the inertial reference is assumed to be the sky. Hence the name **"Skyhook damper"** control.

The force law of Eq. 7.2, which arises naturally when Wiener filter theory or a state space optimal control theory is applied to the vibration control problem, can be explained readily using transmissibility plots for the conventional system of Fig. 7.1(a), and the skyhook system of Fig. 7.2 or its active equivalent of Fig. 7.1(b). These plots are shown in Figs.7.3 and 7.4.

The value of spring constant k sets the natural frequency $\omega_n = (k/m)^{\frac{1}{2}}$ for both suspensions. For sinusoidal inputs below this natural frequency, $x \approx d$. Thus, for low frequencies, the spring is primarily responsible for maintaining small relative displacements. Near the resonant frequency, the damper controls the motion of the system.

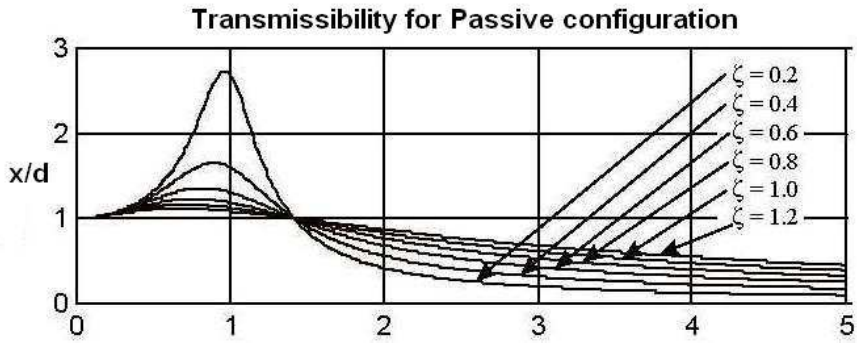

Figure 7.3 Transmissibility for passive system

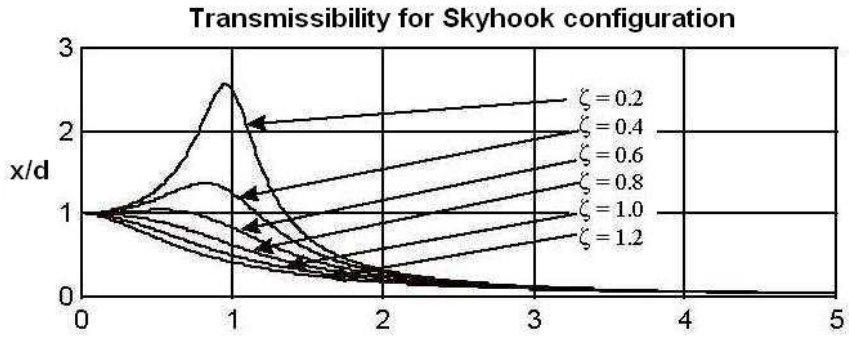

Figure 7.4 Transmissibility for skyhook system

Figures 7.3 and 7.4 shows several plots for various values of damping ratio ζ,

$$\zeta = \frac{c}{2}\left(\frac{m}{k}\right)^{\frac{1}{2}} \tag{7.3}$$

For both suspensions, small values of ζ result in undesirably high values of response for input frequencies near ω_n. For inputs with frequencies greater than the system natural frequency, both suspension systems begin to isolate the mass from the base motions. There is, however a major difference between the two systems as the damping parameter is varied. When ζ is increased in the skyhook configuration, the response near the resonance frequency decreases and also the high frequency response reduces although marginally. But, for the passive system, attennuation in the resonant response is achieved only at the cost of performance degradation at the higher frequencies as can be clearly seen in Fig. 7.3.

The reason for this difference is intuitively evident. The skyhook damper exerts a force tending to reduce the absolute velocity of the mass while the conventional damper exerts a force tending to reduce relative velocity $(\dot{x} - \dot{d})$. For high frequency inputs, the conventional damper acts to stiffen the suspension, when a soft suspension is desired.

An active system programmed to simulate the skyhook damper can therefore achieve a better combination of resonance damping and high frequency isolation than a conventional passive spring damper combination.

7.1.1 Skyhook control law

The linear control law for an active controller of Eq. 7.2 can only be partly realized using an ordinary spring, but the term $c\dot{x}$ cannot be realized by a passive element in the position of the conventional damper in Fig. 7.1(a). The force component $c\dot{x}$ in F_c can be achieved by a servomechanism capable of either supplying or absorbing energy.

Suppose now that a device is installed in place of the conventional damper, and that the device is passive, but, the force across the device is controllable. Such a system will look like Fig. 7.5.

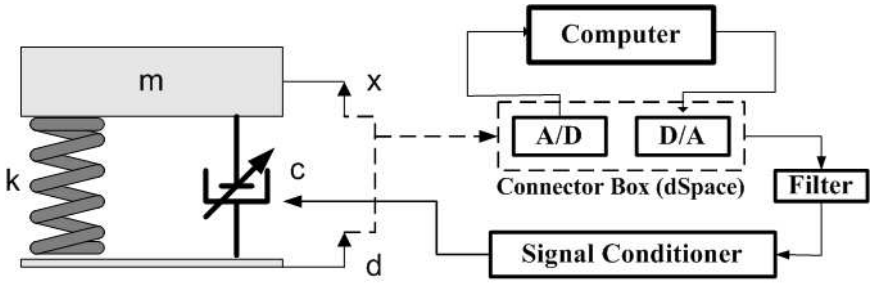

Figure 7.5 Semi-active isolator unit

Let's suppose that the variable damping device is able to generate essentially any force F_d such that the power

$$F_d(\dot{x} - \dot{d}) \geq 0 \tag{7.4}$$

i.e. the power associated with F_d is always dissipative. The desired value of F_d is $c\dot{x}$, but, the semi-active device will only be able to generate this force if the sign of $\dot{x} - \dot{d}$ is proper, since, the device cannot supply power to the system. Thus,

$$F_d \;=\; c\dot{x}, \quad if \quad \dot{x}(\dot{x} - \dot{d}) \;\geq\; 0 \tag{7.5}$$

When $\dot{x}$ and $(\dot{x} - \dot{d})$ are of opposite sign, the device could only supply a force with a sign opposite to the desired force $c\dot{x}$. The best the device can do to approximate the desired force $c\dot{x}$ then is to supply no force at all, which is mathematically given by,

$$F_d \;=\; 0, \quad if \quad \dot{x}(\dot{x} - \dot{d}) \;<\; 0 \tag{7.6}$$

When the relative velocity of the damper is positive, the damper is expanding and when relative velocity is negative, damper compresses. Hence, the logic of the skyhook law uses the following four cases:

1. If the suspension is expanding and the sprung mass is moving up, high damping is required to hold the mass from sling shooting.

2. If the suspension is expanding and the sprung mass is moving down, low damping is required to prevent the mass from being pulled further down.

3. If the suspension is compressing and the sprung mass is moving down, high damping is required to keep the two masses as far apart as possible to prevent suspension bottom-out.

4. If the suspension is compressing and the sprung mass is moving up, low damping is required to prevent transfer of momentum from the base to the sprung mass.

If the expression $\dot{x}(\dot{x} - \dot{d})$ vanishes exactly, two special cases may arise. In the first case, $\dot{x} = 0$, in which case, we anyways desire $F_d = 0$. In the second case, $\dot{x} \neq 0$, but, $(\dot{x} - \dot{d}) = 0$, and in this case, the device can attempt to apply the force $c\dot{x}$. Depending

on the subsequent time history of $\dot{d}$, the quantities $\dot{x}$ and $(\dot{x} - \dot{d})$ either change so that the criteria (7.5)and (7.6) apply in the succeeding instants or the force $c\dot{x}$ may be large enough to lock up the system so that $(\dot{x} - \dot{d} = 0)$ for a finite time. During lock up, $\ddot{x} = \ddot{d}$, and the spring force is $k(x-d)_l$ where $(x-d)_l$ is the spring deflection at lock up. The damper force is then,

$$F_d \;=\; -m\ddot{d} - k(x-d)_l \tag{7.7}$$

Thus we may say that the semi-active device will lock up when,

- $(\dot{x} - \dot{d}) = 0$ and
- the desired force $c\dot{x}$ is larger in magnitude than the expression of Eq. 7.7.

Note: In both computer simulations and hardware realization, true lock up often does not occur. What happens is that the device begins to apply a large force F_d till the relative velocity is driven to zero, at which point, the damper force also becomes zero. As the relative velocity builds, the damper force also builds, and so on. A limit cycle oscillation can exist when $(\dot{x} - \dot{d})$ is nearly zero and the time average value of F_d is near the theoretical lock up force of Eq. 7.7. Eventually, the variables $\dot{x}$ and $\dot{d}$ change enough so that the system breaks out of the lock up condition and remains a finite length of time in the state described by Eqs. 7.5 and 7.6. This limit cycle phenomenon (lock-up) is highly undesirable from a performance standpoint.

In the next section, a modified version of the skyhook law, which prevents the lock-up scenario is presented. **Although, this modified skyhook law is not a new discovery, an appropriate form of this law identified to be suitable for implementation on the pneumatic system to produce variable airspring induced damping is an original contribution of this thesis.**

7.2 Modified skyhook control

In the previous section, skyhook control logic in its original form was introduced. It was shown that even though skyhook control in this form is suitable for implementation in vibration isolation problems, suspension lock up was an inevitable and undesirable characteristic. Even though the suspension may not exactly lock up, sudden jerks in acceleration are felt as the suspension velocity crosses the zero line, i.e., when $(\dot{x}-\dot{d}=0)$. In (45), a modified skyhook control was proposed and implemented on a semi-active suspension comprising of the MR damper. It was shown that the jerks produced by the inherent non-linearities present in the original skyhook law are greatly reduced by making minor modifications to the original skyhook algorithm. This modified version of the Skyhook law is shown below in Eq.7.8.

$$\begin{cases} V_1 V_{12} \geq 0 & F_d = K V_1 |V_{12}| \\ V_1 V_{12} < 0 & F_d = 0 \end{cases} \tag{7.8}$$

where, $V_1 = \dot{x}$ and $V_{12} = (\dot{x} - \dot{d})$.

According to (45), including the relative velocity in the skyhook control formulation eliminates damping force discontinuity and dynamic jerk as can be seen from Figs. 7.6 and 7.7. This modified skyhook control law is used for controlling the MR-damper based semi-active suspension. This skyhook controlled MR-damper based system is used as a benchmark for performance comparison with the pneumatic system , which is also controlled by a variant of skyhook law.

In the case of an oil-based damper (including the MR-damper), damping action is produced by dissipating the Kinetic energy as heat (oil passing through the orifice). However, for the case of the purely pneumatic suspension, the damping effect is produced by the dissipation of pressure energy across the orifice owing to the significant pressure differential that exists across the orifice. This pressure differential is due to the compressibility of air, which is the medium being used. The damping is inherently

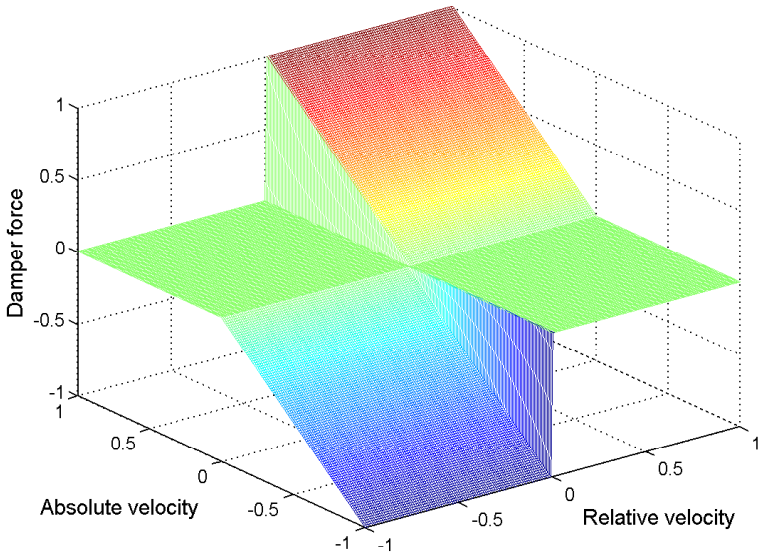

Figure 7.6 Surface plot for original skyhook law

a function of the mass flow rate across the orifice, which in turn is dependent on the relative velocity of the airspring. Due to the dynamics by which pneumatic damping is produced, skyhook logic in the form given by Eqs. 7.5 and 7.6 cannot be implemented.

The new modified skyhook control proposed is,

$$\begin{cases} \text{For} \quad \dot{x_a}(\dot{x_a} - \dot{d}) \geq 0 \quad F_d = 2\varsigma_{\max}\omega_n \times \text{sgn}(\dot{x_a} - \dot{d}) \\ \text{For} \quad \dot{x_a}(\dot{x_a} - \dot{d}) < 0 \quad F_d = 2\varsigma_{\min}\omega_n \times \text{sgn}(\dot{x_a} - \dot{d}) \end{cases} \tag{7.9}$$

Although, the mathematical expression projets a non-linear characteristic to the switching function, the damping ratio ζ is actually a function of the relative velocity across the suspension. Hence, the control law given by Eq. 7.9 is similar to that of Eq. 7.8 and provides a smooth transition of damping from maximum to minimum. This modified skyhook control scheme is utilized for closed loop control of the proposed pneumatic suspension system and its performance is compared with that obtained for the MR-damper based system. The test protocol followed and the results obtained are presented next.

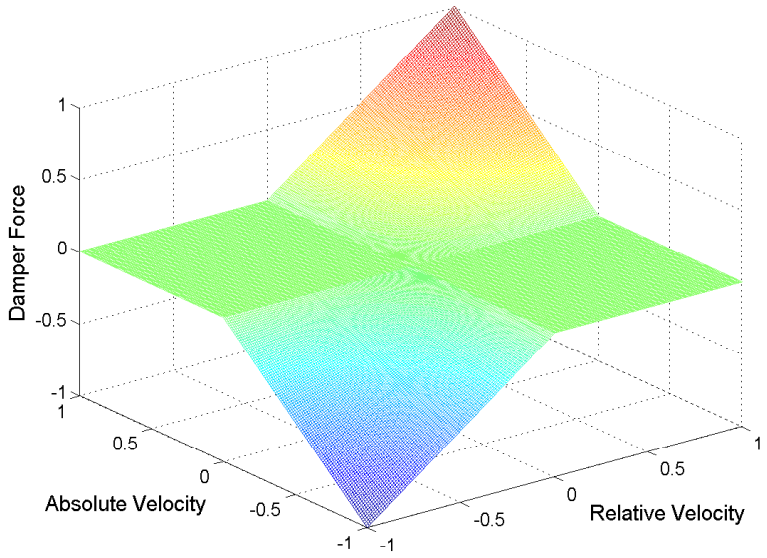

Figure 7.7 Surface plot for modified skyhook law

7.3 Test results (modified skyhook control)

Testing protocol comprise of simulation study on the computational models as well as implementation of the skyhook law on the experimental apparatus. However, experimental testing was carried out only for the case of the purely pneumatic suspension using the test setup shown in Fig. 3.5, due to the unavailability of apparatus for the MR-damper based system.

To simulate base excitation that reflects the vibration environment in typical seat/cab suspensions, an arbitrary profile obtained by randomly superposing three tonal frequencies at $1.5, 2$ and 3 Hz respectively was generated in Matlab. This test-profile was used for all the cases (computation and experiment). The different cases considered are presented below with detailed descriptions.

1. For the case of the purely pneumatic suspension (Eqs. 4.1 and 4.14), the closed loop system with skyhook control (Eq. 7.9) was simulated in Matlab. To ascertain the degree of vibration isolation acheived, acceleration transmissibility between the

base and the sprung mass was obtained for the arbitrary profile base excitation input. Figure 7.8 shows the result.

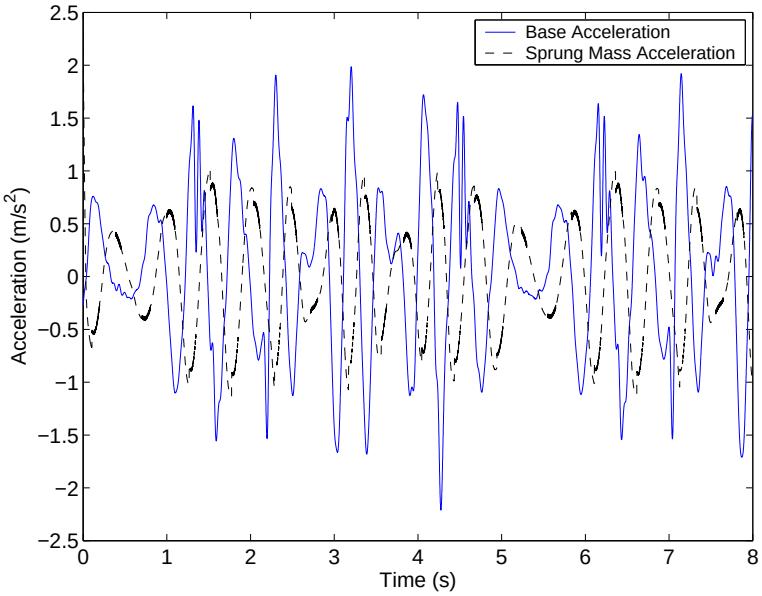

Figure 7.8 Acceleration transmissibility (simulation result)

2. The same Skyhook law (Eq. 7.9) was then implemented on the hardware. The velocity signals required for the implementation of the control logic were directly obtained from the velocity sensors shown in Fig. 3.5. The acceleration signals were processed using high sensitivity DC accelerometers (Fig. 3.5). Figure 7.9 shows the acceleration transmissibility obtained.

3. A single degree-of-freedom simulation model using the spring stiffness derived in Eq.6.3 and the damping force derived empirically in Eq.6.14 was built in Simulink. This model which used the conventional MR-damper as the semi-active device was used as a benchmark for comparison with the pneumatic system. The acceleration transmissibility obtained for this benchmark system controlled by skyhook control (Eq. 7.8) is shown in Fig. 7.10.

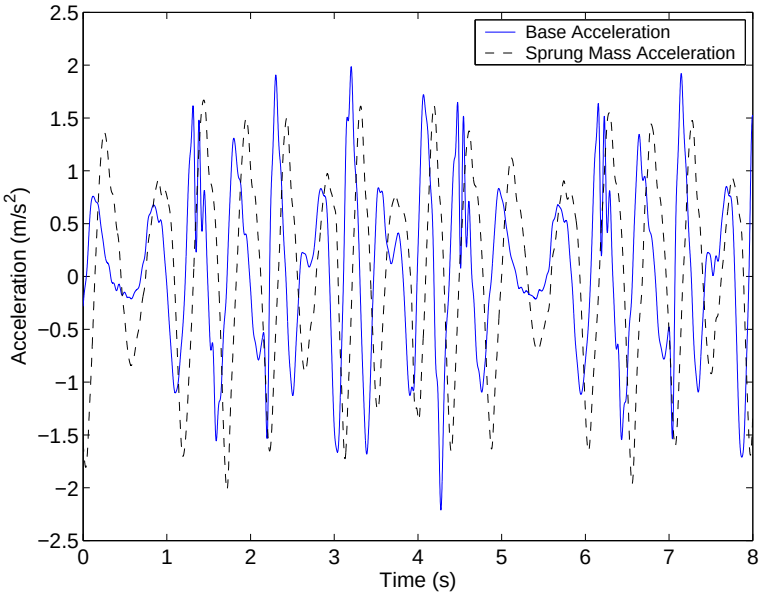

Figure 7.9 Acceleration transmissibility (experiment result)

4. To get a better idea of the performance achieved by the pneumatic suspension in comparison to the contemporary MR-damper based system, suspended mass acceleration for both the cases have been plotted in Fig. 7.11.

7.3.1 Conclusions

A modified Skyhook control was implemented on the pneumatic suspension system. Suspension parameters for both the pneumatic and the MR-damper based systems were derived from first-principles and system identification. Based on the type of suspension, the appropriate form of Skyhook control was implemented. From Figs. 7.8 - 7.11, it can be inferred that the skyhook controlled pneumatic suspension utilizing only airspring induced damping is able to provide a degree of vibration isolation comparable with the semi-active MR-damper based system, which also employed the skyhook scheme. In the following chapter, a more advanced nonlinear control scheme called the sliding mode control, which also utilizes the advantages of the skyhook law, is presented and its performance is compared with that achieved by the modified skyhook law (Eq. 7.9).

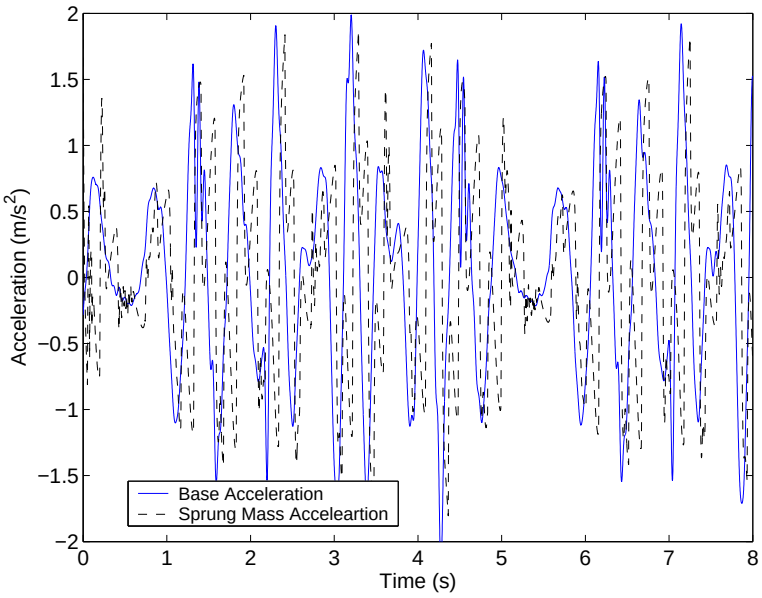

Figure 7.10 Acceleration transmissibility (MR suspension)

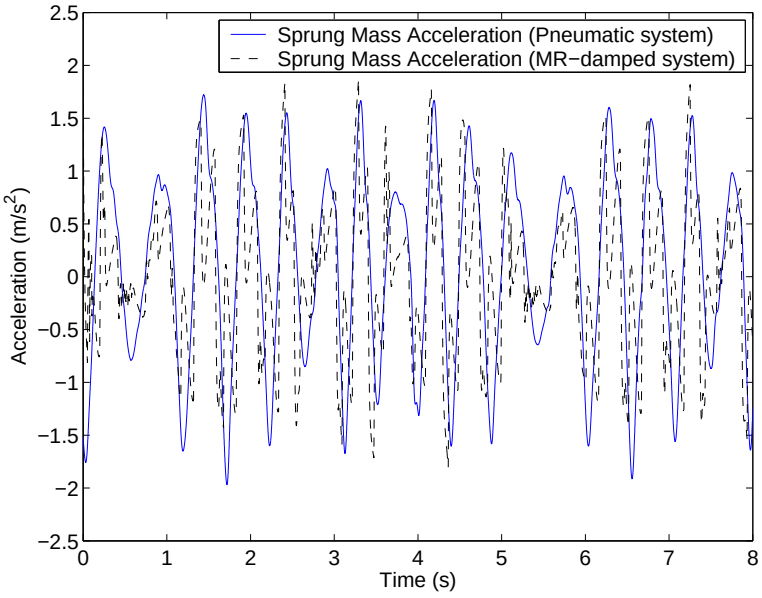

Figure 7.11 Comparison of suspended mass acceleration

CHAPTER 8. Sliding mode control

In this chapter, control of the proposed pneumatic system using Sliding Mode Control is presented. The pneumatic isolator is modeled as a single degree of freedom, second order system with damping and natural frequency obtained experimentally and analytically as explained in Chapter 6. The basic concepts of Sliding Mode Control used for the design and synthesis of the controller are provided in *Appendix*-A. This information will serve both as a background material for the reader and help in understanding the controller synthesis procedure followed for the design of the sliding mode controller.

8.1 Continuous sliding mode control of the pneumatic system

The sliding mode methodology explained in *Appendix*-A is utilized to synthesize a model specific robust controller for the proposed pneumatic system. From literature, it can be inferred that skyhook control is one of the most suitable control schemes, especially for semi-active suspension applications involving controllable dampers. In the previous chapter, the suitability of the skyhook law in regulating airspring induced damping was demonstrated. Although, the modified skyhook law performed satisfactorily, some of its limitations were:

- The control algorithm could not take advantage of system dynamics to improve performance (Due to the model independent controller algorithm).
- High actuator bandwidth was required due to the discontinuous switching of the control input.

- Life-time expectancy of the actuator becomes a concern when implementing such a switching law.

- Most significantly, the control algorithm is not always successful, because, there is no feedback to compensate for damper force errors such as those caused by time delays.

The proposed continuous sliding mode controller is able to overcome all these limitations of the original skyhook scheme by formulating the control as an asymptotic model matching problem, in which, the objective is to force the plant to behave like a suitably chosen reference model in response to an exogenous input. In the proposed sliding mode scheme, this objective of model matching is achieved by forcing the tracking error dynamics between the pneumatic system dynamics and the dynamics of the skyhook model (Fig. 7.2) in the sliding mode. The idea here is that, since, the skyhook model dynamics closely resembles that of the pneumatic system, the pneumatic system can be made to follow the reference model and the error dynamics between the two can be forced to converge to zero asymptotically.

The ensuing sections present the synthesis procedure for deriving the controller parameters. In the section that follows later, the synthesized sliding mode controller is implemented both on a simulation model as well as on the actual hardware and an exhaustive analysis of its performance is conducted. As a first step in the controller design process, the development of state-space representation for the linearized pneumatic system is accomplished, which is presented below.

8.1.1 Linearized pneumatic system model

Figure 8.1 shows the actual pneumatic system schematic comprising of the airspring, orifice and accumulator and its equivalent spring-mass-damper representation. The spring-accumulator combination has been replaced by a spring with stiffness K_{as} as

derived in section 6.1.1 and the orifice mechanism is replaced by a variable force damper whose damping characteristics are as shown in Fig. 6.3.

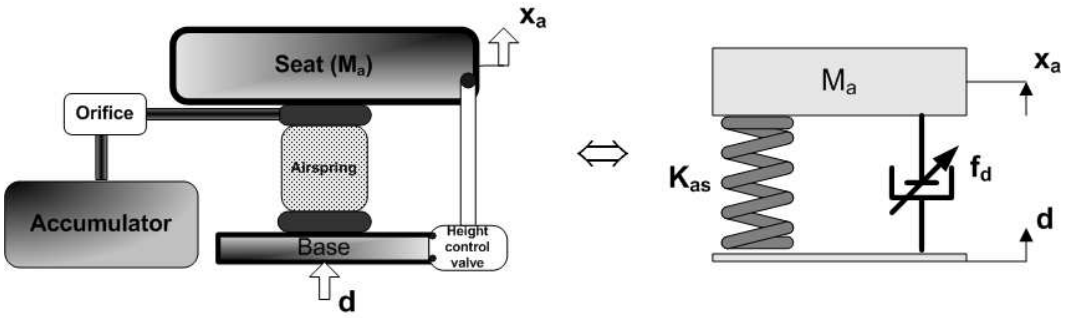

Figure 8.1 Linearized pneumatic system model

The equation of motion for the suspended mass is given by,

$$M_a\ddot{x}_a + K_{as}(x_a - d) + f_d = 0 \tag{8.1}$$

where, $f_d = F(\dot{x}_a - \dot{d})$.

Suppose, the state vectors are chosen as $x = [x_1 \quad x_2]^T$, where, x_1 is the suspended mass displacement, and x_2 is the suspended mass velocity, Eq. 8.1 can be represented in state variable form as,

$$\begin{aligned} \dot{x}_1 &= x_2 \\ \dot{x}_2 &= -\frac{K_{as}}{M_a}x_1 - \frac{1}{M_a}f_d + \frac{K_{as}}{M_a}d \end{aligned} \tag{8.2}$$

Thus the state-space representation becomes,

$$\dot{x} = Ax + B_u f_d + B_d d \tag{8.3}$$

$$\text{where, } A = \begin{bmatrix} 0 & 1 \\ -\frac{K_{as}}{M_a} & 0 \end{bmatrix} \quad B_u = \begin{bmatrix} 0 \\ -\frac{1}{M_a} \end{bmatrix} \quad B_d = \begin{bmatrix} 0 \\ \frac{K_{as}}{M_a} \end{bmatrix}$$

From the above state-space model, although the A matrix can be observed to have poles on the $j\omega$ axis, the system (A, B_u) is fully controllable and thus, damping could be added through the B_u matrix to make the system stable, i.e, through addition of control.

8.1.2 Reference (skyhook) model

Now, let's consider the single degree of freedom skyhook system, which is used as a reference model. A schematic of this model is as shown in Fig. 8.2. As can be seen from the figure, the parameters of the skyhook system are chosen to be the same as those of the pneumatic system. This is to ensure that the reference model closely represents the actual system dynamics and that unrealistic performance demands are not placed on the semi-active device.

For the system represented in Fig. 8.2, the equation of motion can be written as,

$$M_a\ddot{x}_{sky} + K_{as}(x_{sky} - d) + C_s\dot{x}_{sky} = 0 \tag{8.4}$$

where,

$$C_{sky} = \begin{cases} 2\zeta_{\max}\omega_n \times M_a & \text{for} \quad \dot{x}_{sky}(\dot{x}_{sky} - d) \geq 0 \\ 2\zeta_{\min}\omega_n \times M_a & \text{for} \quad \dot{x}_{sky}(\dot{x}_{sky} - d) < 0 \end{cases} \tag{8.5}$$

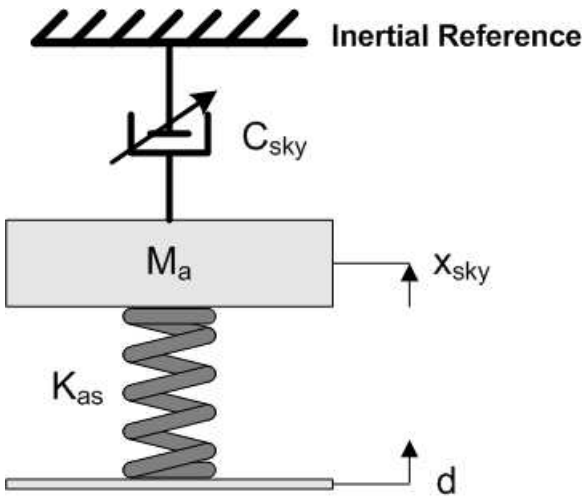

Figure 8.2 Reference (skyhook) system model

Now, defining the state vector for the reference model as $x_r = [x_{r1} \quad x_{r2}]$, where, $x_{r1} = x_{sky}$, the skyhook suspended mass displacement, and $x_{r2} = \dot{x}_{sky}$, the skyhook

suspended mass velocity, Eq. 8.4 can be written in state variable form as,

$$\begin{aligned} \dot{x}_{r1} &= x_{r2} \\ \dot{x}_{r2} &= -\frac{K_{as}}{M_a}x_{r1} - \frac{C_{sky}}{M_a}x_{r2} + \frac{K_{as}}{M_a}d \end{aligned} \tag{8.6}$$

Thus, the resulting state-space representation of the reference model becomes,

$$\begin{aligned} \dot{x}_r &= A_r x_r + B_d d \\ \text{where, } A_r &= \begin{bmatrix} 0 & 1 \\ -\frac{K_{as}}{M_a} & -\frac{C_{sky}}{M_a} \end{bmatrix} B_d = \begin{bmatrix} 0 \\ \frac{K_{as}}{M_a} \end{bmatrix} \end{aligned} \tag{8.7}$$

8.1.3 Tracking error dynamics

As mentioned before, the logic behind the design methodology of the sliding mode controller is to force the tracking error dynamics between the pneumatic system and the skyhook system in the sliding mode. To accomplish this objective, appropriate error dynamics has to be defined. As a first step in ascertaining the error dynamics, let's define the tracking error vector with integral action in the state variables form as,

$$\mathbf{e} = [e_1 \quad e_2 \quad e_3]^T = \left[(x_1 - x_{r1}) \quad (x_2 - x_{r2}) \quad \int (x_1 - x_{r1})\right]^T \tag{8.8}$$

where, $(x_1 - x_{r1})$ is the displacement error, $(x_2 - x_{r2})$ is the velocity error, and $\int(x_1 - x_{r1})$ is the integral of the displacement error.

The error dynamics can then be obtained by differentiating Eq. 8.8 with respect to time. Hence,

$$\dot{\mathbf{e}} = [\dot{e}_1 \quad \dot{e}_2 \quad \dot{e}_3]^T = [(\dot{x}_1 - \dot{x}_{r1}) \quad (\dot{x}_2 - \dot{x}_{r2}) \quad (x_1 - x_{r1})]^T \tag{8.9}$$

From Eqs. 8.2, 8.6 and 8.9, we can derive,

$$\dot{e}_1 = \dot{x}_1 - \dot{x}_{r1} = x_2 - x_{r2} = e_2$$

$$\dot{e}_2 = \dot{x}_2 - \dot{x}_{r2} = \frac{-K_{as}}{M_a}(x_1 - x_{r1}) - \frac{C_{sky}}{M_a}(x_2 - x_{r2}) + \frac{C_{sky}}{M_a}x_2 - \frac{1}{M_a}f_d$$

$$\Rightarrow \dot{e}_2 = \frac{-K_{as}}{M_a}e_1 - \frac{C_{sky}}{M_a}e_2 + \frac{C_{sky}}{M_a}x_2 + \frac{1}{M_a}f_d$$

$$\dot{e}_3 = x_1 - x_{r1} = e_1 \tag{8.10}$$

Now, using equation set 8.10, the tracking error dynamics can be written in state-space form as,

$$\dot{\mathbf{e}} = A_e\mathbf{e} + Gx + B_e f_d \tag{8.11}$$

$$\text{where, } A_e = \begin{bmatrix} 0 & 1 & 0 \\ -\frac{K_{as}}{M_a} & -\frac{C_{sky}}{M_a} & 0 \\ 1 & 0 & 0 \end{bmatrix} G = \begin{bmatrix} 0 & 0 \\ 0 & \frac{C_{sky}}{M_a} \\ 0 & 0 \end{bmatrix} B_e = \begin{bmatrix} 0 \\ -\frac{1}{M_a} \\ 0 \end{bmatrix}$$

8.1.4 Sliding surface for integral control

To guarantee the asymptotic stability of the error dynamics, sliding mode control is very suitable. Moreover, tracking performance can also be achieved by suitably choosing the error dynamics. As explained in section A.0.3, to produce an integral action on the displacement error (for tracking) between the reference model and the pneumatic system, $\left(\int_0^t e(r)dr\right)$ can be included as a variable of interest and an appropriate sliding surface as shown in Eq. A.22 can be chosen. Since, the error dynamics for the pneumatic system is third order relative to the error variable, the equation for sliding surface is exactly that defined in Eq. A.22, and is as shown below.

$$s = \left(\frac{d}{dt} + \lambda\right)^2 \left(\int_0^t edr\right) = \dot{e} + 2\lambda e + \lambda^2 \int_0^t edr \tag{8.12}$$

8.1.5 Synthesis of control input

As shown in Fig. A.4, the objective of the sliding mode controller is to force the system dynamics to approach the sliding surface. Once on the surface, the error dynamics asymptotically converges to zero.

Suppose the error dynamics is in the sliding mode, then

$$s = \dot{s} = 0 \tag{8.13}$$

From Eq. 8.12, by differentiating we get,

$$\begin{aligned} \dot{s} &= \ddot{e} + 2\lambda\dot{e} + \lambda^2 e = 0 \\ \Rightarrow \dot{s} &= \dot{e}_2 + 2\lambda e_2 + \lambda^2 e_1 = 0 \end{aligned} \tag{8.14}$$

Now, substituting for $\dot{e}_2$ from Eq. 8.10, we get,

$$\frac{-K_{as}}{M_a}e_1 - \frac{C_{sky}}{M_a}e_2 + \frac{C_{sky}}{M_a}x_2 - \frac{1}{M_a}f_d + 2\lambda e_2 + \lambda^2 e_1 = 0 \tag{8.15}$$

Re-arranging Eq. 8.15, the equivalent sliding mode control input $f_{d(eq)}$ can be obtained and is as shown below in Eq. 8.16.

$$f_{d(eq)} = \left(\lambda^2 M_a - K_{as}\right) e_1 + \left(2\lambda M_a - C_{sky}\right) e_2 + C_{sky} x_2 \tag{8.16}$$

The effective control force $f_{d(eq)}$ synthesized above in Eq. 8.16 was obtained by setting $\dot{s} = 0$. However, to ensure that the sliding mode controller satisfies the sliding condition given by Eq. A.13 despite uncertainty in the pneumatic system dynamics, a term discontinuous across the surface $s = 0$ is added to the damper force $f_{d(eq)}$. The sliding mode control force is obtained by adding this discontinuous term (called the relay term $Ksgn(s)$) and is as shown in Eq. 8.17.

$$f_{d(smc)} = f_{d(eq)} + Ksgn(s) \tag{8.17}$$

where, $K = K(x_a, \dot{x}_a)$ is chosen large enough so that the sliding condition (Eq. A.13) is guaranteed under all quantified system perturbations. The synthesis of the relay term

$Ksgn(s)$ requires the use of Lyapunov stability theory and its derivation is presented in the following section.

8.1.6 Lyapunov stability analysis of pneumatic system

Lyapunov's direct method, explained in section A.1 is used for the synthesis of the relay term $Ksgn(s)$ in such a way that the resulting controller will make the closed loop system (origin) globally asymptotically stable.

In section, A.1, the concepts on Lyapunov functions and their use in the stability theorems were explained. The two basic steps involved were first to choose a positive definite function, and then second to determine its derivative along the path of the non-linear system under consideration. The same procedure is applied for the case of the pneumatic system.

For the purpose of continuity, re-writing the sliding mode condition given by Eq. A.13, we get,

$$\frac{1}{2}\frac{d}{dt}s^2 \leq -\eta\,|s| \tag{8.18}$$

To prove the existence of the sliding mode condition (Eq. 8.18), consider a Lyapunov function candidate,

$$V(s) = \frac{s^2}{2} \tag{8.19}$$

Differentiating Eq. A.40 and applying the sliding mode condition, we get the relation,

$$\frac{d}{dt}V(s) = \frac{1}{2}\frac{d}{dt}s^2 = s\dot{s} \leq -\eta\,|s| \tag{8.20}$$

where, η is a strictly positive constant.

Now, by simple algebraic manipulation, Eq. 8.12 can be re-written in matrix form as shown below.

$$s \;=\; \left(\frac{d}{dt}+\lambda\right)^2\left(\int_0^t e dr\right) = \dot{e} + 2\lambda e + \lambda^2\int_0^t e dr$$

$$
\begin{aligned}
s &= \begin{bmatrix} 1 & 2\lambda & \lambda^2 \end{bmatrix} \begin{bmatrix} \dot{e} \\ e \\ \int e \end{bmatrix} = \begin{bmatrix} 1 & 2\lambda & \lambda^2 \end{bmatrix} \begin{bmatrix} e_2 \\ e_1 \\ \int e_1 \end{bmatrix} \\
&= \begin{bmatrix} 2\lambda & 1 & \lambda^2 \end{bmatrix} \begin{bmatrix} e_1 \\ e_2 \\ \int e_1 \end{bmatrix} \\
\Rightarrow s &= \Lambda \mathbf{e} \qquad (8.21)
\end{aligned}
$$

where, $\Lambda = \begin{bmatrix} 2\lambda & 1 & \lambda^2 \end{bmatrix}$

Substituting from Eqs. 8.11, 8.16, 8.17 and 8.21 into Eq. 8.20, we get

$$
\begin{aligned}
\dot{s}\, s &= \Lambda\, \dot{e}\, s = \Lambda \left(A_e e + Gx + B_e f_{d(smc)} \right) s \leq -\eta\, |s| \\
\Rightarrow \dot{s}\, s &= \Lambda \left(A_e e + Gx + B_e \left(f_{d(eq)} + K \mathrm{sgn}(s) \right) \right) s \leq -\eta\, |s| \\
\Rightarrow \dot{s}\, s &= \Lambda \left(A_e e + Gx + B_e f_{d(eq)} \right) s + \Lambda B_e K \mathrm{sgn}(s) s \leq -\eta\, |s| \qquad (8.22)
\end{aligned}
$$

It can be noticed from Eq. 8.22 that the first term is identically equal to zero, since, the equivalent control force $f_{d(eq)}$ is produced when the dynamics is in sliding mode. Also, from Eq. 8.22, the term $K\mathrm{sgn}(s) \times s$ is equivalent to $K|s|$. Hence, Eq. 8.22 becomes,

$$
\begin{aligned}
\Lambda B_e K\, |s| &\leq -\eta\, |s| \\
\Rightarrow \begin{bmatrix} 2\lambda & 1 & \lambda^2 \end{bmatrix} \begin{bmatrix} 0 \\ -\frac{1}{M_a} \\ 0 \end{bmatrix} K &\leq -\eta \\
\Rightarrow K &\geq \eta M_a \qquad (8.23)
\end{aligned}
$$

Substituting the result obtained in Eq. 8.23 into Eq. 8.17, the expression for the damper force can be obtained as,

$$f_{d(smc)} \;=\; f_{d(eq)} + (\eta M_a) sgn(s) \tag{8.24}$$

Similar to the case of skyhook control, the damper force $f_{d(smc)}$ produced by the sliding mode controller is constrained by the skyhook logic (Eqs. 7.5 and 7.6). This is to ensure that the damper force always acts such that the suspended mass vibration is dissipated and not exacerbated. The difference between the sliding mode controller and the original skyhook controller is that the desired value of the damper force is now $f_{d(smc)}$ instead of $c\dot{x}$. Again, noting that the semi-active device will only generate this force if the sign of $\dot{x_a} - \dot{d}$ is proper, since, the device cannot supply power to the system, the sliding mode control has to be modified into the form,

$$f_{d(smc)} \;=\; f_{d(eq)} + (\eta M_a) sgn(s), \quad for \;\; (f_{d(eq)} + (\eta M_a) sgn(s))(\dot{x_a} - \dot{d}) \;\geq\; 0 \tag{8.25}$$

When $(f_{d(eq)} + (\eta M_a) sgn(s))$ and $(x_a - d)$ are of opposite sign, the best the device can do to approximate the desired damper force is to supply no force at all, i.e.,

$$f_{d(smc)} \;=\; 0, \quad for \;\; (f_{d(eq)} + (\eta M_a) sgn(s))(\dot{x_a} - \dot{d}) \;\leq\; 0 \tag{8.26}$$

Equations 8.25 and 8.26 together make-up the sliding mode control law for the pneumatic system shown in Fig. 8.1.

However, as explained in section A.0.4, sliding control law in the above form has one significant drawback. In order to account for the presence of modeling imprecision and disturbances, the control law is made discontinuous across $S(t)$ (i.e. due the relay term). This causes an undesirable characteristic in the form of chattering. The extreme control activity as a result of chattering can have a detrimental effect on the life expectancy of the hardware. Hence, the chattering effect has to be minimized if not eliminated. This can be accomplished by using a continuous approximation term $(sat(s)/\Phi)$ in place of the discontinuous switching term (sgn) in Eqs. 8.25 and 8.26 (as shown in Eq. A.33).

This leads to a continuous approximation of the sliding mode control law (Eqs. 8.25 and 8.26).

$$f_d = \begin{cases} f_{d(smc)} + (\eta M_a)\, sat\,(s/\Phi) & for \;\; (f_{d(smc)} + (\eta M_a)\, sat\,(s/\Phi))\left(\dot{x}_a - \dot{d}\right) \geq 0 \\ 0 & for \;\; (f_{d(smc)} + (\eta M_a)\, sat\,(s/\Phi))\left(\dot{x}_a - \dot{d}\right) \geq 0 \end{cases} \tag{8.27}$$

From this control law, it can be noticed that when $f_d = (f_{d(smc)} + (\eta M_a)\, sat\,(s/\Phi))$, the sliding mode condition was shown to be satisfied in Eq. 8.23. However, when $f_d = 0$, the same does not hold. In this scenario we have,

$$\dot{s} = \left(\lambda^2 - \frac{K_{as}}{M_a}\right) e_1 + 2\lambda e_2 + \frac{C_{sky}}{M_a} x_2 \tag{8.28}$$

Hence, the Lyapunov stability condition $\dot{s} < 0$ cannot be guaranteed for the case $f_d = 0$. However, $f_d = 0$, the pneumatic system becomes a conventional passive system, and the error dynamics is assumed to be bounded, since, following the skyhook based reference model with similar parametric values is a realistic demand. Moreover, when the control is re-applied, the error which existed during the phase when $f_d = 0$ gets reduced. It will be shown in simulation and experiments that this assumption on stability of the system is indeed justified under all conditions of the damper force described by Eq. 8.27.

8.2 Simulation study and experimental corroboration

In chapter 7, the performance of the skyhook controller implemented on the pneumatic system was compared with a similar skyhook scheme applied to a MR-damper based conventional semi-active system. It was inferred based on the plots that the performance of the skyhook suspension closely rivals that of the MR-damper based unit. In this section, a comparison is made between the performance obtained by the skyhook control and the sliding mode control employed for closed-loop control of the pneumatic system. Simulation study was carried out to optimize the design parameters of the sliding mode controller: Boundary layer thickness "Φ", Control switching term "η" and

Error dynamics weighting matrix "Λ" were tweaked to achieve the main objective of reducing the acceleration transmissibility. The pneumatic system was simulated in the Matlab/Simulink environment (Fig. B.2), where, the sub-system "skyhook model" is as shown in Fig. B.1. Simulations were carried out for the same random base excitation input used in chapter 7. Although, acceleration is considered as the most important performance measure due to its direct co-relation with passenger comfort, two other measures were used for performance appraisal.

1. Displacement transmissibility to ascertain resonance behavior.

2. Magnitude of damper force to ascertain the control effort.

To corroborate the findings from the computational study explained in the previous section, experimental testing protocol with similar parametric constraints was undertaken. In chapter 7, performance of the skyhook controller implemented on the pneumatic system was compared with a similar skyhook scheme applied to a MR-damper based conventional semi-active system. From the plots, it was inferred that the performance of the skyhook suspension closely rivaled that of the MR-damper based unit. In the experimental part of this section, a comparison is made between the performance of the skyhook controller and the sliding mode controller, both implemented on the pneumatic system. Comparisons between the simulation study of the sliding mode controller and the experimentally observed behavior were also made at appropriate places. The simulink block diagram constructed to interface the data acquisition board and the hardware is included in the *Appendix*-B for the reader's reference (Fig. B.5). Simulation studies, corresponding experimental tests and relevant analysis performed for the different cases under consideration are presented in the ensuing paragraphs.

Test-case 1(skyhook control): The simulation study and hardware implementation of the skyhook controller was conducted in chapter 7. This test-case also corresponds

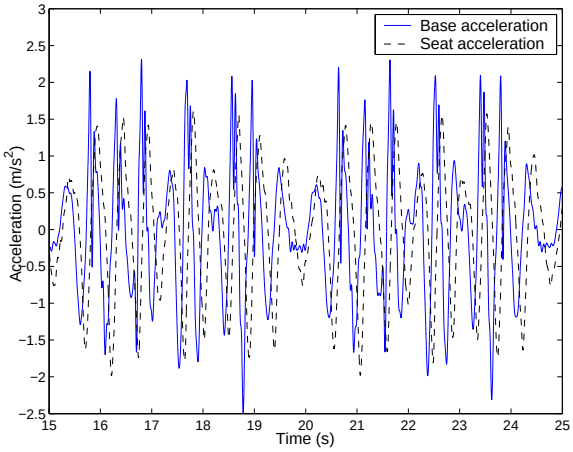

Figure 8.3 Acceleration transmissibility (experiment "skyhook control")

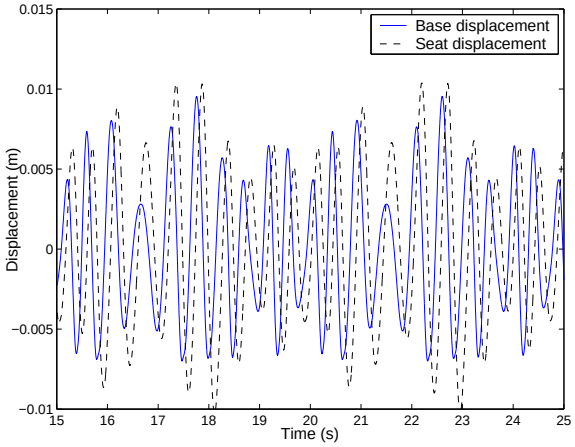

Figure 8.4 Displacement transmissibility (experiment "skyhook control")

to the skyhook controller (defined by Eq. 7.9) implemented on the pneumatic system (Fig. 8.1) and is used as a benchmark for making comparisons with the performance of the sliding mode controller. The simulink block diagram constructed for skyhook controller implementation and data acquisition is included in *Appendix*-B. The random profile obtained by superposition of sinusoids (see chapter 7) is used for base excitation in all the cases including this case. Figs. 8.3, 8.4 and 8.5 show the acceleration transmissibility, displacement transmissibility and damper force respectively for the closed loop system. Similar to Fig. 7.9, it can be noticed from the plot of acceleration transmissibility (Fig. 8.3) that the skyhook controller performs well in arresting the acceleration on the upstroke, but, its performance deteriorates during the suspension downstroke. Since, skyhook control is a model independent control, this performance achieved cannot be fine-tuned for improvement.

Unlike acceleration transmissibility, the importance of displacement transmissibility arises only when the magnitude of seat displacement becomes significantly larger than that of the base, since, it can then cause handling problems. However, a displacement transmissibility of much greater than 1 (Fig. 8.4) at many instances clearly shows that

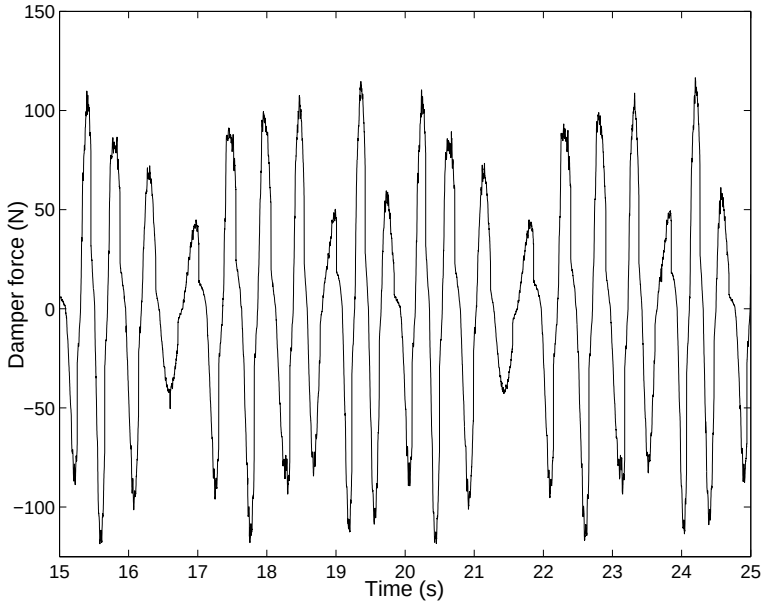

Figure 8.5 Damper force (skyhook control)

the damper force in not effective in arresting sprung mass motion. One reason for this could be that delays always exist in actuator dynamics (in this case, the solenoid valve) and, since, the skyhook algorithm does not obtain feedback of the damper force, these time delays are uncorrected and lead to the degradation in performance. Moreover, the model independent nature of the skyhook controller cannot take into account the uncertainties that are inherent in the pneumatic system.

Test-case 2: This set corresponds to the best configuration of the sliding mode controller design parameters. For this test, the controller parameters were initially chosen according to the relationships obtained in the controller synthesis procedure and then fine-tuned based on observations of the performance measures. The resulting controller parameters were: The boundary layer thickness $\Phi = 0.01$; The switching term constant $\eta = 1 \;\Rightarrow\; K = \eta * M_a = 90$; weighting for displacement error $\lambda_1 = 4$; and weighting for the integral of displacement error $\lambda_3 = 16$.

From Fig. 8.6, it can be noticed that the sliding mode controller provides an excellent

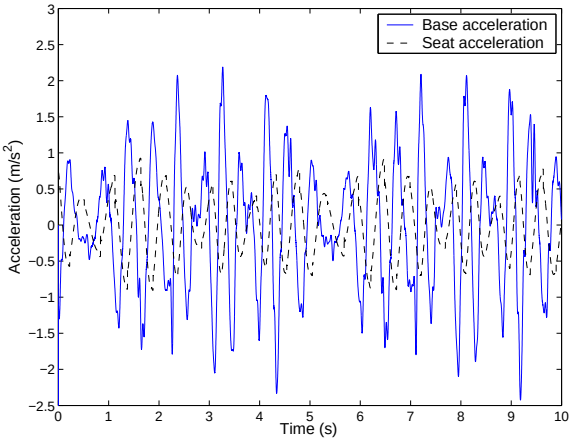

Figure 8.6 Acceleration transmissibility (simulation case 2)

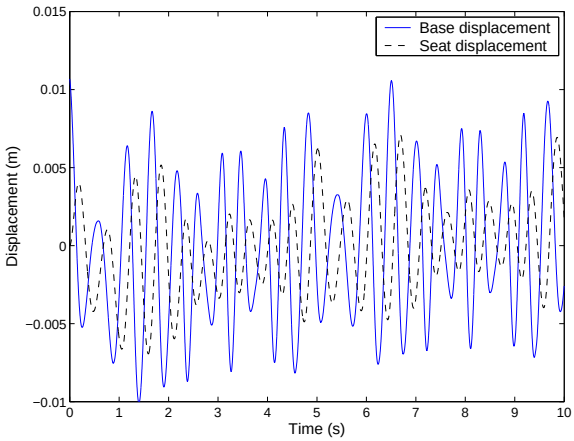

Figure 8.7 Displacement transmissibility (simulation case 2)

attenuation of acceleration transmissibility (more than a two-fold reduction). Another interesting observation that could be made by comparing Fig. 8.6 with Fig. 7.8 is that the performance of the sliding mode controlled pneumatic system is very similar to the skyhook controlled pneumatic system. This is due to the fact that the sliding mode controller forces the pneumatic system dynamics to behave like a skyhook controlled system, since, the reference model chosen is exactly the skyhook model. This observation can also be inferred by analyzing the sliding surface dynamics (Fig. 8.9), which, is an indicator of the error between the states of the pneumatic system and that of the reference skyhook model. The bounded characteristic of the sliding surface dynamics also justifies the claim made earlier (section 8.1.6) regarding system stability. Even though the damper force is intermittently available due to the nature of the sliding mode control law (Eq. 8.27), the pneumatic system dynamics does not diverge from that of the reference model quickly enough to cause instability. This allows the controller to reduce the built-up error using finite control effort (Eq. 8.8) when the damper gets re-activated by the sliding mode control law.

Fig. 8.7 shows the performance of the sliding mode controller from a displacement

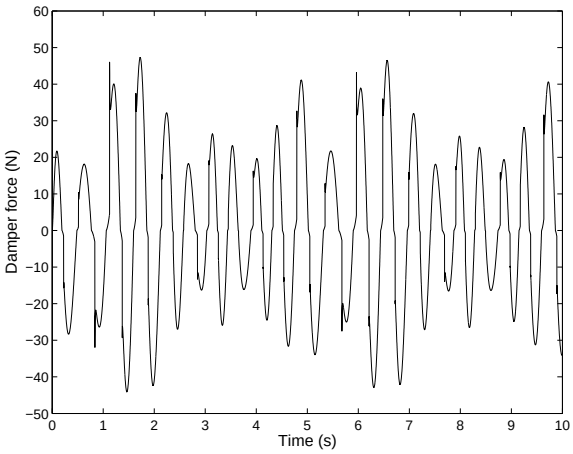

Figure 8.8 Damper force (simulation case 2)

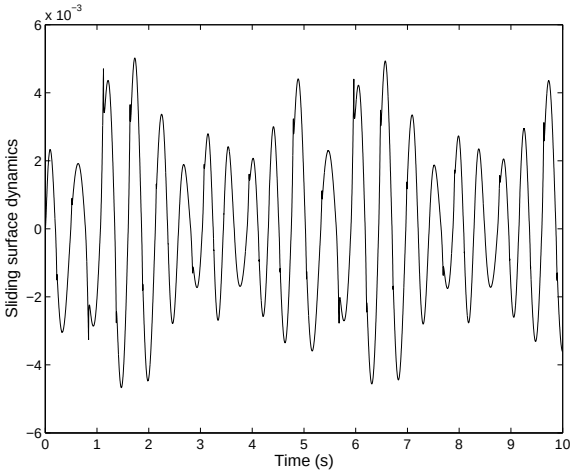

Figure 8.9 Sliding surface dynamics 's' (simulation case 2)

transmissibility stand-point. Since, the displacement transmissibility is less than one (no resonance effects), it would be reasonable to judge the performance mainly from the stand-point of acceleration (Fig. 8.6). Hence, for this simulation case, the controller was observed to provide excellent performance with respect to passenger comfort while maintaining good road handling qualities. Also, the control effort was observed to be able to bound the tracking error to a relatively small magnitude.

Experimental testing was then performed for the same controller configuration to get a head-to-head comparison not only with simulation, but, also with the experimentally obtained performance for the skyhook control case. From Figs. 8.10 and 7.9, it can be observed that the sliding mode controller provides a much superior acceleration transmissibility as compared to the skyhook scheme. In fact, the experimentally observed performance for the sliding mode controller rivals that obtained in simulation for the skyhook controller (Fig. 7.8). *This justifies the claim that while the skyhook controller predicted a good performance in the simulation study, the inherent limitations of the control scheme discussed earlier, caused the experimental performance to degrade. However, since the sliding mode controller is able to mitigate all the limitations of the*

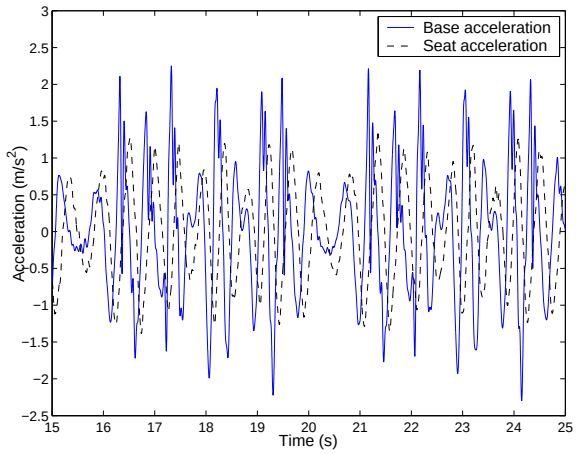

Figure 8.10 Acceleration transmissibility (experiment case 2)

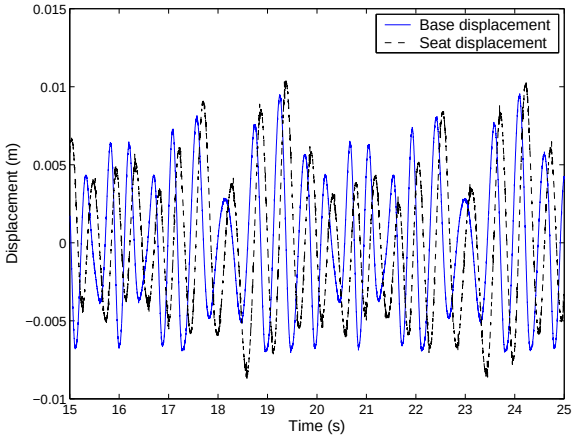

Figure 8.11 Displacement transmissibility (experiment case 2)

original skyhook control by including the error dynamics in feedback, the experimental performance closely replicates that of the simulation both for the original skyhook control (fig. 7.8) and for the sliding mode control (Fig. 8.6). This also justifies the robustness claims made regarding the sliding mode scheme, since, the plant being controlled was assumed to behave like a second order even though it is of a higher order in real-life (Fig. 6.2). Approximated analytical expressions and empirical co-relations were also utilized to quantify the system parameters such as spring stiffness/ damping and the controller was able to account for all these parametric uncertainties as well.

Comparing Figs. 8.11 and 8.4, it can be noticed that the sliding mode controller achieves a better displacement transmissibility, especially on the suspension downstroke. This shows that the damper is able to provide adequate damping and at the correct instant in time so as to arrest resonance caused by the low frequency component of the base excitation signal. *This is a significant performance achievement, since, one major drawback of accumulated airsprings is that they are susceptible to suspension bottom-out due to the compressibility of air and the fact that the suspension is made "soft" by accumulation.*

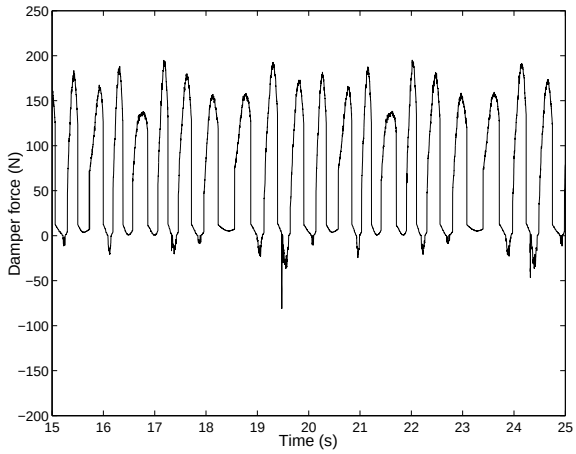

Figure 8.12 Damper force (experiment case 2)

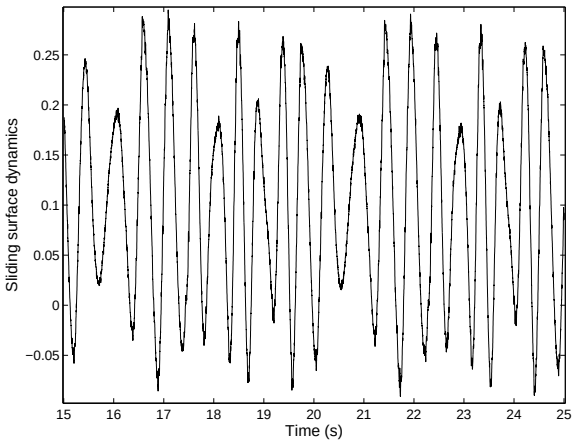

Figure 8.13 Sliding surface dynamics 's' (experiment case 2)

Figure 8.12, shows the damping force commanded by the sliding mode controller. Comparing this with Fig. 8.5, it is noticed that although the damping force magnitude is higher for the sliding mode controller, it is applied only when required based on the sliding surface dynamics (Fig. 8.13) and at other times, the controller allows the inherent vibration isolation characteristic of accumulation to attenuate the vibration.

Hence, from this head-to-head performance comparison between the sliding mode and skyhook control schemes, it can be concluded that the sliding mode controller is able to retain all the advantages of the ideal skyhook logic, while at the same time, mitigating its drawbacks to a great extent. In addition, the sliding mode controller showed robustness to different types of modeling and parametric uncertainties while delivering excellent performance. After several iterations, the controller configuration used in "test-set 2" was found to be the best from a performance standpoint. However, from an research/academic stand-point, it is important to observe and understand the effect that each controller design parameter has on the overall performance. In this view, a thorough study was conducted to ascertain the controller performance for different parametric configurations and is presented as test-cases below.

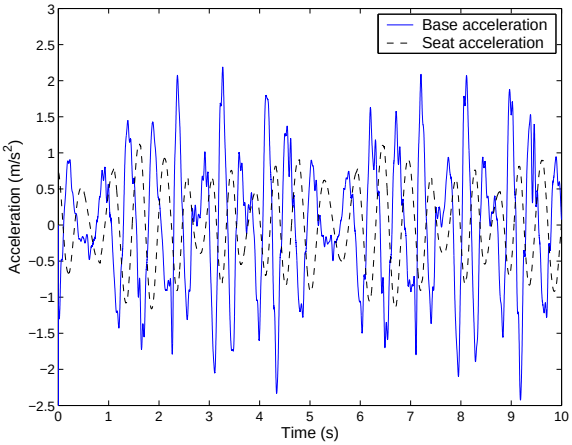

Figure 8.14 Acceleration transmissibility (simulation case 3)

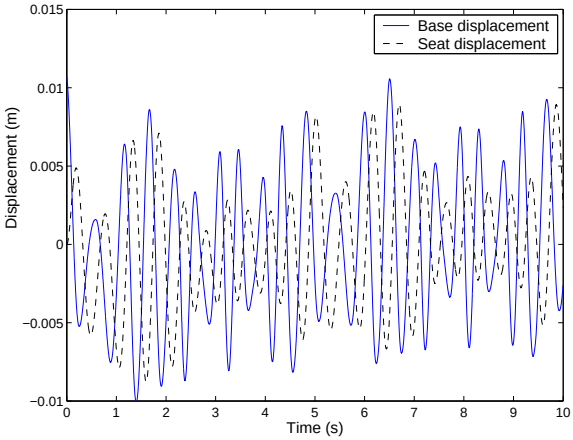

Figure 8.15 Displacement transmissibility (simulation case 3)

Test-case 3: As mentioned in the lead-up to the design of the sliding mode controller, several design parameters can be tuned to synthesize the best possible controller configuration. In the next several cases including this one, the controller design parameters are changed to understand its impact on the closed loop performance. It will also help the reader appreciate the flexibility that sliding mode control provides for optimizing the controller as compared to the original skyhook law, which has no such advantage.

For this test case, the boundary layer thickness was increased to $\Phi = 0.1$. The unchanged parameters were: The switching term constant $\eta = 1 \Rightarrow K = \eta * M_a = 90$; weighting for displacement error $\lambda_1 = 4$; and weighting for the integral of displacement error $\lambda_3 = 16$. As explained in section A.0.4, the boundary layer is used to produce a continuous switching function so as to prevent extreme and abrupt changes in control activity. The boundary layer thickness "Φ" in turn determines how aggressively the switching happens to keep the system dynamics in sliding mode. Hence, increasing the value Φ should add delay to the control activity, causing the performance to degrade.

Figures 8.14 and 8.15 show a degradation of performance as anticipated, with dis-

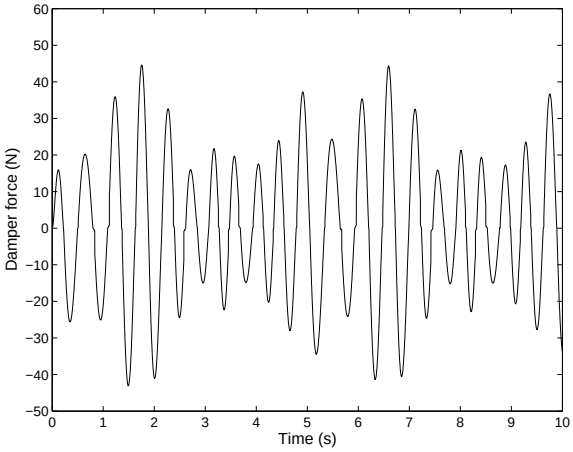

Figure 8.16 Damper force (simulation case 3)

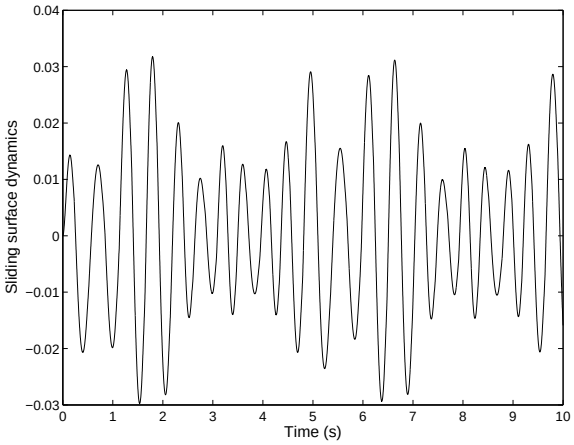

Figure 8.17 Sliding surface dynamics 's' (simulation case 3)

placement transmissibility degrading to a more considerable extent. The damper force (Fig. 8.16) shows that the sudden changes in control force seen in Fig. 8.8 for case 2 are absent due to this increased delay. Also, the tracking error (Fig. 8.17) increases five-fold as compared to case 2 (Fig. 8.9). Comparing Fig. 8.16 with Fig. 8.8, the magnitude of control is observed to remain the same, since, increasing the boundary layer thickness only causes the saturation function (s/Φ) to reduce the slope resulting in a delayed control action. Since, the gain of the controller is unaltered by changing Φ, this increased delay in control results in increasing magnitude of tracking error, thereby degrading the performance.

Figures 8.18, 8.19 and 8.20 show the experimentally obtained result and corroborate the expected result. From Figs. 8.18 and 8.19 the degradation in acceleration as well as displacement transmissibilities is evident. Comparing Figs. 8.20 and 8.20, it is noticed that even though the magnitude of control is not increased, the increased delay in control makes the controller compensate by demanding damping even during suspension jounce. Comparing the plots for the sliding surface dynamics (Figs. 8.13 and 8.21), the increase in tracking error is also evident.

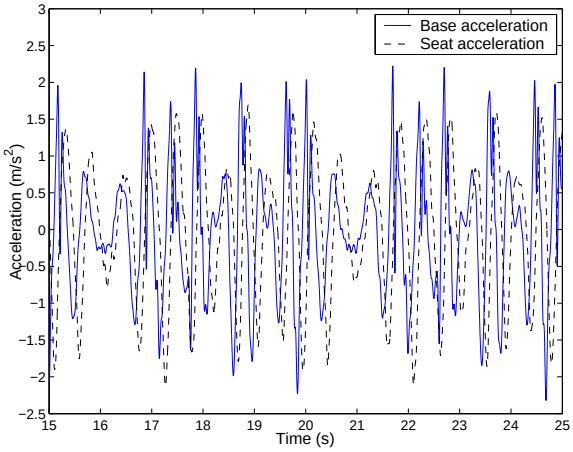

Figure 8.18 Acceleration transmissibility (experiment case 3)

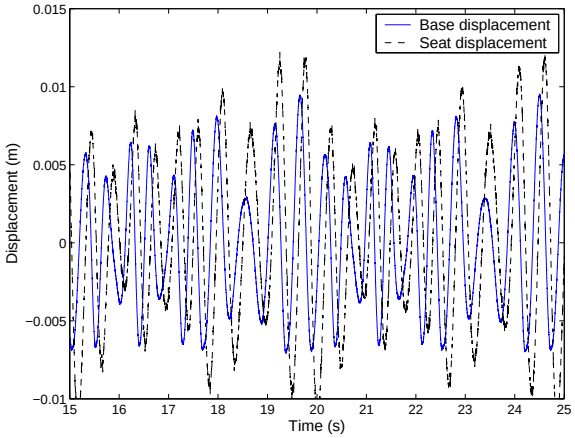

Figure 8.19 Displacement transmissibility (experiment case 3)

Test-case 4: For this case, the boundary layer thickness was decreased to $\Phi = 0.001$. The unchanged parameters were: The switching term constant $\eta = 1 \Rightarrow K = \eta * M_a = 90$; weighting for displacement error $\lambda_1 = 4$; and weighting for the integral of displacement error $\lambda_3 = 16$.

Compared to test-case 3, decreasing the value Φ should produce a more aggressive control activity, since, slope of the saturation function (s/Φ) increases. Figure 8.24, which shows the damper force (control input) is almost twice as compared to case 2 (Fig. 8.8) and thus justifies the argument. However, Figs. 8.26 and 8.27 show only a slight improvement in acceleration as well as displacement transmissibilities. Hence, when the significant increase in damper force as well as bandwidth are weighed against the lesser significant improvement in performance, the controller of case 2 is a more practical choice.

Similar to the simulation plot for damper force (Fig. 8.24), the experimentally observed damper force (Fig. 8.28) also has sharp spikes in the force profile, thus, corroborating the claim of increased bandwidth demand placed by reducing the boundary layer thickness. This is also justified by comparing Figs. 8.28 and 8.20, and observing

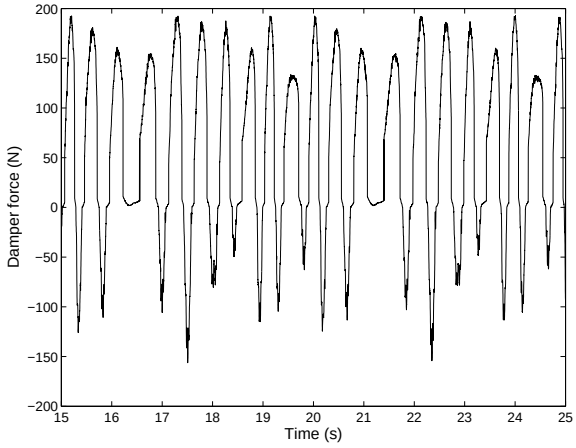

Figure 8.20 Damper force (experiment case 3)

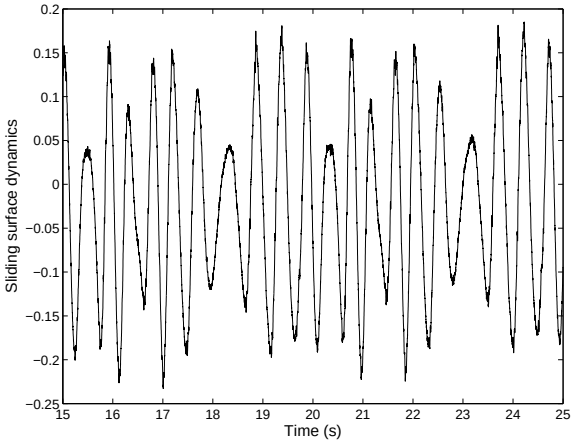

Figure 8.21 Sliding surface dynamics 's' (experiment case 3)

the spike activity. Figs. 8.26 and 8.27 show the improvement in acceleration as well as displacement transmissibilities as compared to case 3 (Fig. 8.18 and 8.19).

Simulation case 5: For this case, the switching term η was reduced to 0.1 ($\eta = 0.1 \Rightarrow K = \eta * M_a = 9$). The unchanged parameters were: The boundary layer thickness $\Phi = 0.01$; weighting for displacement error $\lambda_1 = 4$; and weighting for the integral of displacement error $\lambda_3 = 16$.

The switching term basically ensures that the sliding mode condition of Eq. A.13 is satisfied. If this term is reduced drastically, stability in the presence of uncertainties may not be guaranteed. However, decreasing the value of η to a reasonable extent reduces the magnitude of the switching term, which, in turn reduces the control magnitude. Figure 8.36 shows the damper force demanded by the controller and corroborates the expected result. As regards to performance, Figs. 8.34 and 8.35 show degradation in acceleration as well as displacement transmissibilities due to the decreased control effort. This degradation in performance is also clearly noticed in the sliding surface dynamics plot (Fig. 8.33), where the error magnitude increases by an order of seven times as

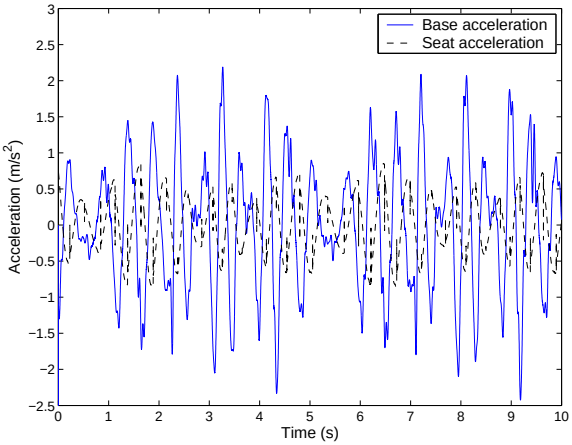

Figure 8.22 Acceleration transmissibility (simulation case 4)

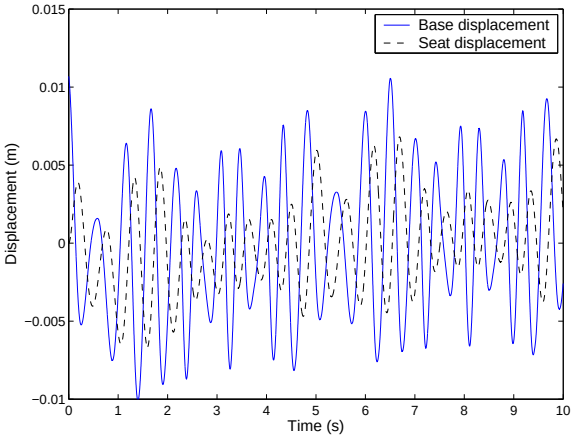

Figure 8.23 Displacement transmissibility (simulation case 4)

compared to case 2 (Fig. 8.9).

The effect of reducing the switching term can also be noticed in the experimental performance of the pneumatic system. As compared to the damper force demanded by the controller in case 2 (Fig. 8.12), the magnitude of the control effort reduces (Fig. 8.36) by half. Also, due to this reduced control effort, degradation in acceleration as well as displacement transmissibilities (Figs. 8.34 and 8.35) can be clearly noticed when compared with Figs. 8.10 and 8.11, thereby corroborating the expected result.

Test-case 6: In this last case considered, the switching term η was increased to 2 ($\eta = 2 \Rightarrow K = \eta * M_a = 180$). The unchanged parameters were: The boundary layer thickness $\Phi = 0.01$; weighting for displacement error $\lambda_1 = 4$; and weighting for the integral of displacement error $\lambda_3 = 16$.

Increasing the value η has a direct effect on the magnitude of control input. Figure 8.44 shows that increasing the value of η, increases the magnitude of control input (compared with case 2). According to the simulation plots (Figs. 8.38 and 8.39), both

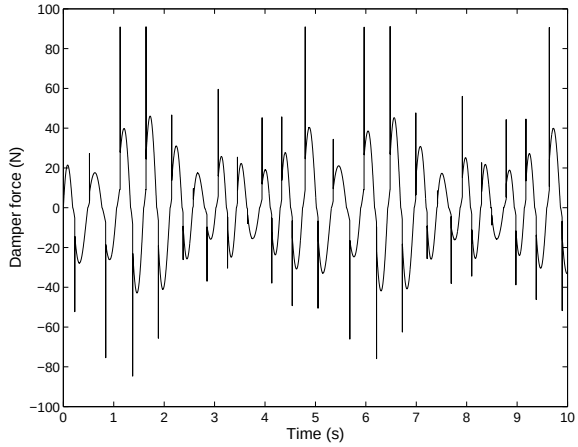

Figure 8.24 Damper force (simulation case 4)

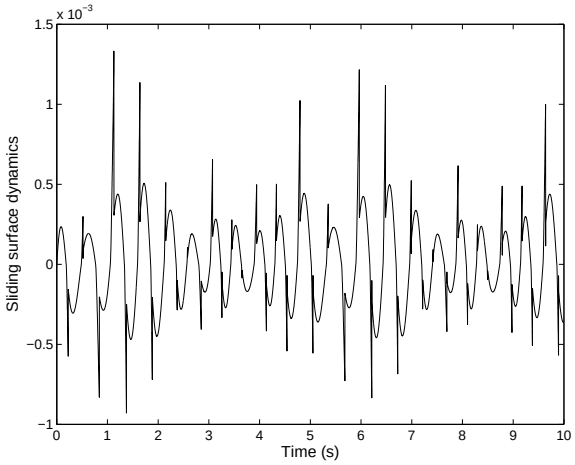

Figure 8.25 Sliding surface dynamics 's' (simulation case 4)

the acceleration and displacement transmissibilities are improved on account of increased control effort. However, from the corresponding experimental plots (Figs. 8.42 and 8.43), the opposite trend is observed. The reason for this could be that, the system assumed in the simulation study is strictly a 2^{nd}-order system, whereas, the actual system is of higher order. Hence, increasing the control gain is probably exciting higher frequency dynamics not accounted for in the simulation model.

Figure 8.44 shows that this expected result is indeed the case. Figures 8.42 and 8.43 show degradation in acceleration as well as displacement transmissibilities. This result also shows that more than adequate damping only degrades the performance.

In this chapter, the synthesis of a model matching sliding mode controller for closed-loop control of the pneumatic system was presented. Lyapunov stability analysis was also used to synthesize parameters in the controller and guarantee asymptotic stability of the closed-loop system. The performance of the sliding mode controller was shown to be superior to that obtained for the skyhook controller designed in chapter 7. The following chapter summarizes the original contributions of the thesis and sheds light on some critical areas that need further research.

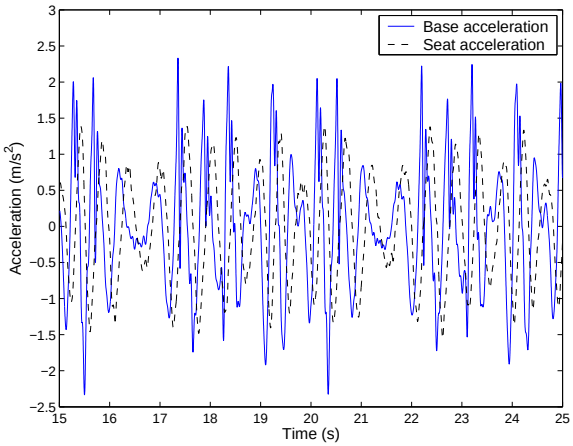

Figure 8.26 Acceleration transmissibility (experiment case 4)

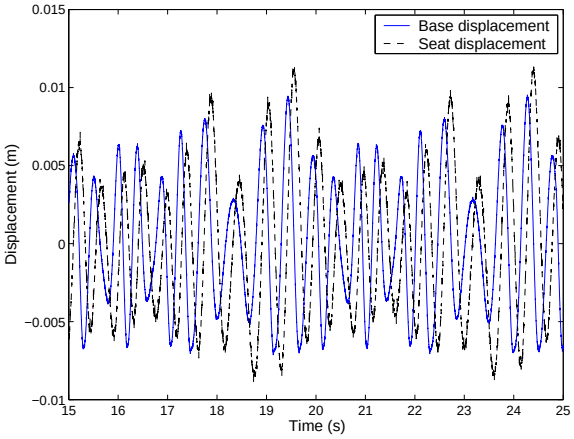

Figure 8.27 Displacement transmissibility (experiment case 4)

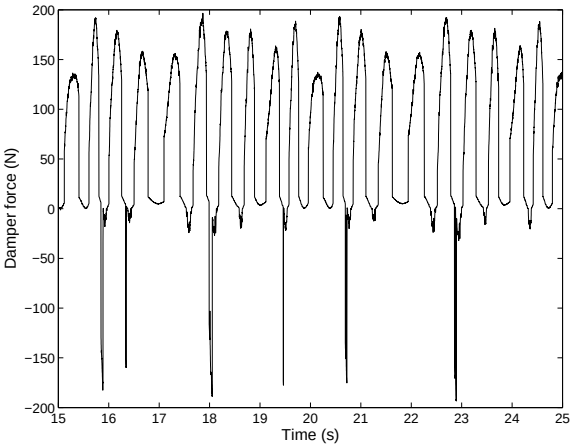

Figure 8.28 Damper force (experiment case 4)

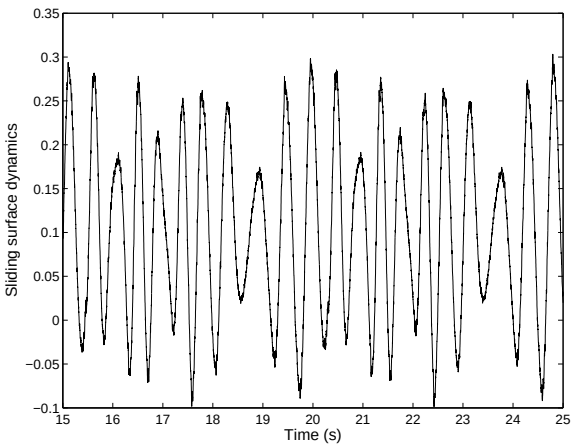

Figure 8.29 Sliding surface dynamics 's' (experiment case 4)

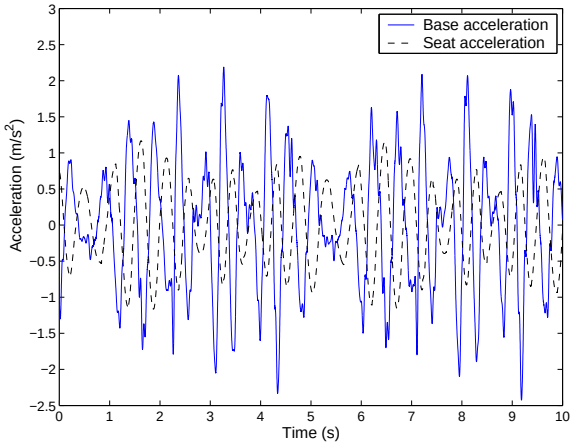

Figure 8.30 Acceleration transmissibility (simulation case 5)

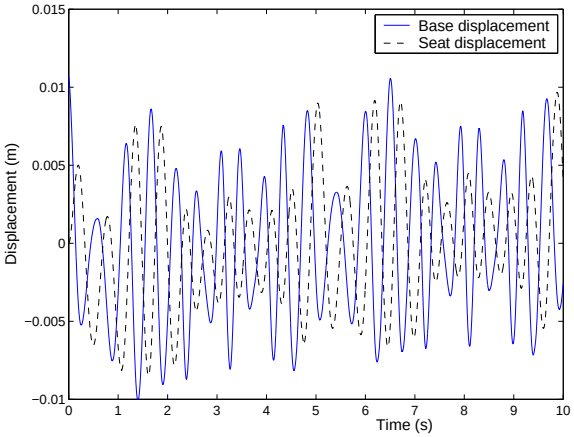

Figure 8.31 Displacement transmissibility (simulation case 5)

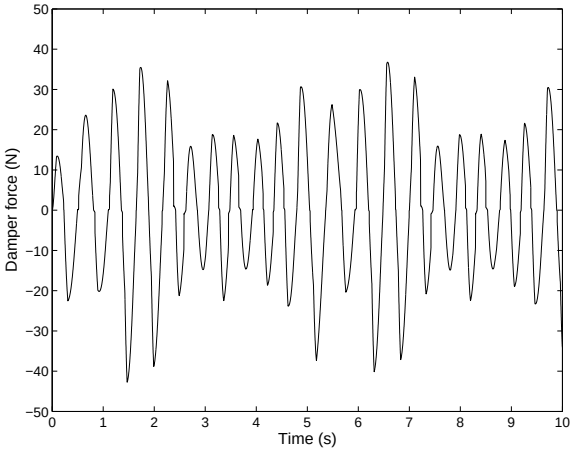

Figure 8.32 Damper force (simulation case 5)

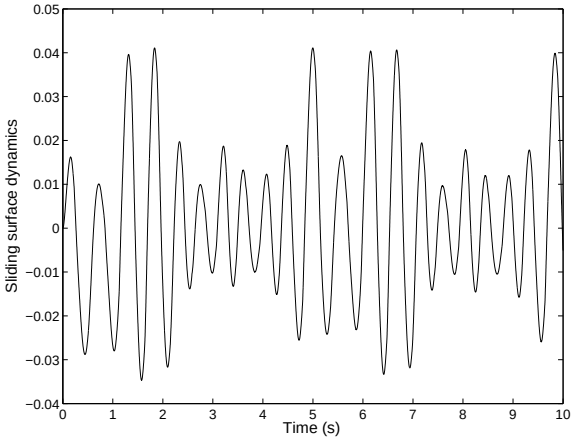

Figure 8.33 Sliding surface dynamics 's' (simulation case 5)

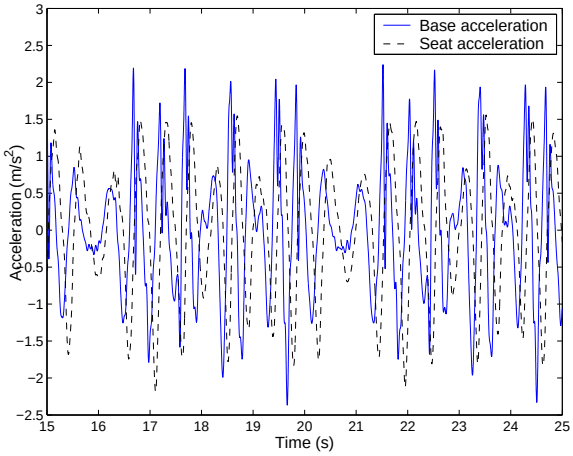

Figure 8.34 Acceleration transmissibility (experiment case 5)

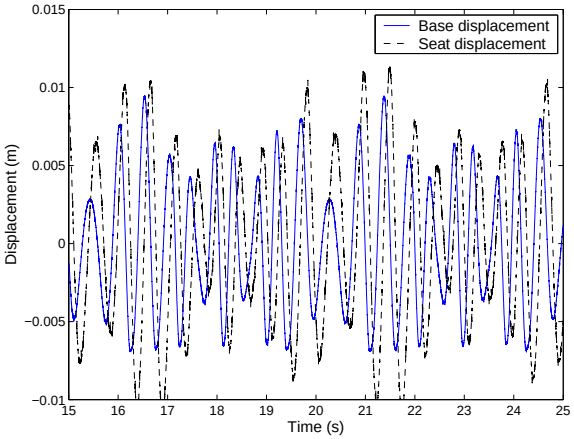

Figure 8.35 Displacement transmissibility (experiment case 5)

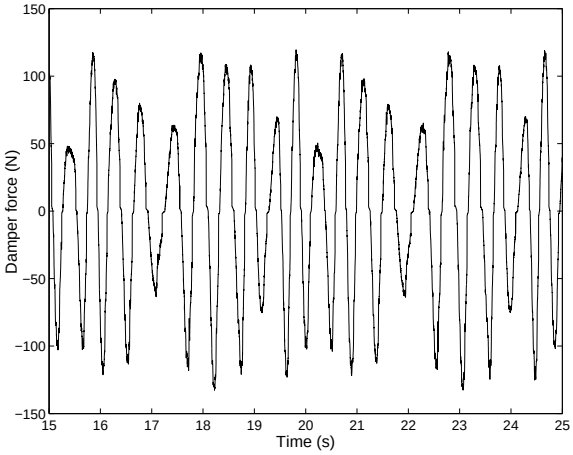

Figure 8.36 Damper force (experiment case 5)

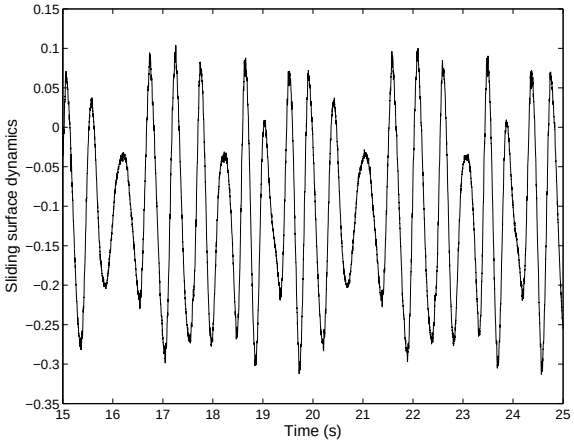

Figure 8.37 Sliding surface dynamics ‘s’ (experiment case 5)

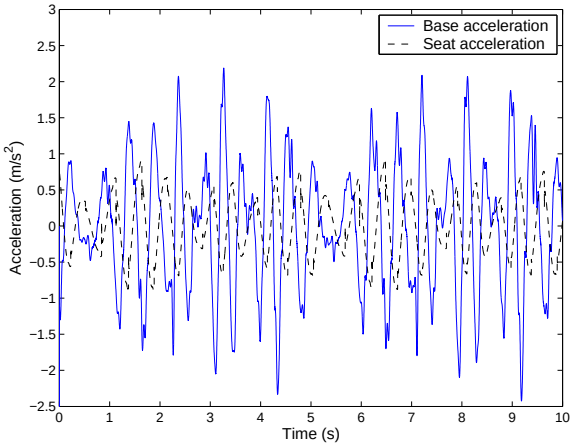

Figure 8.38 Acceleration transmissibility (simulation case 6)

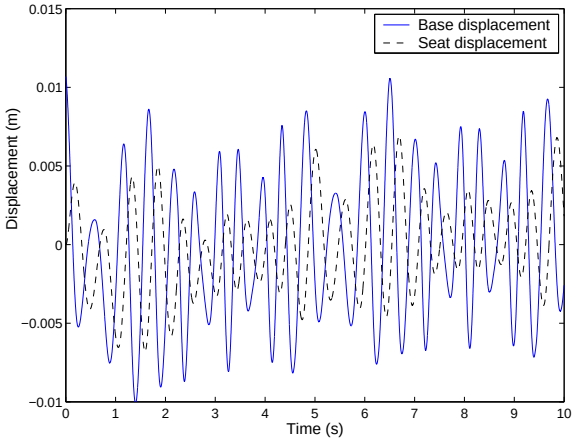

Figure 8.39 Displacement transmissibility (simulation case 6)

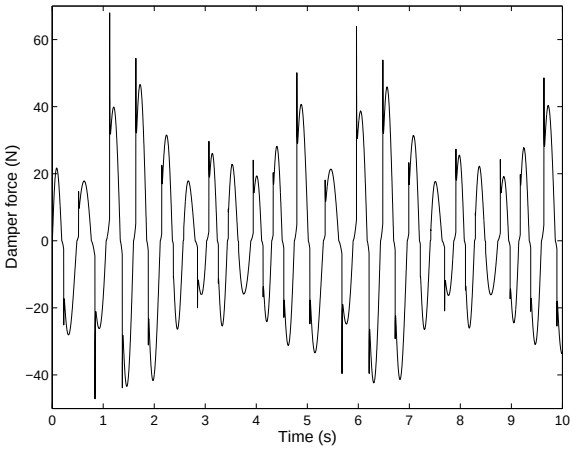

Figure 8.40 Damper force (simulation case 6)

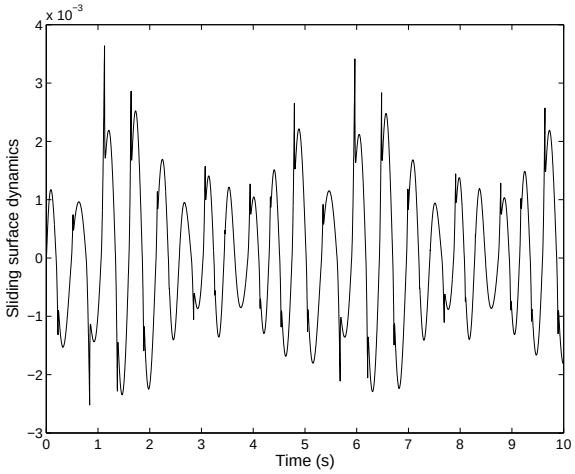

Figure 8.41 Sliding surface dynamics 's' (simulation case 6)

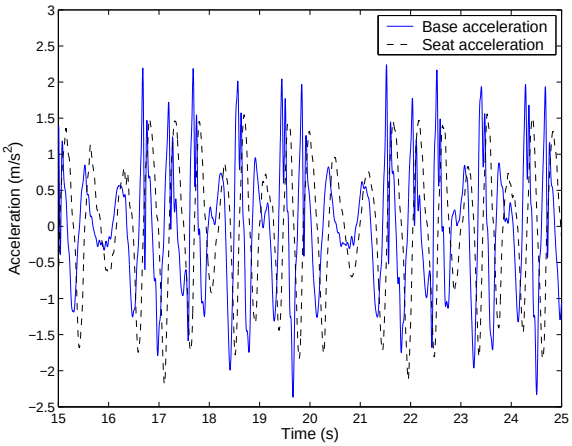

Figure 8.42 Acceleration transmissibility (experiment case 6)

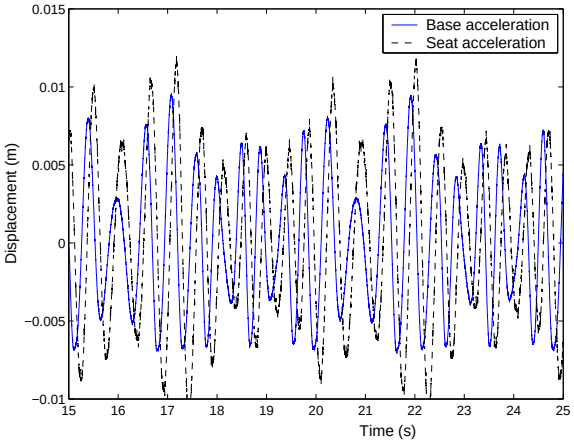

Figure 8.43 Displacement transmissibility (experiment case 6)

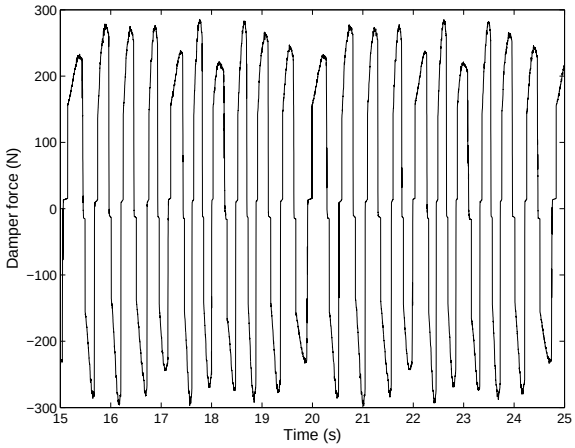

Figure 8.44 Damper force (experiment case 6)

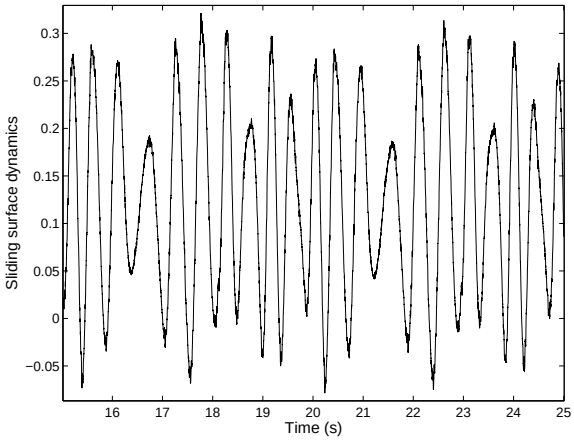

Figure 8.45 Sliding surface dynamics 's' (experiment case 6)

CHAPTER 9. Summary and discussion

This dissertation presented the modeling, analysis and non-linear control of a novel semi-active pneumatic vibration isolation technology. A real-world field-test project was undertaken to establish the need for additional research in the area of seat/cab suspension design (as one possible application). With this motivation and information available on a novel pneumatic vibration isolator invented in (66), research was initiated. The original contributions of this research study are enumerated below.

1. The components of the novel pneumatic system configuration specified in (66) were modeled from first principles and empirical co-relations to produce a high fidelity non-linear mathematical model.

2. An exhaustive computational study of the non-linear model was conducted and preliminary conclusions were derived hypothesizing a second-order system behavior. This hypothesis yielded the discovery of the continuously variable natural frequency and damping (CVNFD) characteristic of the pneumatic isolator. The computationally analyzed system dynamics were corroborated through experimental testing. One particular configuration of the pneumatic system , corresponding to a constant natural frequency with continuously variable damping was identified to be the most suitable configuration for controller design.

3. A modified mathematical model quantifying the pneumatic system configuration was developed. It comprised of a spring with constant stiffness whose value was

derived analytically from fundamental governing laws and a variable force damper whose characteristics were experimentally identified.

4. A model independent control scheme called skyhook control was utilized to regulate airspring induced variable damping. The skyhook law in its original form was shown to be unsuitable for implementation and a modified version of the algorithm was proposed, tested in simulation and successfully implemented on the hardware.

5. A more advanced non-linear robust control scheme called sliding mode control was identified to be suitable for controller design. The controller was synthesized using the sliding mode control theory applied to the theory of model-matching. Lyapunov stability analysis was applied and the sliding mode controller was modified to guarantee global asymptotic stability. It was demonstrated computationally as well as experimentally that by suitably choosing the several controller design-parameters, the skyhook based sliding mode controller can recover the performance lost by implementing the model independent skyhook law.

In summary, the research conducted in this thesis demonstrated the availability and feasibility of a new and novel semi-active pneumatic vibration isolation technology that can replace and/or enhance the performance of contemporary passive and semi-active systems. While this technology has matured to a stage where it could be implemented on on-road vehicles, additional experimentation is required to make this technology a viable option for stand-alone implementation in extremely harsh environments, such as in off-road vehicle applications. In view of this, an area identified for further research is the design an orifice geometry that can produce a greater damping range. Additional research on accumulator volume-modulator is also recommended for future work. The highly encouraging experimental results backed by a thorough understanding of the underlying physics of the problem as a result of this thesis study, provide credibility and motivation for furthering the research in the suggested areas.

APPENDIX A. Sliding mode control : Introduction

The material in this appendix was taken from (65) to serve as a reference for the reader and hopefully aid in better understanding of the material presented in chapter 8.

Mathematical modeling of real-world systems is invariably an approximation leading to inaccuracies. Model imprecision may come from actual uncertainty about the plant (eg: unknown plant parameters), or from the purposeful choice of a simplified representation of the system's dynamics (eg: neglecting structural modes in a reasonably rigid mechanical system). It is a well known fact that these modeling inaccuracies can have strong adverse effects on nonlinear control systems. Therefore, any practical design must address them explicitly.

A simple approach to robust control, is the so-called sliding mode control. Intuitively, it is based on the remark that it is much easier to control 1^{st} order systems, be they nonlinear or uncertain, than it is to control general n^{th} order systems. In sliding mode control methodology, these n^{th} order problems are replaced by equivalent 1^{st} order problems. It will be shown in the ensuing sections that, for this transformed system, "perfect" performance in principle be achieved in the absence of arbitrary parameter uncertainties.

Thus, for the class of systems to which it applies, sliding mode controller design provides a systematic approach to the problem of maintaining stability and consistent performance in the face of modeling imprecisions (65).

A.0.1 Sliding surfaces

Consider the single-input dynamic system,

$$x^{(n)} = f(x) + b(x)u \tag{A.1}$$

where, the scalar x is the output of interest (in our case, the displacement measurement), the scalar u is the control input (in our case, the orifice damping), and $X = [x \ \dot{x} \ \ldots \ x^{(n-1)}]^T$ is the state vector.

In A.1, the function $f(x)$ (in general non-linear) is not exactly known, but, the extent of imprecision on $f(x)$ is upper bounded by a known continuous function of x; similarly, the control gain $b(x)$ is not exactly known, but is of known sign and is bounded by known, continuous functions of x. The control problem is to get the state X to track a specific time varying state $X_d = [x_d \ \dot{x_d} \ \ldots \ x_d^{(n-1)}]^T$ in the presence of model imprecision on $f(x)$ and $b(x)$.

For the tracking task to be achievable using finite control u, the initial desired state $X_d(0)$ must be such that,

$$X_d(0) = X(0) \tag{A.2}$$

If this condition is not satisfied, tracking can be achieved only after a transient. For example: In a second order system, position or velocity cannot "jump", so that any desired trajectory feasible from time $t = 0$ necessarily starts with the same position and velocity as those of the plant. In this case, these variables asymptotically converge to the desired trajectory in finite time after the control effort has been applied.

A.0.1.1 Notation

Let $e = X - X_d$ be the tracking error in the variable x, and let

$$E = X - X_d = [e \ \dot{e} \ \ldots \ e^{(n-1)}]^T \tag{A.3}$$

be the tracking error vector. Furthermore, let us define a time-varying surface $S(t)$ in the state-space $R^{(n)}$ by the scalar equation $s(X,t)$, where,

$$s(X,t) = \left(\frac{d}{dt} + \lambda\right)^{n-1} e \tag{A.4}$$

and λ is a strictly positive constant, whose choice we shall interpret later. For instance, if $n = 2$,

$$s = \dot{e} + \lambda e \tag{A.5}$$

i.e., s is simply a weighted sum of the position error and the velocity error; if $n = 3$,

$$s = \ddot{e} + 2\lambda \dot{e} + \lambda^2 e \tag{A.6}$$

Given initial condition (Eq. A.2, the problem of tracking $X \equiv X_d$ is equivalent to that of remaining on the surface $S(t)$ for all $t > 0$; indeed $s \equiv 0$ represents a linear differential equation whose unique solution is $e \equiv 0$, given initial conditions (Eq. A.2. Thus, the problem of tracking the n-dimensional vector X_d can be reduced to that of keeping the scalar quantity 's' at zero.

More precisely, the problem of tracking the n-dimensional vector X_d (i.e., the original n^{th}-order tracking problem in x) can in effect be replaced by a 1^{st}-order stabilization problem in s. Indeed, since from Eq. A.4, the expression of s contains e^{n-1}, we only need to differentiate s once for the input u to appear.

Furthermore, bounds on s can be directly translated into bounds on the tracking error vector E, and therefore the scalar s represents a true measure of tracking performance. Specifically, assuming that $E(0) = 0$ (the effect of non-zero initial conditions in E can be added seperately), we have,

$$\forall t \geq 0, |s(t)| \leq \Phi \quad \Rightarrow \quad \forall t \geq 0, \left|e^{(i)}(t)\right| \leq (2\lambda)^i \varepsilon \quad i = 0, ..., n-1 \tag{A.7}$$

where, $\varepsilon = \Phi/\lambda^{(n-1)}$.

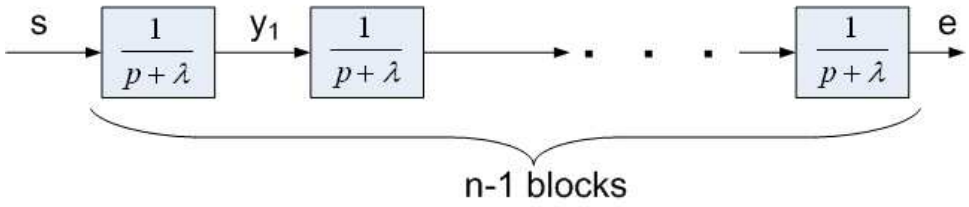

Figure A.1 Computing bounds on error 'e'

Proof: Indeed, by definition (eq. A.4), the tracking error e is obtained from s through a sequence of first-order lowpass filters (Fig. A.1, where $p = (d/dt)$ is the Laplace operator). Let y_1 be the output of the first filter. We have,

$$y_1(t) = \int_0^t e^{-\lambda(t-T)} s(T) dT \tag{A.8}$$

From $|s(t)| \leq \Phi$ we thus get,

$$|y_1(t)| \leq \Phi \int_0^t e^{-\lambda(t-T)} dT = (\Phi/\lambda)(1 - e^{-\lambda t}) \leq \Phi/\lambda \tag{A.9}$$

We can apply the same reasoning to the second filter, and so on, all the way to $y_{n-1} = e$. We then get,

$$|e| \leq \Phi/\lambda^{n-1} = \varepsilon \tag{A.10}$$

Similarly, e^i can be thought of as obtained though the sequence of Fig. A.2. From the previous result, one has $|z_1| \leq \Phi/\lambda^{n-1-i}$, where z_1 is the output of the $(n-i-1)^{th}$ filter. Furthermore, noting that

$$\frac{p}{p+\lambda} = \frac{p+\lambda-\lambda}{p+\lambda} = 1 - \frac{\lambda}{p+\lambda} \tag{A.11}$$

one sees that the sequence of Fig. A.2 implies that

$$\left|e^{(i)}\right| \leq \left(\frac{\Phi}{\lambda^{n-i-1}}\right)\left(1 + \frac{\lambda}{\lambda}\right)^i = (2\lambda)^i \varepsilon \tag{A.12}$$

Finally, in the case that $e(0) \neq 0$, bounds (Eq. A.7 are obtained asymptotically, i.e., within a short time-constant $(n-1)/\lambda$.

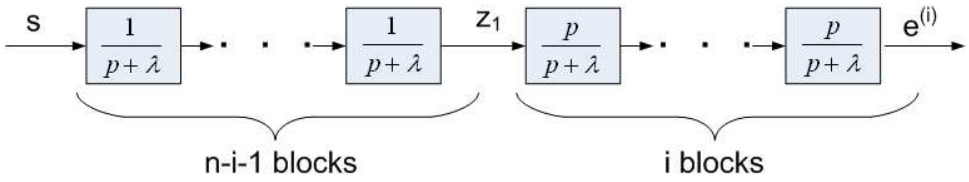

Figure A.2 Computing bounds on error 'e'

Thus, an n^{th}-order tracking problem has been in effect been replaced by a 1^{st}-order stabilization problem, and the corresponding transformed performance measures have been quantified by Eq. A.7.

The simplified 1^{st}-order stabilization problem of keeping the scalar s at zero can now be achieved by choosing the control law u of Eq. A.1 such that outside of $S(t)$

$$\frac{1}{2}\frac{d}{dt}s^2 \leq -\eta\,|s| \tag{A.13}$$

where, η is a strictly positive constant. Essentially, Eq. A.13 states that the squared "distance" to the surface, as measured by s^2, decreases along all system trajectories. Thus, it constraints trajectories to point towards the surface $S(t)$, as shown in Fig. A.3. In particular, once on the surface, the system trajectories remain on the surface. In other words, satisfying condition (Eq. A.13, or "sliding condition", makes the surface an invariant set. Graphically, this corresponds to the fact that in Fig. A.3, the trajectories off the surface can "move" while still pointing towards the surface.

$S(t)$ **verifying Eq. A.13 is referred to as a "Sliding Surface", and the system's behavior on the surface is called "Sliding Regime" or "Sliding Mode".**

The other interesting aspect of the invariant set $S(t)$ is that once on it, the system trajectories are defined by the equation of the set itself, namely

$$s(X,t) = \left(\frac{d}{dt} + \lambda\right)^{n-1} e = 0 \tag{A.14}$$

In other words, the surface $S(t)$ is both a place and dynamics. This fact is simply

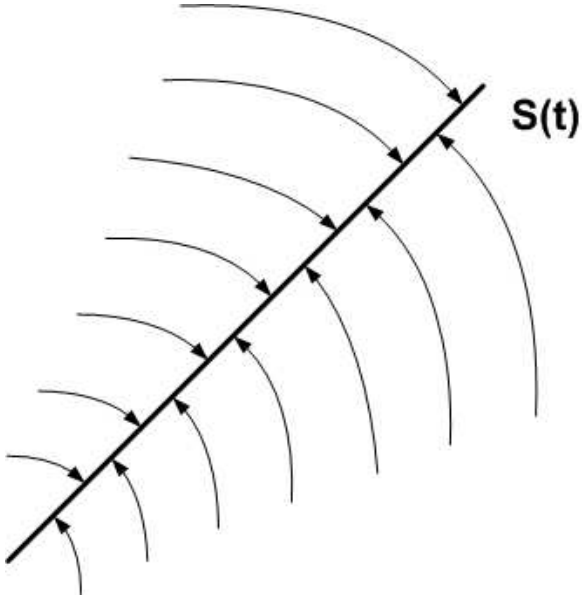

Figure A.3 Computing bounds on error 'e'

the geometric interpretation of replacing an n^{th}-order tracking problem by a 1^{st}-order stabilization problem.

Finally, satisfying Eq. A.13 guarantees that if condition Eq. A.2 is not exactly satisfied, i.e., if $X(t=0)$ is actually off $X_d(t=0)$, the surface $S(t)$ will nonetheless be reached in a finite time smaller than $|s(t=0)|/\eta$.

Proof: Indeed, let's assume that $s(t=0) > 0$, and let t_{reach} be the time required to hit the surface $s=0$. Integrating Eq. A.13 between $t=0$ and $t=t_{reach}$ leads to,

$$0 - s(t=0) = s(t=t_{reach}) - s(t=0) \leq -\eta(t_{reach} - 0) \tag{A.15}$$

which implies that

$$t_{reach} \leq |s(t=0)|/\eta \tag{A.16}$$

Note: Similar result is obtained starting with $s(t=0) < 0$

Furthermore, definition (Eq. A.4) implies that once on the surface, the tracking error tends exponentially to zero, with a time constant $(n-1)/\lambda$ (from the sequence of

(n-1) filters of time constants equal to $1/\lambda$). The typical system behavior implied by

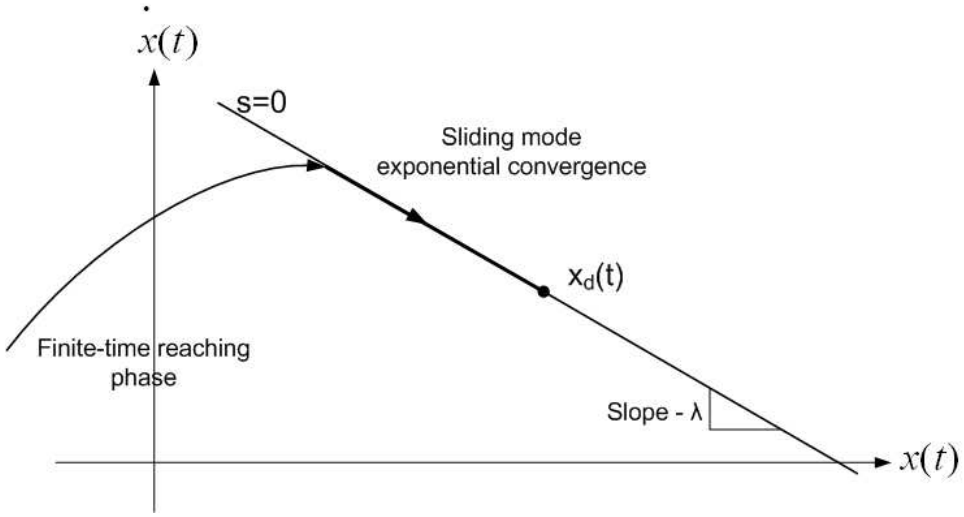

Figure A.4 Graphical interpretation of sliding condition

satisfying sliding condition (Eq. A.13 is illustrated in Fig. A.4 for $n = 2$. The sliding surface is a line in the phase plane, of the slope $-\lambda$ and containing the (time-varying) point $X_d = [x_d \quad \dot{x_d}]^T$. Starting from any initial condition, the state trajectory reaches the time-varying surface in a finite time smaller than $|s(t=0)|/\eta$, and then slides along the surface towards x_d exponentially, with a time-constant equal to $1/\lambda$.

In summary, the idea behind Eqs. A.4 and A.13 is to pick-up a well-behaved function of the tracking error, s, according to Eq. A.4, and then select the feedback control law u in Eq. A.1 such that s^2 remains a Lyapunov-like function of the closed-loop system, despite the presence of model imprecision and of disturbances.

A.0.2 Filippov's construction of the equivalent dynamics

The system's motion on the sliding surface can be given an interesting geometric interpretation, as an "average" of the system's dynamics on both sides of the surface.

The dynamics while on the sliding mode can be written as,

$$\dot{s} = 0 \tag{A.17}$$

By solving the above equation formally for the control input, we obtain an expression for u called the "equivalent control", u_{eq}, which can be interpreted as the continuous control law that would maintain $\dot{s} = 0$ if the dynamics were exactly known. For instance, for a system of the form

$$\ddot{x} = f + u \tag{A.18}$$

we have,

$$u_{eq} = -f + \ddot{x_d} - \lambda\dot{e} = 0 \tag{A.19}$$

and the system dynamics while in sliding mode is, of course,

$$\ddot{x} = f + u_{eq} = \ddot{x_d} - \lambda\dot{e} = 0 \tag{A.20}$$

Geometrically, the equivalent control can be constructed as

$$u_{eq} = \alpha u_+ + (1 - \alpha)u_- \tag{A.21}$$

i.e., as a convex combination of the values of u on both sides of the surface $S(t)$. The value of α can again be obtained formally from Eq. A.17, which corresponds to requiring that the system trajectories be tangent to the surface. This intuitive construction is summarized in Fig. A.5, where $f_+ = [\dot{x}f + u_+]^T$, and similarly $f_- = [\dot{x}f + u_-]^T$ and $f_{eq} = [\dot{x}f + u_{eq}]^T$ (derived formally in the early 1960's by Russian mathematician A.F. Filippov).

Recalling that the sliding motion on the surface corresponds to a limiting behavior as control switchings occur infinitely fast, the formal solution α of Eq. A.17 and A.21 can be interpreted as the average "residence time" of the trajectory on the side $s > 0$.

A.0.3 Integral control

A similar result to what would be obtained for the sliding mode formulation explained in the previous section can be achieved by using integral control, i.e., formally letting

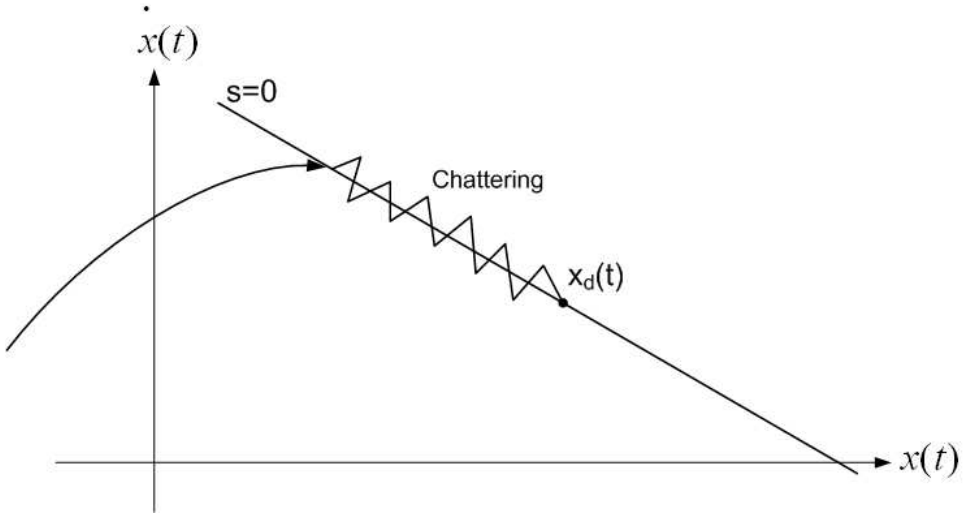

Figure A.5 Filippov's construction of the equivalent dynamics in sliding mode

$\left(\int_0^t e(r)dr\right)$ be the variable of interest. The system defined by Eq. A.18 is now third-order relative to the variable, and Eq. A.4 gives:

$$s = \left(\frac{d}{dt} + \lambda\right)^2 \left(\int_0^t e dr\right) = \dot{e} + 2\lambda e + \lambda^2 \int_0^t e dr \tag{A.22}$$

We obtain instead of Eq. A.19,

$$u_{eq} = -f + \ddot{x}_d - 2\lambda\dot{e} - \lambda^2 e \tag{A.23}$$

Note that $\left(\int_0^t e(r)dr\right)$ can be replaced by $\left(\int^t e(r)dr\right)$, i.e., the integral can be defined to within a constant. The constant can be chosen to obtain $s(t=0) = 0$ regardless of $x_d(0)$, by letting

$$s = \dot{e} + 2\lambda e + \lambda^2 \int_0^t e dr - \dot{e}(0) - 2\lambda e(0) \tag{A.24}$$

A.0.4 Continuous approximation of switching control laws

One main drawback of sliding control methodology is that, in order to account for the presence of modeling imprecision and of disturbances, the control law has to be

discontinuous across $S(t)$. Since, the implementation of the associated control switchings is necessarily imperfect (for instance, in practice, switching is not instantaneous and has a certain finite time-delay), this leads to "chattering" (Fig. A.6).

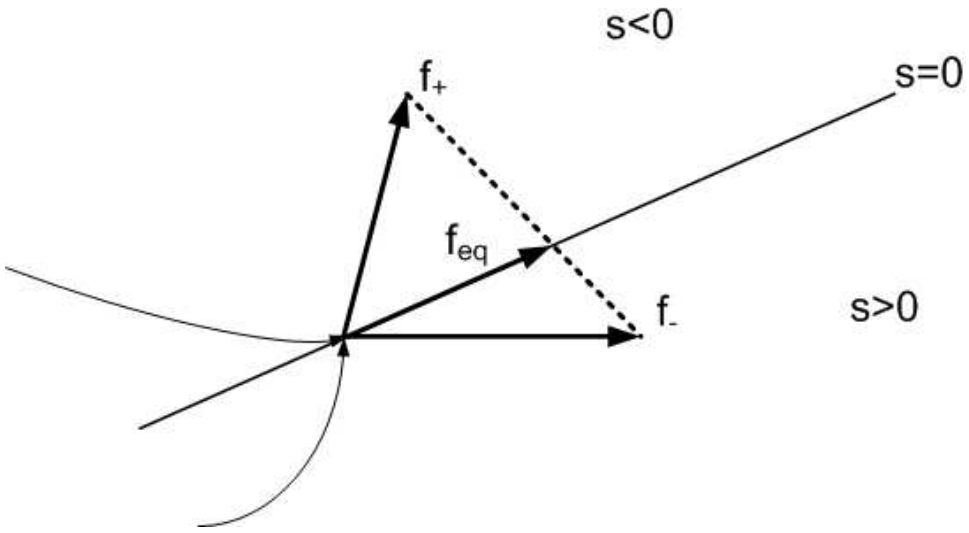

Figure A.6 Chattering as a result of imperfect control switching

Chattering is normally undesirable, since it involves high control activity and further may excite high-frequency dynamics neglected in the course of modeling. In other words, chattering must be eliminated for the controller to perform properly. This can be achieved by smoothing out the control discontinuity in a thin "boundary layer" neighboring the switching surface

$$B(t) = \{X, |s(X,t)| \leq \Phi\} \quad \Phi > 0 \tag{A.25}$$

where Φ is the boundary layer thickness, and $\epsilon = \Phi/\lambda^{n-1}$ is the boundary layer width, as Fig. A.7 illustrates for the case $n = 2$.

In other words, outside $B(t)$, the control law u is the same as before (i.e, satisfying the sliding condition Eq. A.13), which guarantees that the boundary layer is attractive, hence invariant: all trajectories starting inside $B(t = 0)$ remain inside $B(t)$ for all $t \geq 0$;

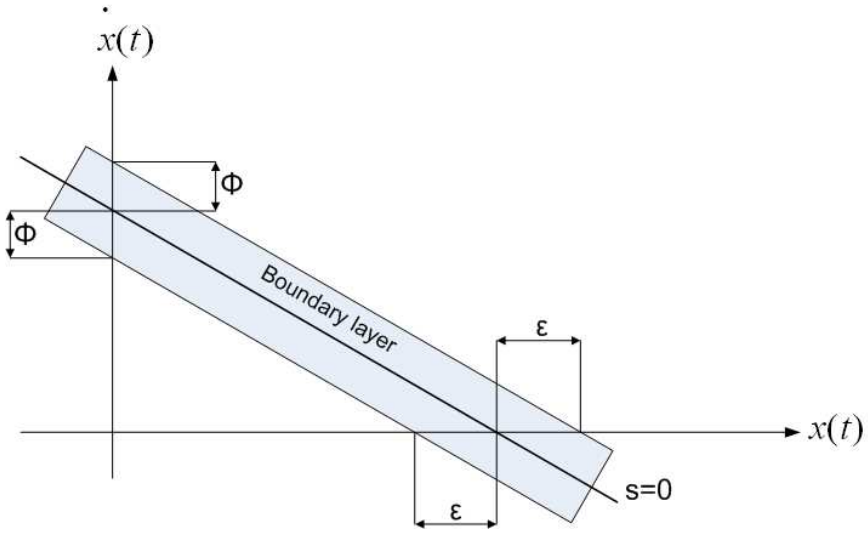

Figure A.7 The boundary layer

and we then interpolate u inside $B(t)$- for instance, replacing in the expression of u the term sgn(s) by s/Φ, inside $B(t)$, as illustrated in Fig. A.8.

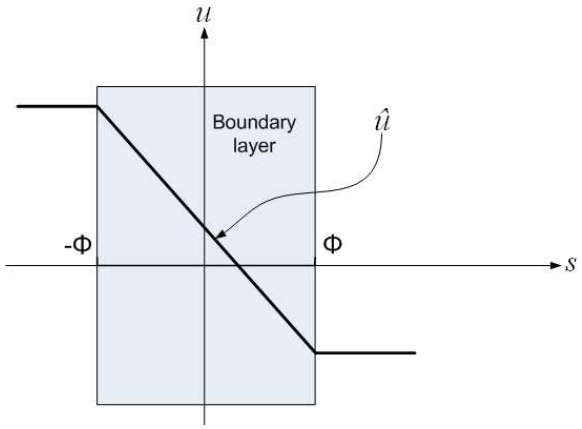

Figure A.8 The boundary layer

Given the results of the section A.0.1, this leads to tracking to within a guaranteed precision ϵ (rather than "perfect" tracking), and more generally guarantees that for all trajectories starting inside $B(t=0)$.

$$\forall t \geq 0, \quad \left|e^{(i)}(t)\right| \leq (2\lambda)^i \varepsilon \quad i = 0, ..., n-1 \tag{A.26}$$

The intuitive understanding of the effect of control interpolation in a boundary layer can be carried on further, and guide the selection of the design parameters λ and Φ. *It is shown below that the smoothing of the control discontinuity inside $B(t)$ essentially assigns a low-pass filter structure to the local dynamics of the variable s, thus eliminating chattering.* Recognizing this filter-like structure then allows for tune-up of the control law so as to achieve a trade-off between tracking precision and robustness to un-modeled dynamics. Boundary layer thickness Φ can be made time-varying, and can be monitored so as to well exploit the control "bandwidth" available.

Consider again the system (Eq. A.1) with $b = 1$. In orderto maintain attractiveness of the boundary layer now that Φ is allowed to vary with time, we must modify condition (Eq. A.13). We now need to guarantee that the distance to the boundary layer always decreases.

$$s \geq \Phi \qquad \Rightarrow \qquad \frac{d}{dt}[s - \Phi] \leq -\eta \tag{A.27}$$

$$s \leq -\Phi \qquad \Rightarrow \qquad \frac{d}{dt}[s - (-\Phi)] \geq \eta \tag{A.28}$$

Thus, instead of simply requiring that (Eq. A.13) be satisfied outside the boundary layer, we now require that (combining the above equations)

$$s \geq \Phi \qquad \Rightarrow \qquad \frac{1}{2}\frac{d}{dt}s^2 \leq (\dot{\Phi} - \eta)\,|s| \tag{A.29}$$

The additional term $\dot{\Phi}|s|$ in Eq. A.29 reflects the fact that the boundary layer attraction condition is more stringent during boundary layer contraction ($\dot{\Phi} < 0$) and less stringent during boundary layer expansion ($\dot{\Phi} > 0$). In order to satisfy Eq. A.29, the quantity $-\dot{\Phi}$ is added to control discontinuity gain $k(x)$, i.e., in our smoothed implementation the term $k(x)sgn(s)$ obtained from switched control law u is actually replaced by $\bar{k}(x)sat(s/\Phi)$, where

$$\bar{k}(X) = k(X) - \dot{\Phi} \tag{A.30}$$

and sat is the saturation function:

$$sat(y) = y \qquad if \quad |y| \leq 1 \tag{A.31}$$

$$sat(y) = sgn(y) \qquad otherwise \tag{A.32}$$

Accordingly, the control law u becomes:

$$u = \hat{u} - \bar{k}(X)sat(s/\Phi) \tag{A.33}$$

Let's consider the system trajectories inside the boundary layer. They can be expressed directly in terms of s as

$$\dot{s} = -\bar{k}(X) \quad \frac{s}{\Phi} - \Delta f(X) \tag{A.34}$$

where, $\Delta f = \hat{f} - f$. Now since $\bar{k}$ and Δf are continuous in x, we can exploit Eq. A.7 to rewrite Eq. A.34 in the form

$$\dot{s} = -\bar{k}(X_d)\frac{s}{\Phi} + (-\Delta f(X_d) + O(\varepsilon)) \tag{A.35}$$

We see from Eq. A.35 that the variable s (which is a measure of the algebraic distance to the surface $S(t)$) can be viewed as the output of a first-order filter, whose dynamics only depends on the desired state $x_d(t)$, and whose inputs are, the perturbations, i.e., uncertainty $\Delta f(x_d)$. Thus, chattering can indeed be eliminated, as long as high-frequency un-modeled dynamics are not excited.

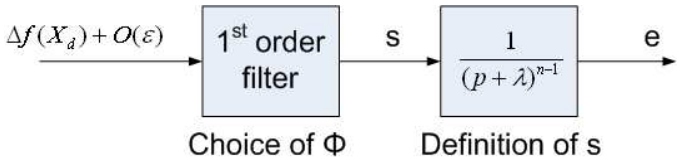

Figure A.9 Structure of the closed-loop error dynamics

Conceptually, the structure of the closed-loop error dynamics can be summarized by Fig. A.9. From the figure we see that, the perturbations are filtered according to

Eq. A.35 to give s, which in turn provides tracking error e by further low-pass filtering, according to definition (Eq. A.4). Control action u is a function of x and x_d. Now, since λ is the break frequency (Eq. A.4, it must be chosen to be small with respect to high-frequency un-modeled dynamics. Furthermore, the boundary layer thickness should be tuned so that Eq. A.35 also represents a first-order filter of bandwidth λ. It suffices to let

$$\frac{\bar{k}(X_d)}{\Phi} = \lambda \tag{A.36}$$

which can be written from Eq. A.30 as

$$\dot{\Phi} + \lambda\Phi = k(X_d) \tag{A.37}$$

Equation A.37 defines the desired time-history of the boundary layer thickness Φ, and is referred to as the "Balance Condition". Intuitively, it amounts to tuning up the closed loop system so that it mimics an n^{th} order critically damped system. Combining Eq. A.37 with A.30, we get

$$\bar{k}(X) = k(X) - k(X_d) + \lambda\Phi \tag{A.38}$$

The s-trajectory, i.e., the variation of s with time, is a compact descriptor of the closed-loop behavior: the control activity directly depends on s, while by definition (Eq. A.4), tracking error e ie merely a filtered version of s. Furthermore, the s-trajectory represents a time-varying measure of the validity of the assumptions on model uncertainty. Similarly, the boundary layer thickness Φ describes the evolution of dynamic model uncertainty with time.

A.1 Lyapunov stability theory

In sliding mode control, Lyapunov's direct method, which is not restricted to local motion of the system dynamics is used both for controller synthesis as well as for sta-

bility analysis. A brief background of the theory is provided here again for the reader's reference.

The philosophy of Lyapunov's direct method is that when faced with a set of nonlinear differential equations, the basic procedure of the method is to generate a scalar "energy-like" function for the dynamic system, and examine the time variation of that scalar function. In this way, conclusions may be drawn on the stability of the set of differential equations without using the difficult stability definitions or requiring explicit knowledge of solutions.

A.1.1 Positive definite functions and Lyapunov functions

The energy function used for Lyapunov's direct method must have two properties:

1. The first is a function of the property itself: it is strictly positive unless both state variables x and $\dot{x}$ are zero.

2. The second property is the property associated with the system dynamics.

In Lyapunov's direct method, the first property is formalized by the notion of *positive definite functions*, and the second is formalized by the so-called Lyapunov functions. Let us discuss positive definite functions first.

Definition: *A scalar continuous function V(X) is said to be locally positive definite if* $V(0) = 0$ *and in a ball* B_{R_0}

$$X \neq 0 \quad \Rightarrow \quad V(X) > 0 \tag{A.39}$$

If $V(0) = 0$ *and the above property holds over the whole state space, then* $V(X)$ *is said to be globally positive definite.* The above definition implies that the function V has a unique minimum at the origin 0. The geometric meaning of locally positive definite functions is as follows.

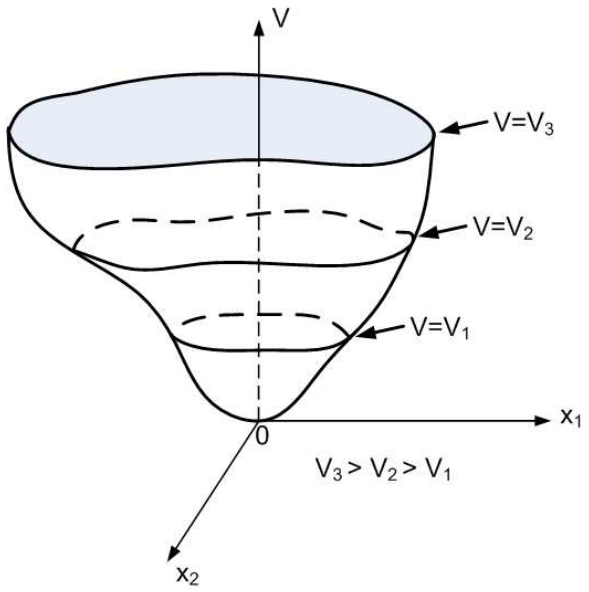

Figure A.10 Typical shape of a positive definite function $V(x_1, x_2)$

Consider a positive definite function $V(X)$ of two state variables x_1 and x_2. Plotted in a 3-dimensional space, $V(X)$ typically corresponds to a surface looking like an upward cup (Fig. A.10). The lowest point of the cup is located at the origin. A second geometric representation can be made as follows. Taking x_1 and x_2 as cartesian co-ordinates, the level curves $V(x_1, x_2) = V_\alpha$ typically represent a set of ovals surrounding the origin, with each oval corresponding to the value of V_α. These ovals, often called contour curves, may be thought as the sections of the cup by horizontal planes, projected on the (x_1, x_2) plane a shown in Fig. A.11. Note: The contour curves do not intersect, because $V(x_1, x_2)$ is uniquely defined given (x_1, x_2). A few related concepts can be defined similarly, in the local or global sense, i.e., a function $V(X)$ is negative definite if $-V(X)$ is positive definite; $V(X)$ is positive semi-definite if $V(0) = 0$ and $V(X) > 0$ for $x \neq 0$; $V(X)$ is negative semi-definite if $-V(X)$ is positive semi-definite.These concepts can be given geometric meanings similar to the ones given for positive definite functions.

With X denoting the state of an autonomous system $\dot{X} = f(X)$, a scalar function $V(X)$ actually represents an implicit function of time. Assuming that $V(X)$ is differen-

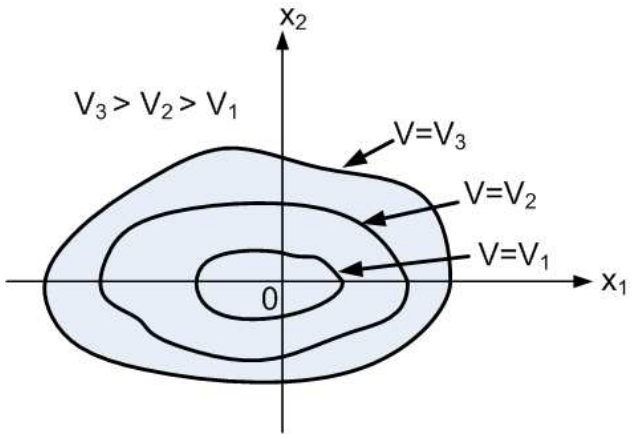

Figure A.11 Interpreting postive functions using contour curves

tiable, its derivative with respect to time can be found by the chain rule,

$$\dot{V} = \frac{dV(X)}{dt} = \frac{\partial V}{\partial x}\dot{X} = \frac{\partial V}{\partial x}f(X) \tag{A.40}$$

We notice here that, because X is required to satisfy the autonomous state equations $\dot{X} = f(X)$, $\dot{V}$ only depends on X. It is often referred to as "the derivative of V along the system trajectory".

Definition:*If, in a ball B_{R_0}, the function $V(X)$ is positive definite and has continuous partial derivatives, and if its time derivative along any state trajectory of the system $\dot{X} = f(X)$ is negative semi-definite, i.e.,*

$$\dot{V} \leq 0 \tag{A.41}$$

then $V(X)$ is said to be a **Lyapunov function** for the system $\dot{X} = f(X)$.

A Lyapunov function can be given simple geometric interpretations. in Fig., the point denoting the value of $V(x_1, x_2)$ is seen to always point down an inverted cup. In Fig.A.12, the state point is seen to move across contour curves.

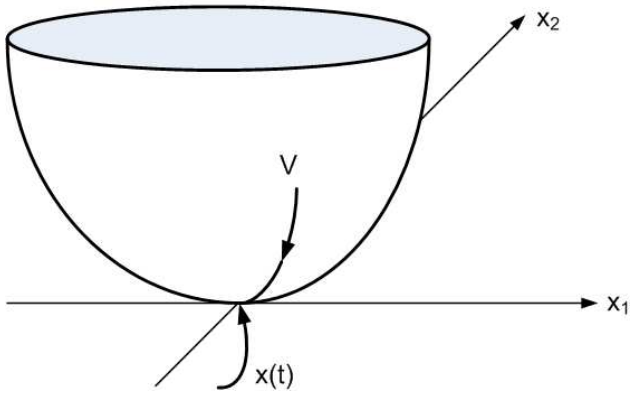

Figure A.12 Geometric interpretation of Lyapunov function for n=2

A.1.2 Lyapunov theorem for local stability

Theorem: (Local Stability) *If, in a ball B_{R_0}, there exists a scalar function $V(X)$ with continuous first partial derivatives such that*

- $V(X)$ is positive definite (locally in B_{R_0})
- $\dot{V}(X)$ is negative semi-definite (locally in B_{R_0})

then the equilibrium point 0 *is stable. If, actually, the derivative $\dot{V}(X)$ is locally negative definite in B_{R_0}, then the stability is asymptotic.*

The proof of this fundamental result is conceptually simple and can be derived using the geometric interpretation of a Lyapunov function as illustrated in Fig. A.11 for the case n=2. A detailed proof of the above theorem can be found in (65).

A.1.3 Lyapunov theorem for global stability

The above theorem applies for the local analysis of stability. In order to assert global asymptotic stability of a system, the ball B_{R_0} in the above local theorem has to be expanded to be the whole state-space. This is indeed necessary, but not sufficient. An additional condition on the function V has to be satisfied: $V(X)$ must be "radially

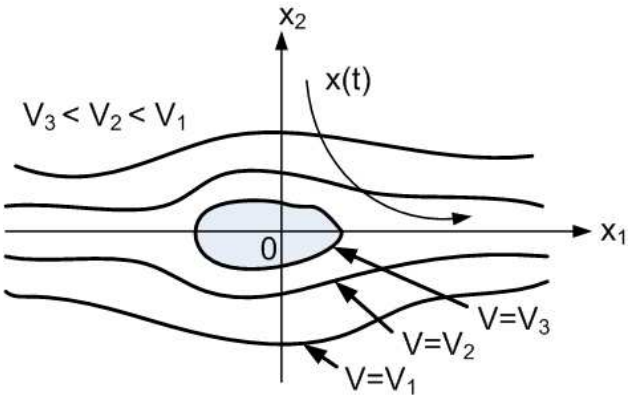

Figure A.13 Motivation of the radial unboundedness condition

unbounded", implying that $V(X) \rightarrow \infty$ as $\| x \| \rightarrow \infty$. We then obtain the following powerful result:

Theorem: (Global Stability) *Assume that there exists a scalar function V of the state X, with continuous first order derivatives such that,*

- $V(X)$ is positive definite
- $\dot{V}(X)$ is negative definite
- $V(X) \rightarrow \infty$ as $\| x \| \rightarrow \infty$

then the equilibrium at the origin is globally asymptotically stable.

In the above theorem, the reason for the radial unboundedness condition is to assure that the contour curves (or contour surfaces for higher order systems) $V(X) = V_\alpha$ correspond to closed curves. If the curves are not closed, it is possible for the state trajectories to drift away from the equilibrium point, even though the state keeps going through contours corresponding to smaller and smaller $V'_\alpha s$ as portrayed in Fig. A.13. The proof for this theorem is along the same lines as that for the local case and the reader is referred to (65) for a detailed explanation. The theorem on global stability is very useful for the design and stability analysis of sliding mode controllers.

APPENDIX B. Simulink block diagrams

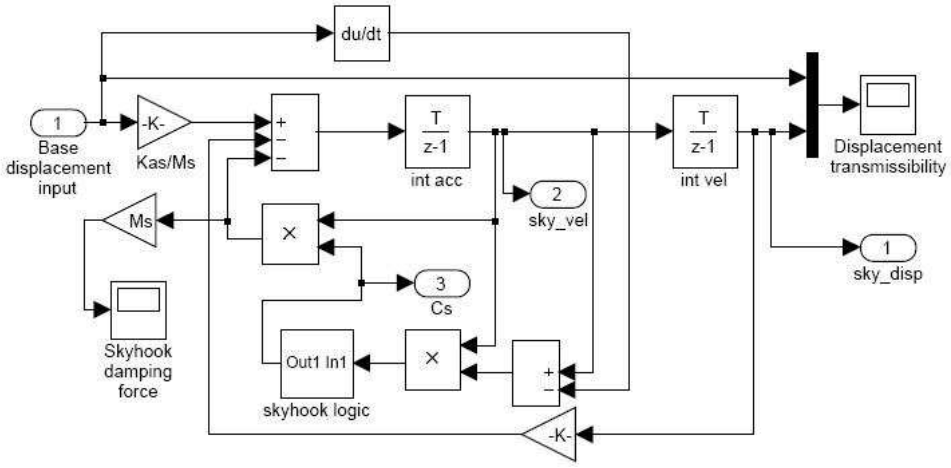

Figure B.1 Block diagram of "skyhook model" subsystem of Fig. B.2

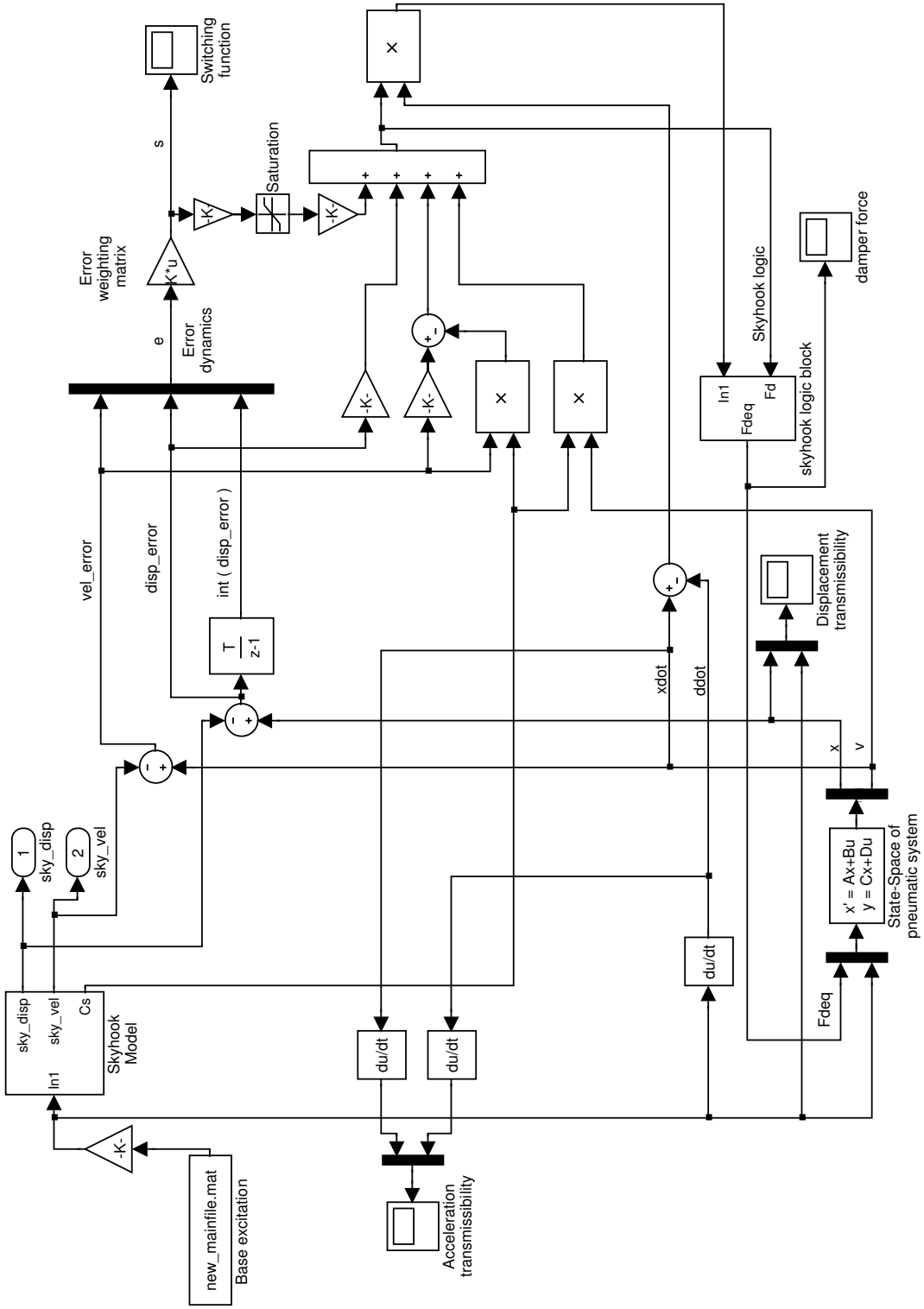

Figure B.2 Closed loop system with sliding mode controller (simulation)

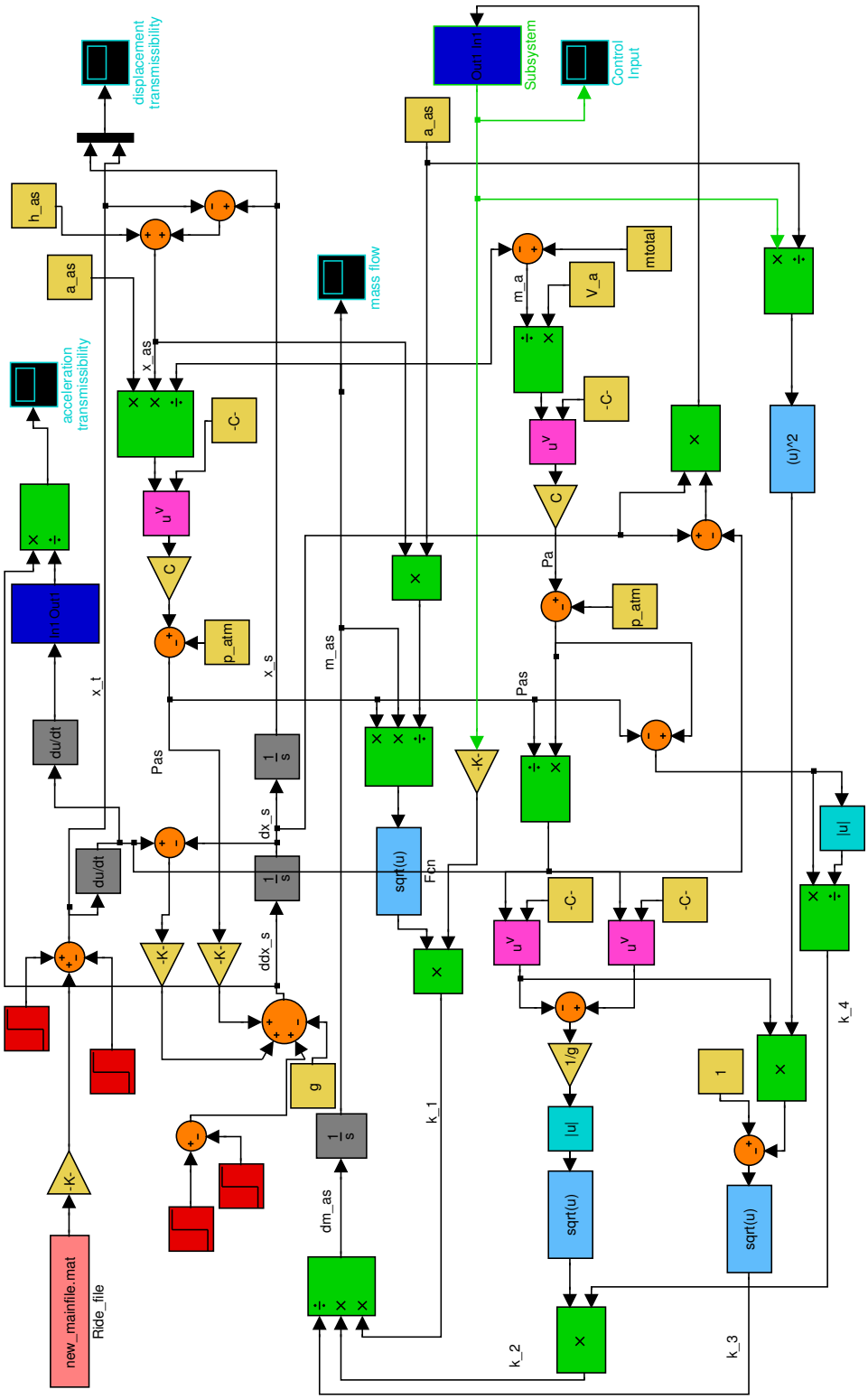

Figure B.3 Simulink model of Eqs. (4.1) and (4.14)

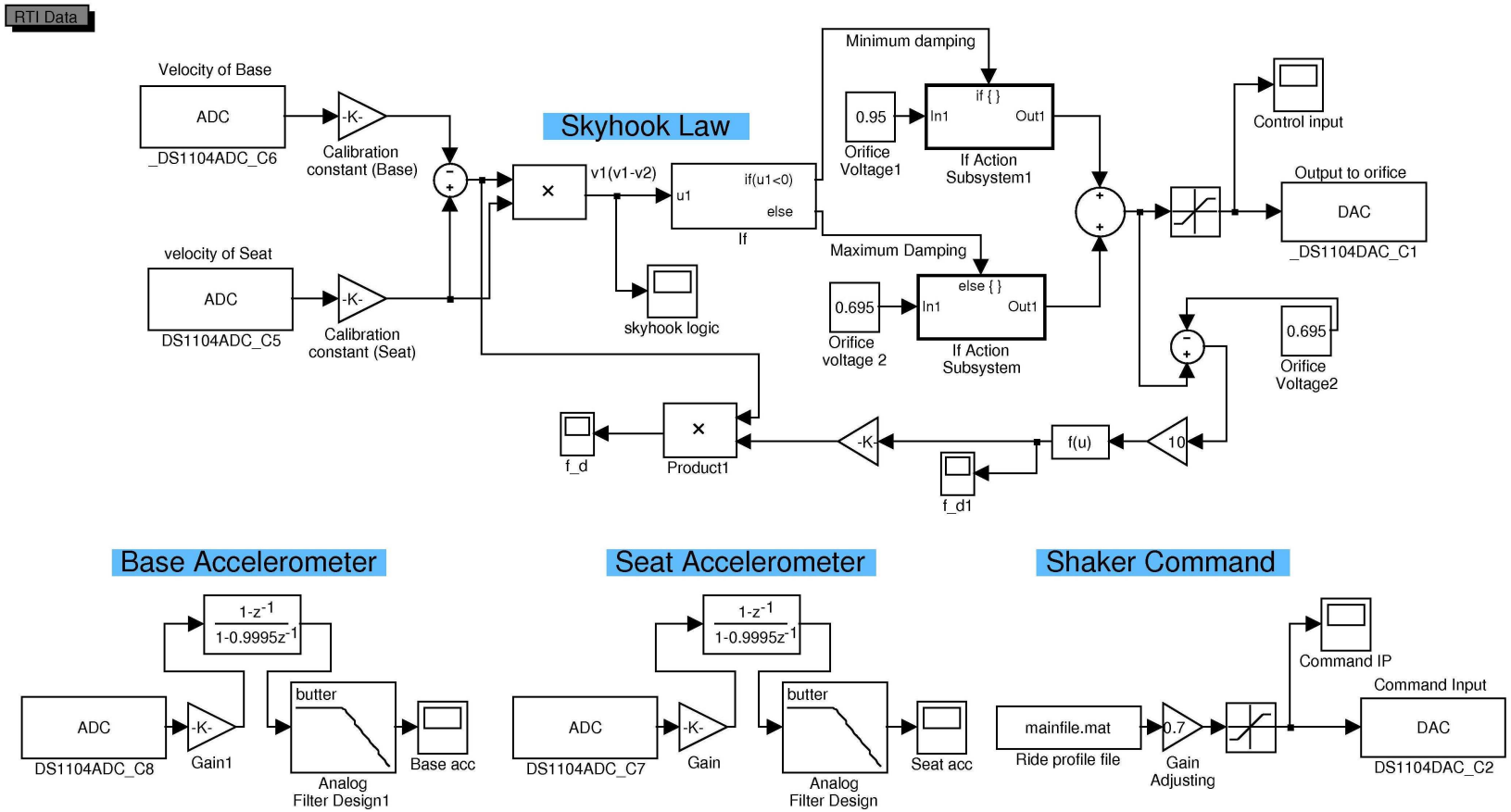

Figure B.4 Closed loop system with skyhook controller (hardware-in-loop)

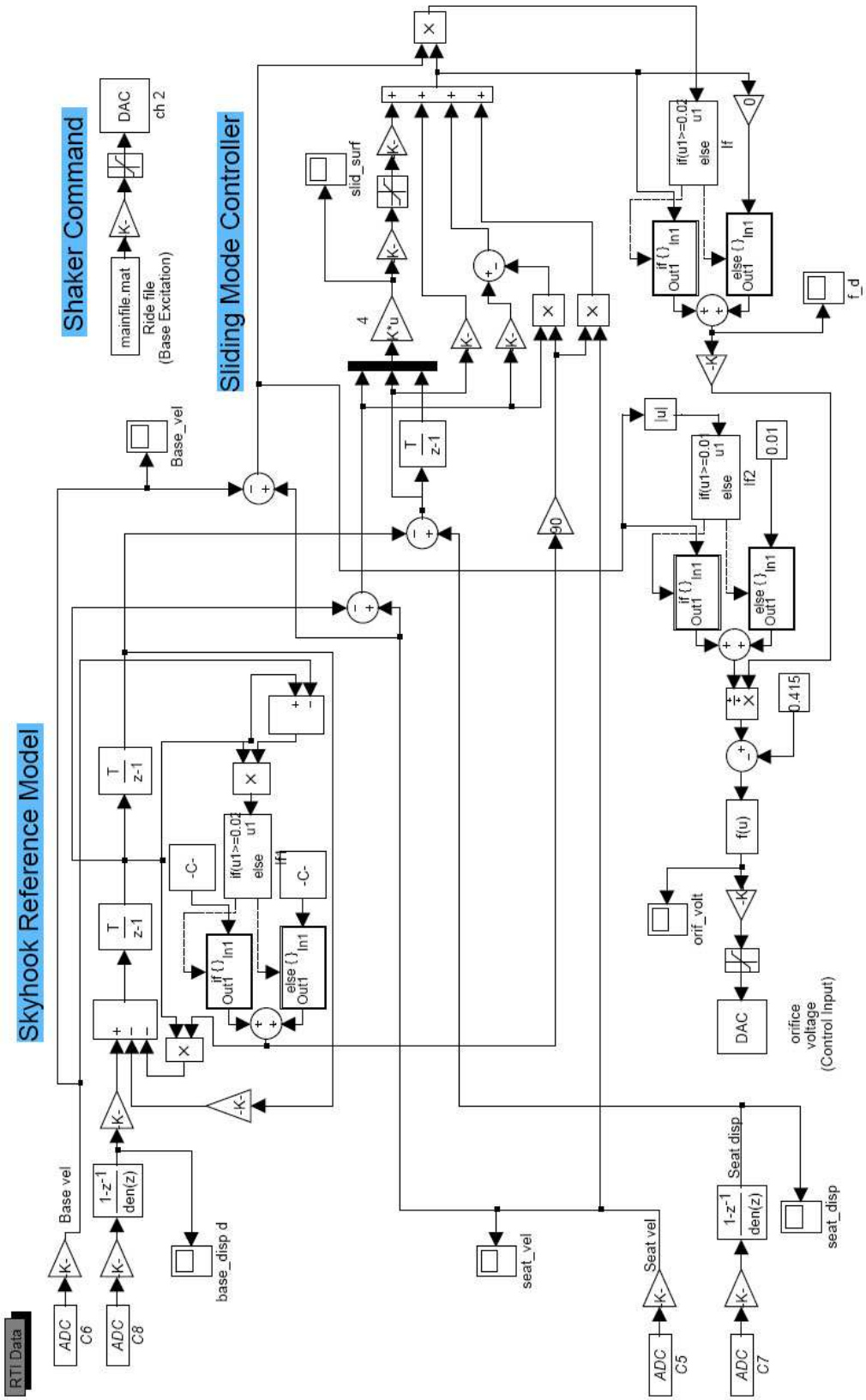

Figure B.5 Closed loop system with sliding mode controller (hardware-in-loop)

BIBLIOGRAPHY

[1] Barak. (1992). "Passive versus active and semi-active suspension from theory to application in North American industry." *SAE paper No. 922140.*

[2] El Madany MM and Dokainish MA. (1979). "Ride-dynamics of articulated vehicles- A literature survey." *Vehicle system dynamics.* Vol. 8, pp 287-316.

[3] Hedrick JK and Wormerly DN. (1975). "Active suspension for ground support vehicles- A state-of-the-art Review." *ASME-AMD*, Vol. 15, pp 21-40.

[4] Hedrick JK. (1981). "Railway vehicle active suspension." *Vehicle System Dynamics*, Vol. 10, pp 267-283.

[5] Hrovat D. (1993). "Application of Optimal Control to Advanced Automotive Suspension Design." *Trans. ASME, Journal of Dynamic Systems, Measurement and Control*, Vol. 115, pp 328-342.

[6] Morman KN and Giannopoulis F. (1982). "Recent Advances in Analytical and Computational Aspects of Modeling Active and Passive Vehicle Suspensions." *ASME-AMD*, Vol. 50, pp 75-115.

[7] Ahmed AKW and Rakheja S. (1992). "An Equivalent Linearization Technique for the Frequency Response Analysis of Asymmetric Dampers." *Journal of Sound and Vibration*, Vol. 153(3), pp 537-542.

[8] Burns RN and Sachs HK. (1973). "Ride Comfort as Influenced by Asymmetric Shock Absorber Characteristic." *Proc. 2nd International Conference on Vehicle Mechanics.*

[9] Dahlberg T. (1979). "An Optimized Speed-Controlled of a 2-DOF vehicle Travelling on a Randomly Profiled Road." *Journal of Sound and Vibration*, Vol. 64(4), pp 541-546.

[10] Dahlberg T. (1980). "Comparison of Ride Comfort Criteria for Computer Optimization of Vehicle Travelling on a Randomly Profiled Road." *Vehicle System Dynamics*, Vol. 9, pp 291-307.

[11] Demic M. (1989). "Optimization of the Charateristics of the Elasto-Damping elements of a passenger car by means of a Modified Nelder-Mead Method." *International Journal of Vehicle Design*, Vol. 10(2), pp 137-149.

[12] El Madany MM and Dokainish, MA. (1980). "Optimum Design of Tractor Semi-Trailer Suspension Systems." *SAE*, Paper No. 801419.

[13] El Madany MM. (1987). "An Analytical Investigation of Isolation Systems for Cab Ride." *Computers and Structures*, Vol. 27(5), pp 679-688.

[14] El Madany MM. (1987). "A Procedure for Optimization of Truck Suspension." *Vehicle System Dynamics*, Vol. 16, pp 297-312.

[15] El Madany MM. (1988). "Design and Optimization of Truck Suspension Using Covariance Analysis." *Journal of Computers and Structures*, Vol. 28(2), pp 241-245.

[16] Esmailzadeh E. (1987). "Design Synthesis of a Vehicle Suspension System Using Multi-parameter Optimization." *Vehicle System Dynamics*, Vol. 7, pp 83-96.

[17] Rakheja S, Su H and Sankar TS. (1990). "Analysis of Passive Sequential Hydraulic Damper for Vehicle Suspension." *Vehicle System Dynamics*, Vol. 19, pp 289-312.

[18] Cavanaugh RD. (1976). "Air suspension and Servo Controlled Pneumatic Suspensions." *Shock and Vibration Handbook*, 2nd Ed. (eds. Harris, C.M., Crede, C.E), McGraw Hill B.C, Chapter 33.

[19] Baker A. (1984). "Lotus Active Suspension." *Automotive Engineer*, Feb/Mar, pp 55-57.

[20] Aoyama Y. et al. (1990): "The Development of the Fully Active Suspension by Nissan." *SAE*, Paper No. 901747.

[21] Goto T, Kizu R, Ohnuma T and Ohnu H. (1990). "Toyota Active Control Supension for the 1989 Celica." *Proceedings 22nd ISATA*.

[22] Beard D and Karnopp D. (1993). "Design and Simulation of High Performance Energy Efficient Active Suspension System." *International Conference on Bond Graph Modeling, Simulation Series*, Vol. 2 *(Society for Computers and Simulation)*, pp 249-254.

[23] Chalasani RM. (1986). "Ride performance Potential- Part I, Simplified Analysis based on Quarter-Car Model." *ASME-AMD*, Vol. 80, DSC Vol. 2, pp 187-202.

[24] Bender EK. (1968). "Some Fundamental Limitations of Active and Passive Suspension System." *SAE*, paper No. 680750.

[25] Karnopp D. (1992). "Power Requirements for Vehicle dynamics." *Vehicle System Dynamics*, Vol. 21, pp 65-71.

[26] Milliken WF. (1988). "Active Suspension." *SAE*, Paper No. 880799.

[27] Lundstrm R and Holmlund P. (1988). "Absorption of Energy During Whole-body Vibration Exposure." Journal of Sound and Vibration, Vol. 215, pp 801-812.

[28] Mansfield NJ and Griffin MJ. (1998). "Effect of Magnitude of Vertical Whole-body Vibration on Absorbed Power for the Seated Human Body." Journal of Sound and Vibration, Vol. 215, pp 813-825.

[29] Seidel H, Blthner R, Hinz B and Schust M. (1998). "On the Health Risk of the Lumbar Spine due to Whole-body Vibration - Theoretical Approach, Experimental Data and Evaluation of Whole-body Vibration." *Journal of Sound and Vibration*, Vol. 215, pp 723-741.

[30] International Organisation for Standardisation (ISO). (1997). "ISO 2631-1:1997, Mechanical Vibration and Shock - Evaluation of Human Exposure to Whole-body Vibration." Part 1, General Requirements, ISO, Switzerland.

[31] Choi SB, Choi JH, Lee YS and Han MS. (2000). "Vibration Control of an ER Seat Suspension for a Commercial Vehicle." *Journal of Dynamic Systems, Measurement, and Control. ASME.*

[32] Choi SB, Choi JH, Lee YS and Han MS. (2003). "Vibration Control of an ER Seat Suspension for a Commercial Vehicle." *Transactions of the ASME*, Vol. 125, pp 60-68.

[33] Simon D and Ahmadian M. (2001). "Vehicle evaluation of the performance of magnetorheological dampers for heavy truck suspensions." *Journal of Vibration and Acoustics. ASME.*

[36] Kitching KJ, Cole DJ and Cebon D. (2000) "Performance of a Semi-Active Damper for Heavy Vehicles." *Journal of Dynamic Systems, Measurement, and Control. ASME.*

[35] Hong KS, Sohn HC and Hedrick JK. (2002) "Modified Skyhook Control of Semi-Active Suspensions: A New Model, Gain Scheduling, and Hardware-in-the-Loop Tuning." *Transactions of the ASME*, Vol. 124, pp 158-167.

[36] Choi SB, Park DW and Suh MS. (2002). "Fuzzy Sky-Ground Hook Control of a Tracked Vehicle Featuring Semi-Active Electrorheological Suspension Units." *Transactions of the ASME*, Vol. 124, pp 150-157.

[37] Simon D and Ahmadian M. (2001). "Vehicle Evaluation of the Performance of Magneto Rheological Dampers for Heavy Truck Suspensions." *Journal of Vibration and Acoustics* , Vol. 123, pp 365-375.

[38] Vogel JM, Hooper SJ and Hand JL. (1985). "Apparatus for Preventing the Transmission of Vibration." United States Patent No. 4,497,078.

[39] Vogel JM and Claar II PW. (1989). "A Vibration Isolation System for an Optimal Sleeping Environment." *1989 SAE Truck & Bus Exposition*, SAE Paper No. 892524, Charlotte, NC, Published in Transactions.

[40] Vogel JM and Claar II PW. (1991). "Development of a Slow-Active Control Pneumatic Suspension System for Heavy Vehicle Applications." *1991 SAE Truck & Bus Exposition*, SAE Paper No. 912675, Chicago Illinois.

[41] Vogel JM and Claar II PW. (1991). "Developement of a slow-active control pneumatic suspension system for heavy vehicle applications." *SAE Truck and Bus Exposition*, paper No. 912675.

[42] Porumamilla H and Kelkar AG. (2003). "LQG-based robust control of active automobile suspension." In *Proceedings of the 2003 ASME International Mechanical Engineering Congress and Exposition*, volume 2- Dynamic Systems and Control, Washington, D.C.

[43] Porumamilla H and Kelkar AG. (2004). "Mixed sensitivity H_∞ control and μ-analysis of active automobile suspension." *Proc. 2004 ASME Congress and Exposition*, Anaheim Hilton, Anaheim, CA.

[44] Porumamilla H and Kelkar AG. (2005). "Robust control and analysis of active pneumatic suspension." *Proc. 24th American Control Conference*, Portland, Oregon.

[45] Ahmadian M, Song X and Southward SC. (2004). "No-Jerk Skyhook Control Mehods for Semiactive Suspensions." *Journal of Vibration and Acoustics. ASME.*

[46] Porumamilla H, Kelkar AG and Vogel JM. (2007). "Modelling and Verification of an Innovative Active Pneumatic Vibration Isolation System." *Journal of Dynamic Systems, Measurement and Control*, ASME.

[47] Porumamilla H, Kelkar AG and Vogel JM. (2007). "Implementation of a Modified Skyhook Control on a purely pneumatic semi-active suspension system." *2007 ASME International Mechanical Engineering Congress and Exposition*, ASME.

[48] Lord corporation. (2003). "Lord Rheonetic Magnetically Responsive Technology 2003 MR Damper." RD-1005-3 *Product Bulletin.*

[49] Koo JH, Goncalves FD and Ahmadian M. (2006) "A comprehensive analysis of response time of MR dampers." *Smart Materials and Structures*, Vol. 15, pp 351-358.

[57] Karnopp D. (1990). "Design Principles for Vibration Control Systems Using Semiactive Dampers." *Trans. ASME Journal of Dynamics Systems, Measurements and Control,* Vol 112, pp 448-455.

[51] Ahmadian M. (1999). "On the Isolation Properties of Semi-active Controllers." *Journal of Vibration and Control*, Vol. 5, pp 217-232.

[58] Karnopp D, Crosby MJ and Harwood RA. (1978). "Vibration Control Systems Using Semi-active Force Generators." *Journal of Engineering for industry.*

[53] Seigler M and Ahmadian M. (2002). "A Comparative Analysis of Air-Inflated and Foam Seat Cushions for Truck Seats." *International Truck & Bus Meeting & Exhibition*, SAE Paper No 2002-01-3108, November 2002, Detroit, MI, USA

[54] Jalili N. (2001). "An Infinite Dimensional Distributed Base Controller for Regulation of Flexible Robot Arms." *Transactions of the ASME*, Vol. 123, pp 712-736.

[55] Jalili N and Esmailzadeh E. (2001). "Optimum Active Vehicle Suspensions With Actuator Time Delay." *Transactions of the ASME*, Vol. 123, pp 54-61.

[56] Jalili N. (2000). "A Comparative Study and Analysis of Semi-Active Vibration-Control Systems." *Journal of Vibration and Acoustics*, Vol. 124, pp 593-515.

[57] Karnopp D. (1983). "Active damping in road vehicle suspension systems." *Vehicle System Dynamics*, Vol. 12, pp. 291-311.

[58] Karnopp D. (1986). "Theoretical limitations in active suspensions." *Vehicle System Dynamics*, Vol. 15, pp 41-54.

[59] Karnopp D. (1974). "Vibration control using semi-active force generators." *Journal of engineering for industry.*

[60] Bender EK. (1967). "Optimum linear random vibration isolation." *Reprints 1967 JACC*, pp. 135-143.

[61] Bender EK, Karnopp D and Paul IL. (1967). "On the optimization of vehicle suspensions using random process theory." *ASME paper No. 67-Tran-12*.

[62] ElMadany MM. (1990). "Optimal linear active suspension with multivariable integral control." *Vehicle System Dynamics*, Vol. 19, pp 313-329.

[63] ElMadany MM. (1992). "Integral and state variable feedback controllers for improved performance in Automotive vehicles." *Computers and Structures*, Vol. 42, No.2, pp 237-244.

[64] Bentley JP. (1988). "Principles of measurement systems." *Second edition*, pp 287-307.

[65] Slotine JJ and Li W. (1990). "Applied Non-linear Control." *Prentice Hall*.

[66] Vogel JM and kelkar AG. (2004). "A continuously variable natural frequency vibration isolation system." *ISURF Docket No. 05V1822*.

[67] Porumamilla H, Vogel JM and kelkar AG. (2006). "Pneumatic Vibration Isolation Device." *Docket No. 506149-PROV*.